工學博士學位論文

Performance Enhancement of Silica Nanomaterials-Based Smart Fluids Responsive to Electric Field, Magnetic Field, and Light

전기장, 자기장, 빛에 감응하는 실리카 나노물질을 기반으로 하는 지능형 유체들의 성능 향상

2018年 5月

서울大學校 大學院

化學生物工學部

尹 暢 敏

Performance Enhancement of Silica Nanomaterials-Based Smart Fluids Responsive to Electric Field, Magnetic Field, and Light

by

Chang-Min Yoon

Submitted to the Graduate School of Seoul National University in Partial Fulfillment of the Requirements for the Degree of Doctor of Philosophy

May, 2018

Thesis Adviser: Jyongsik Jang

Abstract

Smart fluids (*i. e.* stimuli-responsive fluid), composed of stimuli-responsive materials dispersed in a media, are able to change their rheological/mechanical properties in response to various external stimuli like magnetic field, electric field, light, and temperature. Smart fluids are receiving tremendous attentions from academia and industrial fields ascribed to their captivating advantages including fast response, fine controllability, simple operation mechanics, low power consumption, and facile reversibility. Among various smart fluids, three types of electro-responsive smart fluid, magneto-responsive smart fluid, and photo-responsive smart fluids responsive to electric field, magnetic field, and lights have attracted a of most special interests due to relatively easy preparation, high resulting changes in mechanical/rheological characteristics, and high possibility for practical application. With the advance of nanotechnology, conventional micro-scaled stimuli-responsive materials for smart fluid applications have been started to replace by the nanomaterials. Nanomaterials possess superiorities in dimension, size, loading capacity, dispersion, and surface area over micro-scale materials, thus nanomaterials-based smart fluids have exhibited distinct

characteristics compared to the conventional smart fluids. Silica nanomaterials possess various positive characteristics like availability for mass-productions, mono-dispersity, thermal stability, and size-controllability, which make them as a good candidate for smart fluid applications. However, there still exist necessities of developments for silica nanomaterials highly responsive to various external fields by facile synthetic method and incorporating with other nanomaterials.

This dissertation describes the effective synthetic and formulation methods of various silica nanomaterials including mesoporous and hybridized and their-derived smart fluids responsive to various external fields of electric field, magnetic field, and lights. Firstly, mesoporous silica nanomaterials with different aspect ratio are synthesized by facile sol-gel method. The resulting mesoporous silica nanomaterials-based electro-responsive smart fluids displayed high electro-responsive activity ascribed to the improved dielectric property and dispersion stability. Secondly, multi-layered numerous magnetite-embedded silica/titania core/shell with outermost silica shell nanomaterial is prepared by sequential synthetic steps using silica nanomaterial as a core-template. Owing to the successful incorporation of various nanomaterials, multi-layered magnetite-

embedded silica/titania core/shell with outermost silica shell nanomaterial-based smart fluid manifest a dual responsive characteristic toward magnetic and electric fields. Finally, photosensitive silica nanomaterials are fabricated by coating of spiropyran molecules using silane. The resulting smart fluid is formulated as highly susceptible fluid to both electric field and light. Accordingly, this study provides promising synthetic approaches for formulation method of highly efficient silica nanomaterials-based smart fluids responsive to various external fields of electric field, magnetic field, and lights.

Keywords: Nanomaterial, Silica nanomaterial, Smart fluid, Stimuli-responsive, Electric field, Magnetic field, Light.

Student Number: 2013-23167

List of Abbreviations

A: cross-sectional area

A_z: depolarization factor

APTES: 3-aminopropyltrimethoxysilane

BET: Brunauer–Emmett–Teller

BJH: Barrett–Joyner–Halenda

C_d: drag coefficient

cSt: centistoke

CTAB: cetrimonium bromide

E field: electric field

EDS: energy-dispersive spectroscopy

EMR: electromagneto-responsive, or electromagnetorheological

EPR: electrophoto-reponsive, or electrophotorheological

ER: electro-responsive, or electrorheological

f_{max}: The maximum peak determined in the loss factor curve

FE-SEM: field emission-scanning electron microscope

Fe_3O_4: magnetite, or iron oxide

FT-IR: fourier-transform infrared spectroscope

GPTS: (3-glycidyloxypropyl)trimethoxysilane

H field: magnetic field

hr: hour

kV: kilovolt

L/D: aspect ratio

MC: merocyanine

MR: magneto-responsive, or magnetorheological

mSiO_2: mesoporous silica

min: minute

mL: milliliter

mm: millimeter

N_2: nitrogen

nm: nanometer

OM: optical microscope

Pa: pascal

r′: shear rate

s: second

Silylated-SiO_2: GPTS connected silica

SiO_2: silica

SiO_2/TiO_2 core/shell: silica/titania core/shell

SiO_2/TiO_2@Fe_3O_4: magnetite-embedded silica/titania core/shell

$SiO_2/TiO_2@Fe_3O_4/SiO_2$: magnetite-embedded silica/titania core/shell with outermost silica shell

SP: spiropyran

SP-SiO_2: spiropyran-decorated silica

STEM: scanning transmission electron microscope

TEOS: tetraethylorthosilicate

TEM: transmission electron microscope

TTIP: titanium isopropoxide

TiO_2: titania

UV: ultraviolet radiation

VIS: visible light

V: volume

XPS: X-ray photoemission spectroscopy

XRD: X-ray diffraction

θ: theta

µm: micro-meter

ε_0: static dielectric constant, or static permittivity

ε_∞: fictitious dielectric constant, or fictitious permittivity

ε': dielectric constant, or permittivity

ε'': dielectric loss

r'_{crit}: critical shear rate

$\Delta\varepsilon$: achievable polarizability

λ: relaxation time

List of Figures

Figure 31. Shear stresses of $SiO_2/TiO_2@Fe_3O_4/SiO_2$ nanomaterials-based EMR smart fluids as a function of shear rate under zero-field (0.0 kV mm^{-1}) and *E* field (3.0 kV mm^{-1}) applied conditions. The concentration EMR fluid smart fluid was set as 20.0 vol%.

Figure 32. The *E* field on−off test of $SiO_2/TiO_2@Fe_3O_4/SiO_2$ nanomaterials-based EMR smart fluids measured with fixed shear rate of 0.1 sec^{-1} (On state: 3.0 kV mm^{-1} and off state: 0.0 kV mm^{-1}).

Figure 33. The on-off test of the $SiO_2/TiO_2@Fe_3O_4/SiO_2$ nanomaterials-based EMR smart fluids by switching and simultaneous applications of the *E* fields (3 kV mm_1) and *H* fields (0.2 T) at a constant shear rate of 0.1 s^{-1}. The directions of dual external field were applied in (a) perpendicular and (b) parallel directions. The boxed images placed right of the shear stress curves present the real-time OM observations of fibril-like structure formations of EMR smart fluids under perpendicular and parallel conditions. The concentration EMR fluid smart fluid was set as 20.0 vol%.

List of Tables

Table 10. Detailed description of ER, PR and EPR activities of ER smart fluids and EPR smart fluid.

Table of Contents

1. Introduction

1.1 Background

1.1.1. Nanomaterial

Nanomaterials are usually known as ultra-small scale materials with the dimension ranges of one tenth of micrometer (< 0.1 μm) [1]. The origins of naturally occurring or artificial nanomaterials are still ambiguous, but with the development of science and technology, human beings are able to synthesize, control, and tailor the nanomaterials. Particularly, interest toward nanomaterials has begun to emerge in the 1980s with the invention and advance of scientific instrument like scanning tunneling microscope [2]. By the early 2000s, nanomaterials have received explosive interests not only from the academia and scientific field, but also publically, industrially, and nationally (**Figure 1**) [3]. Therefore, inorganic and organic materials including various polymer, metal, noble metal, metal oxide, carbon are synthesized as nanomaterials [4-6]. Furthermore, nanoscience and nanotechnology, which are applying various nanomaterials to practical fields, have also progressed with the development of various nanomaterials.

Then why nanomaterials are receiving such tremendous attentions from individual researchers to various scientific fields? Compared to bulk or conventional micro-scale materials, nanomaterials are known to exhibit different, unique, and new advantages in physical and intrinsic characteristics, arising from the infinitesimally small-size and surface property, along with the properties of material itself [7,8]. In physical and simple perspective, properties like surface area (SA), surface area to volume ratio (SA:V), and particle mobility of materials can be greatly increased by lessening the size into nano-scale [9]. Also, physical properties like melting point and electrical conductivity are different in nanomaterials distinct from larger ones [10,11]. From the view point of intrinsic property, nanomaterials demonstrate uniqueness in the band gap energy, optic, dielectric property, surface energy, and chemical reactivity compared to bulk material [12-17]. In turn, nanomaterials are employed and playing important, but different role to bulk materials in fields of recent engineering, chemistry, biology, mechanic, and physics [18-23].

In order to improve the performance of nanomaterials for targeted application field, various strategies, methods, and tactics have been investigated and proposed. One of the most important methods is to

synthesize nanomaterials with high uniformity and monodispersity for reducing the deviation, bias, and mal-function of experimental and intended results. Moreover, performance of nanomaterials can be enhanced by tailoring the surface morphology and structures to porous, hollow, rod, fiber, hierarchical, web, and all others [24,25]. Furthermore, multicomponent, composited, and hybridized nanomaterials are synthesized with the advances in fabrication techniques of nanomaterials [26-28]. Nowadays, most of nanomaterials are synthesized by integrations of aforementioned methods to maximize the efficiency of applications. Although there are some drawbacks like relatively complex synthesis method, high unit cost, and limitations in mass-production, nanomaterials and related nanoscience are one of the most attracting, emerging, fast-developing fields in the present time, which may also impact the human future.

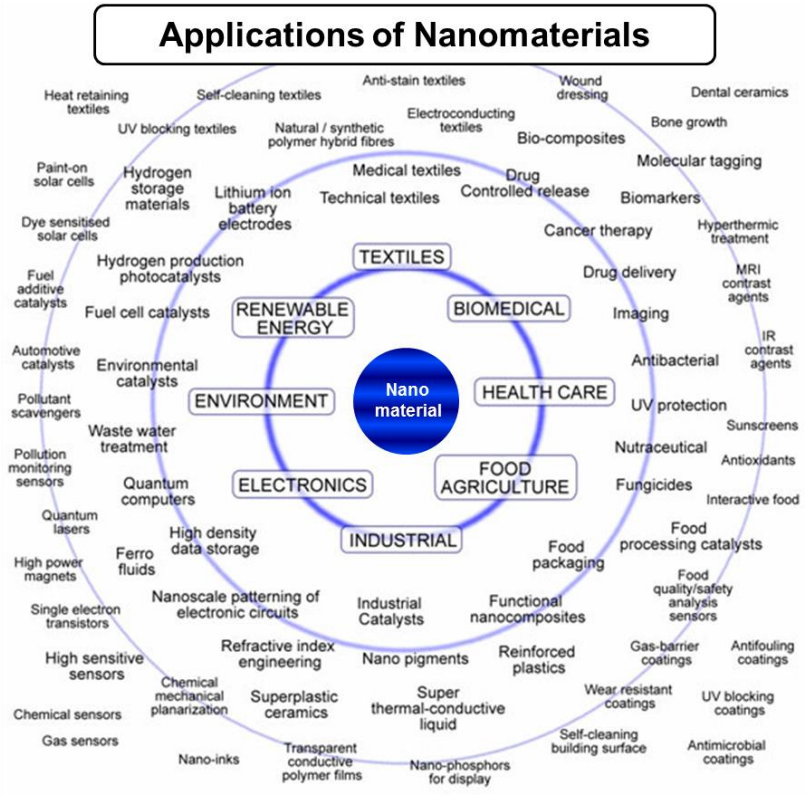

Figure 1. Schematic illustration of wide applications of nanomaterials [3].

1.1.2. Silica nanomaterial

Silica, also referred as silicon dioxide, is an oxide form of silicon with chemical formula of SiO_2. Silica is known as the most abundant kind of materials naturally present in Earth [29]. Many people are unaware, but silica is commonly found and easily access material around us as major constituents of sand, glass, and quartz. Along with the abundance in quantities, silica materials possess various advantages like biocompatibility, chemical/physical inertness, electrical insulation, low cost, and mass-production availability [30-32]. Therefore, silica is a very useful material for human society such as being used in various fields including food, construction, biomedical, electronics, and pharmaceutics [33-35]. Various silica materials can be synthesized for intended purpose of use by methods like purification of quartz, pyrogenic (fumed) synthesis, precipitation, and sol-gel methods [36,37]. With the advent of nanoscience, large efforts have been devoted by many researchers to fabricate various kinds of silica nanomaterials. Numerous synthesis methods have been proposed for different types of silica nanomaterials with distinctive characteristics and advantages.

1.1.2.1. Synthetic methods of silica nanomaterial

Up to now, numerous methods have been invented and set to prepare various types of silica nanomaterials. To a large extent, preparation methods for silica nanomaterials can be classified into top-down or bottom-up methods. Particularly, top-down methods involves the purely physical processes like thermal degradation, mechanical grinding, ball-milling, and pulse laser ablation to reduce the size of bulk silica material down to nano-scale range [38]. In general, it is known that the top-down approaches have advantages in mass-productions, but uniformities of products are not quite guaranteed. As discussed previously, uniformity and monodipersity are very important features in nanomaterials, affecting the performance and preciseness in the practical application fields. In that respect, bottom-up approaches including sol-gel, thermal oxidation, co-precipitation, and microemulsion methods are used to synthesize uniform silica nanomaterials [39,40]. Among various bottom-up approaches, sol-gel method, preparing final solid materials by a conversion of initial sol (*i. e.* suspension of molecular or colloidal suspension) to gel (*i. e.* integrated network) *via* consecutive repetitions of hydrolysis and polycondenstation, is known as the most common and convenient

method to prepare the uniform silica nanomaterials as well as the ceramic and metal oxide materials (**Figure 2**) [41-43]. Specifically, Stöber method, named after W. Stöber after his systematic report regarding on the fabrication of monodisperse silica nanospheres from reactions of silicon alkoxide precursor in the water/alcohol solvent with aqueous catalyst, is the mostly widely utilized synthesis method for silica nanotechnology [44]. After the pioneer invention of W. Stöber, large efforts have been devoted by many researchers on the initial Stöber method to attain thorough controllability over the size and dimensions of silica nanospheres by changing the parameters like reaction temperature, amount of adding reagents, stirring conditions, and type of reacting vessels [45-47]. Furthermore, by adding specific surfactants like cetrimonium bromide into the Stöber systems (so called modified Stöber methods), mesoporous, hollow, and one-dimensional (rod-like and fiber-like) silica nanomaterials are able to synthesize, as shown in **Figure 3 and 4** [48,49]. Although other experimental methods for preparation of silica nanomaterials have been introduced, but the Stöber and modified Stöber methods are still regarded as the most reliable and facile methods to synthesize various silica nanomaterials in uniform and monodisperse manner for

applications in nanotechnologies. At this time, still numerous silica nanomaterials are in on-going production by the above methods, and being underway to apply the advantages of silica nanomaterials to nanotechnologies.

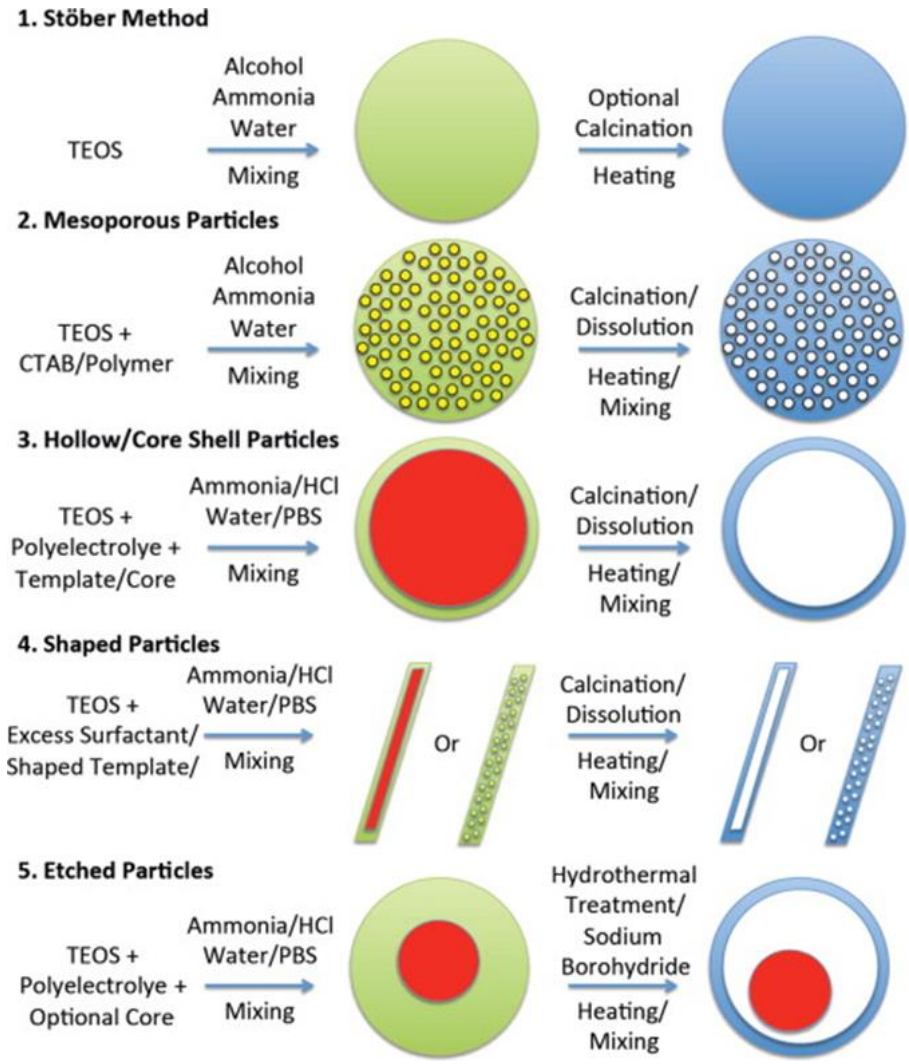

Figure 2. Schematic illustration of the preparation of silica nanomaterials *via* various sol-gel approaches [41].

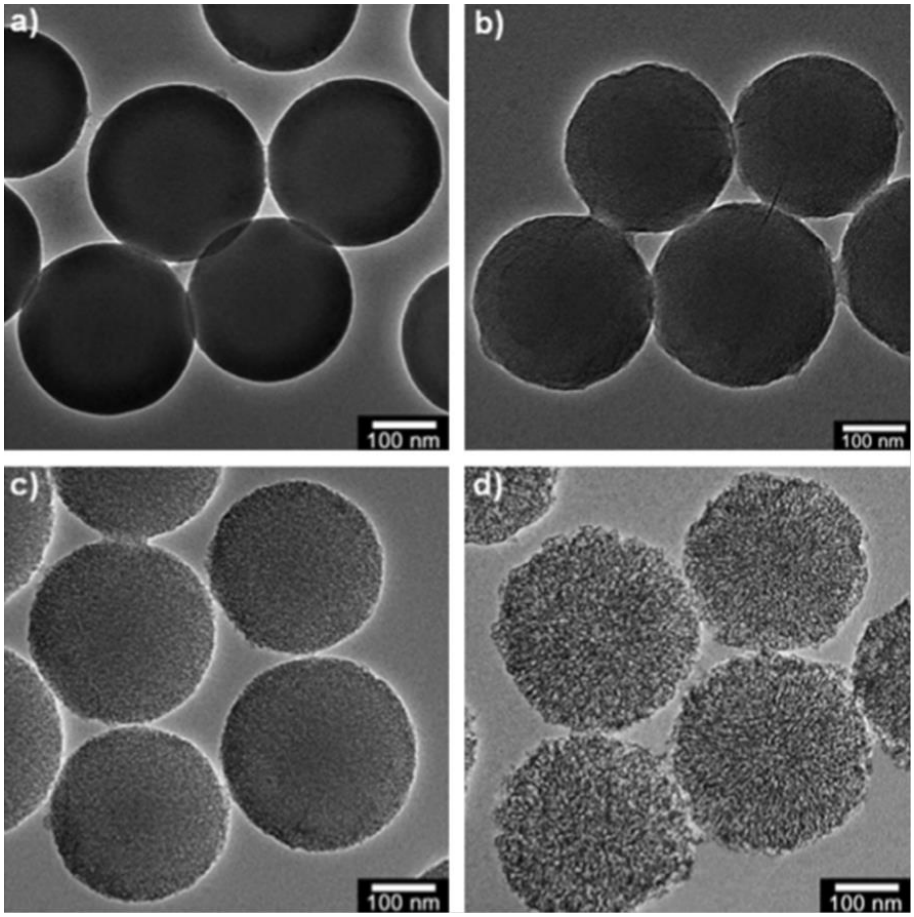

Figure 3. Transmission electron microscope images of a) non-porous silica and mesoporous silica nanomaterials having different pore sizes of b) 1 nm, c) 2 nm, and d) 8 nm [48].

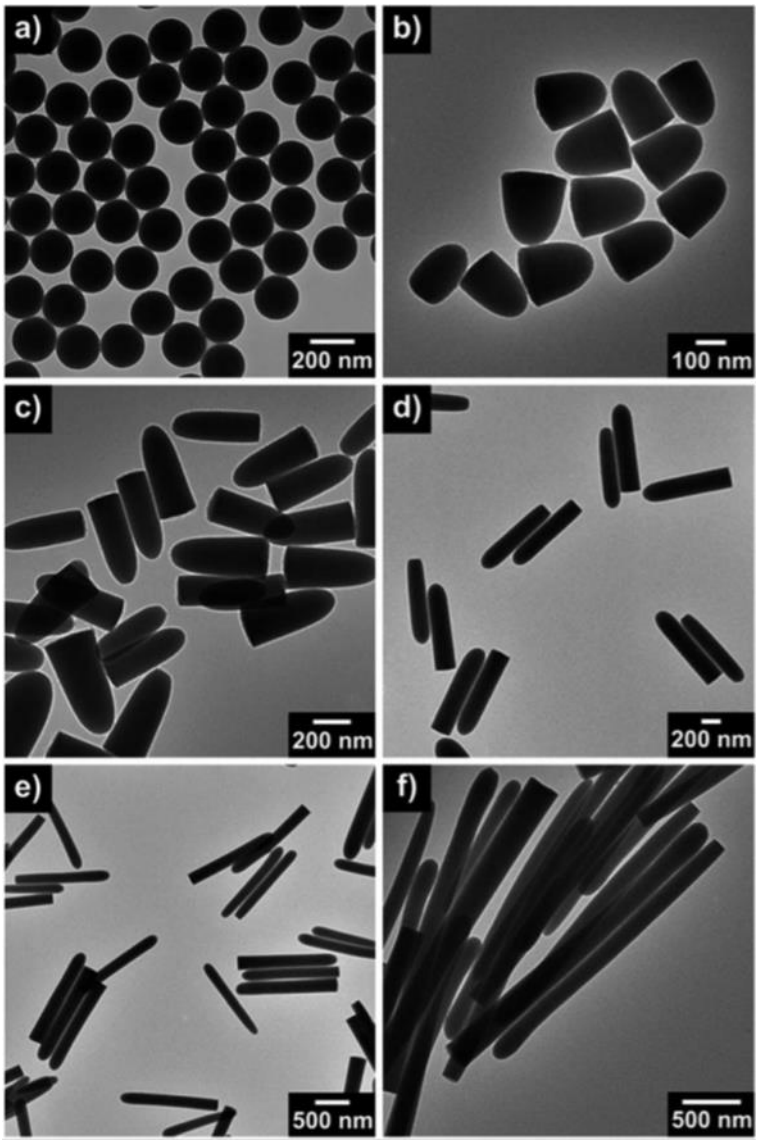

Figure 4. Transmission electron microscope images of silica nanomaterials with various structures and aspect ratio [49].

1.1.2.2. Advantages and applications of silica nanomaterial

Owing to the numerous advantages, silica nanomaterials are being applied in the wide range of nanotechnologies. There are countless advantages of silica nanomaterials, but the most important ones are listed as followings: easy synthesis method, straight forward mechanism, availability for mass-production, relatively low production cost, controllability over size and structure, high uniformity, narrow size distribution, high surface area, well-defined structure, high biocompatibility, low cytotoxicity, chemical/physical inertness, thermal stability, mechanical stability, electrical insulation, hydrophilic surface, easy surface modifications, and versatility of incorporation with other nanomaterials (**Figure 5**) [50-55]. With the aforementioned advantages, silica nanomaterials are adopted in variety of application fields, and some of typical examples are as following. Firstly, silica nanomaterials are regarded as ideal materials for high-precision *in vivo* biomedical applications including drug/gene delivery, bio-imaging, site-specific therapy, biosensor, and protein absorption [56-59]. Also, silica nanomaterials are used in the mechanical-related industry as supplement for cementitious material, additive for filler, abrasive material for chemical/mechanical polishing, corrosion resistance

material for antifouling, and dispersing/responsive materials for smart fluid [60-63]. In addition, silica nanoparticles are utilized in various physico-chemical, optical, and electrical applications including supports for catalyst, adsorption/separation materials for heavy metal ions, light scattering materials for dye-sensitized solar cell, stationary phase for high pressure liquid chromatography, photonic crystal material for nano-optics, and electrical/thermal insulating layer for electronics [64-68]. Furthermore, thanks to the versatility and easy surface modification mechanisms, silica nanomaterials are facilely incorporated and hybridized with other nanomaterials to maximize the efficiency/performance of the targeted applications (**Figure 6**) [69-71]. Taken together, numerous positive and distinctive characteristics enabled the application of silica nanomaterials into the wide spectrum of nanotechnology-related fields.

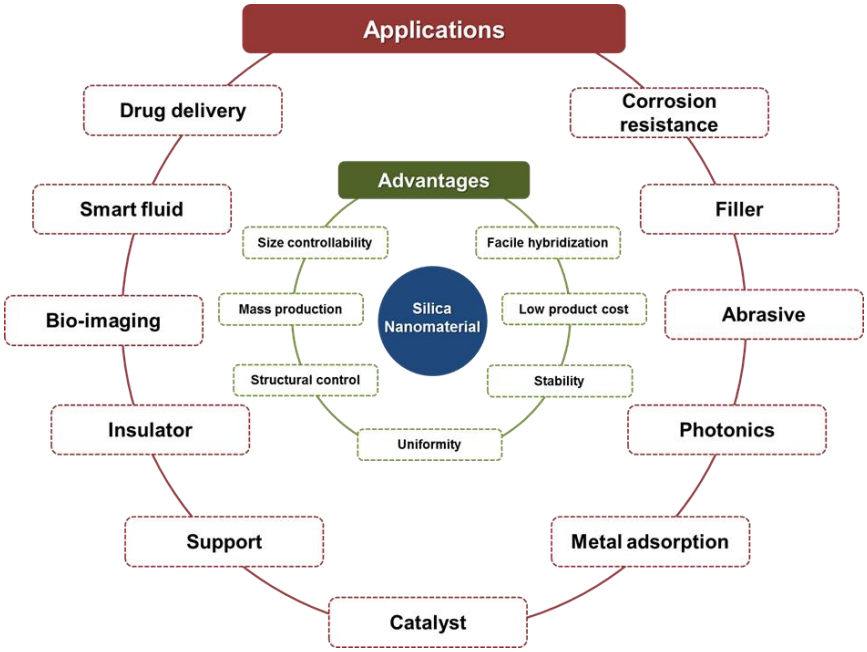

Figure 5. Summarization of various advantages silica nanomaterials and their applications.

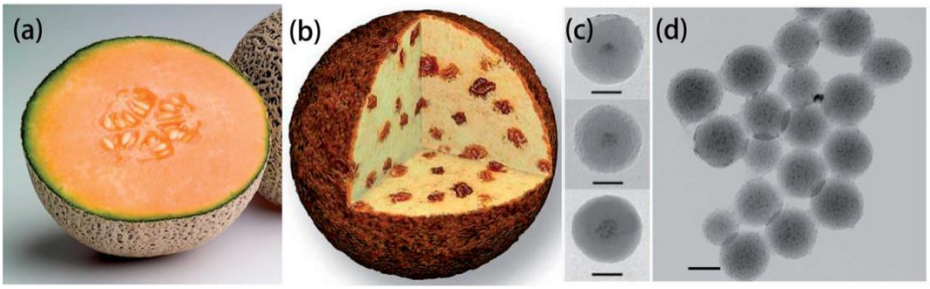

Figure 6. Typical example of hybrid silica nanomaterials with distinctive structures. Digital photographs of (a) muskmelon and (b) raisin-bun, and (c and d) correspondingly synthesized hybrid silica nanomaterials [71].

1.1.2.3. Incorporation of silica nanomaterials with other materials: silica hybrid nanomaterial

One of the most important advantage and the reason why silica nanomaterials are widely utilized in various applications fields is in its ability of facile incorporation to form silica-based hybridized nanomaterials [72,73]. Among various incorporation methods, the easiest approach to incorporate silica nanomaterials with other materials is *via* facile silane-chemistry, also referred as silylation or silanization [74,75]. Specifically, various trialkoxy silane with chemical formula of $(RO)_3$–Si–RX (RO = usually methoxy or ethoxy, RX = various functional groups) are the most commonly employed types of silanes [76]. Generally, alkoxy silane can be easily grafted or introduced onto the surface of silica nanomaterials by condensation reaction between trialkoxy group of silane and silanol (Si–OH) group of silica nanomaterials (**Figure 7**) [77]. Importantly, trialkoxy silanes can bear various functional groups like amino-, glycido-, mercapto-, chloro-, and iodo-groups in the RX position [78,79]. Consecutively, these functional groups can react, conjugate, link, and couple with numerous materials like small organic molecules, proteins, and inorganic/organic nanomaterials *via* mechanisms of organic chemistry,

electrostatic interaction, polar-polar interaction, hydrophobic effect, and so on [80]. For instance, negatively charged graphene oxide (GO) materials can be coated onto the surface of silica nanomaterials by electrostatic interactions between positively charged 3-aminoethoxypropylsilane-coated silica nanomaterials [81]. Also, photosensitive organic molecules like spiropyran can be doped onto the silica nanomaterials reaction between amino-group of silane and carboxylic groups of spiropyran [82]. Additionally, it is possible to embed hydrophobic magnetite (Fe_3O_4) nanoparticles onto the silica nanoparticles after the surface modification by amino-silylation and sequential silica layer coating [83]. Consequently, silylation method is known as the easiest and reliable way to assign targeted functionality and reactivity on the surface of silica nanomaterials for incorporation with other nanomaterials. Moreover, there are also other methods than silane-chemistry for hybridization of silica nanomaterials such as surface oxidant impregnation for polymer and conducting polymer coating, sequential sol-gel method for titania (TiO_2) and other metal oxide coating, co-precipitation/co-condensation, and in-situ polymerization methods [84-86]. Conclusively, by employing the appropriate experimental method, silica nanomaterials can be

effectively synthesized and tailored into the silica-based hybridized nanomaterials for intended processes and purposes.

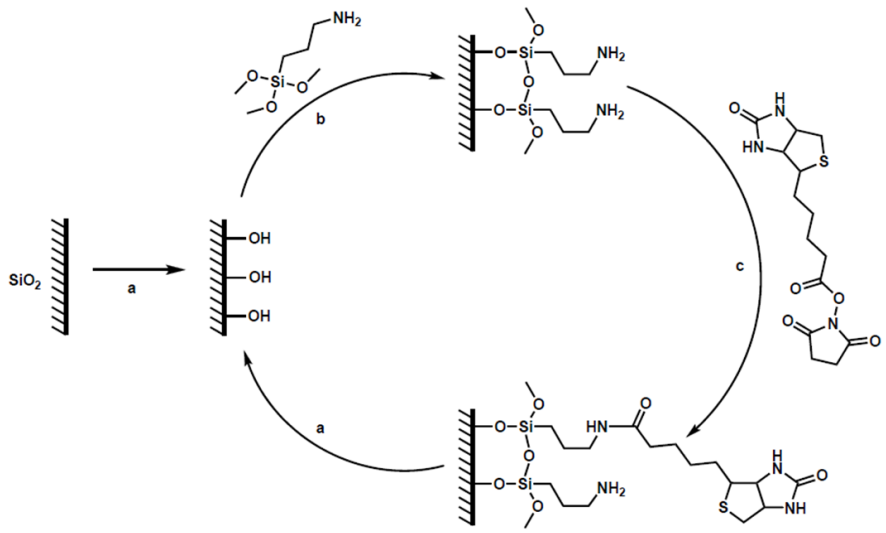

Figure 7. The schematic illustration of general mechanism of silylation reactions between silica nanomaterial and trialkoxysilane [77].

1.1.3. Smart fluid

Smart fluids (*i. e.* rheological systems), which consisted of stimuli-responsive materials, particles, and molecules (so called intelligent material) dispersed in a dispersing media with/without additive, are sensitive to specific external stimuli and surrounding environment, and able to change their mechanical and rheological properties (usually measured in shear stress or viscosity) [87]. Recently, smart fluids have received and receiving widespread interest in the various application fields due to their characteristics like fast responsivity, flexible adjustability, and fine controllability [88]. Up to now, numerous smart fluids that can respond to varieties of external stimuli including electric field, magnetic field, pH change, temperature, light, mechanical force, enzyme, and glucose have been introduced by researchers [89,90]. Among various smart fluids, however, most frequently mentioned three major classes are electro-responsive (*i. e.* electrorheological, ER) smart fluid, magneto-responsive (*i. e.* magnetorheological, MR) smart fluid, and photo-responsive (*i. e.* photorheological, PR) smart fluid responsive to external electric field (*E* field), magnetic field (*H* field), and lights (UV–VIS), respectively. Compared to other smart fluids, these three smart fluids have

advantages such as relatively easy formulation, stronger and dramatic changes in rheological/mechanical property, and high feasibility for practical applications [91]. In this regard, most of the recent research and application of smart fluids are concentrated in the aforementioned three types of smart fluid.

1.1.3.1. Nanomaterials-based smart fluid

Prior to the emergence of nanomaterials, most of the conventional stimuli-responsive materials are prepared in the size ranges of micro-scale or larger. With the growing demand for nanomaterials and advances in the related nanotechnology, nano-sized stimuli-responsive materials have attracted a great deal of interest from the researchers. Compared to conventional micromaterials-based smart fluids, the nanomaterials-based smart fluids possess more advantages in the dispersion stability, enhanced performance promoted from the fundamental/intrinsic properties of nanomaterials, and suitability for practical application needing high precisions [92]. Some examples of positive characteristics of nanomaterials over conventional micromaterials or bulk are described as followings. Specifically, nanomaterials display enhanced dispersion stability compared to

micromaterials when dispersed in the media due to the decreased size/dimension, lowered particle density, and resulting increased particle mobility [93]. If the stimuli-responsive materials are not well-distributed in the dispersing medium, smart fluids cannot properly respond to the external stimuli to leverage the intended mechanical/rheological changes. In this regard, there are plenty of examples of well-dispersed nano-sized magnetite and nano-sized conductive polymers-based smart fluids manifesting enhanced dispersion stability and stable performance under magnetic and electric fields [94-96]. Furthermore, some types of nanomaterials exhibit greatly enhanced electro-responsive activity and resulting rheological changes attributed to the increased surface/contact area and resulting interactions between particles, which are the fundamental characteristics of nanomaterials [97]. Also, since size of nanomaterials is infinitesimally small, nanomaterials-based smart fluids are able to facilitate high precision controllability in the applications like microfluidic control, robotics, and haptic devices [98,99]. However, despite the notable progress in the fields of nanomaterials-based smart fluids, there are some drawbacks such as complex synthetic method, difficulty in mass-production, and high

product cost, which need to be solved for complete replacement of conventional smart fluids in the practical industrial application.

1.1.3.2. Electro-responsive smart fluid: ER smart fluid

Electro-responsive smart fluid, also known as an electrorheological (ER) smart fluid, is composed of polarizable materials dispersed in the non-polar oil media like silicone, mineral, and other synthetic oils with high breakdown strengths [100]. The application of external *E* field causes the well-distributed materials to form numerous aligned fibril-like structures along the direction of *E* field, which suddenly induce the mechanical, rheological, and phase changes in the entire smart fluid system (**Figure 8**) [101,102]. It is known that the operation mechanism of ER smart fluid is very simple and straightforward. With the application of external *E* field, dispersed materials are polarized and able to form fibril-like structures *via* dipole–dipole interactions [103]. Along with the simple operation mechanism, ER fluids have several advantages like low operating power, reversibility, reproducibility, fast-response, and simplicity in the preparation [104,105]. Owing to their positive properties, ER smart fluids are often employed in applications like shock absorber, brakes, and

dampers [106]. According to the previous studies, various types of polarizable metal, metal oxides, carbonaceous, polymer, conducting polymer, organic molecules, and their composites are adopted as electro-responsive materials for ER smart fluid system [107,108]. There are some key factors and regulation affecting the performance of ER smart fluid. In general, dispersion stability and dielectric properties are known as the two most important factors affecting the efficiency of ER smart fluid [109]. For the former, if the electro-responsive materials are not well-distributed throughout the media due to aggregation or sedimentation, then sufficient amount of fibril-like structures cannot be formed, causing the low performance. Therefore, it is essential to enhance the dispersion stability of materials for maximizing the performance of the ER smart fluid. Previous studies have reported that the dispersion stabilities of electro-responsive materials can be enhanced by increasing the surface area/porosity, reducing the particle size/density, and also by matching the density mismatch between dispersed material and media [110,111]. For the latter, it is known that the polarizabilities of materials are determined by the dielectric properties (dielectric constant or permittivity) and its related parameters (dielectric loss and relaxation time). With the high

polarizability, ER responsive materials can construct more numbers, stronger, and fully-connected fibril-like structures to exert dramatic enhancement of performance under applied *E* field. Dielectric properties of materials can be improved by several method like increasing the surface area (polarizable area), creating a composite material, lengthening the aspect ratio, and metal doping [112]. Also, the electrical conductivity of electro-responsive materials should be taken into account with dispersion stability and dielectric property to attain stable ER performance. Generally, ER smart fluids manifest most stable performance near electrical conductivity of 1×10^{-7} S/cm [113]. If the electrical conductivity is too high then the ER smart fluid systems do not properly operate due to the occurrence of electrical short under applied *E* field. On the other hand, if the electrical conductivity is too low then the dispersed materials will not properly polarized and ER smart fluid will be inactive. Consequently, it is important to design and employ electro-responsive materials for ER smart fluid with high dispersion stability/dielectric property and adequate electrical conductivity.

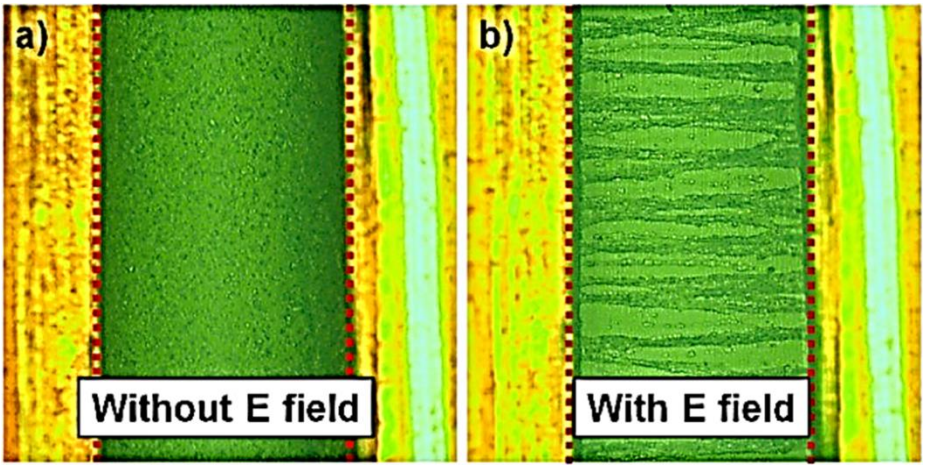

Figure 8. Fibril-like structure formations of electro-responsive materials under applied electric field [101].

1.1.3.3. Magneto-responsive smart fluid: MR smart fluid

Magneto-responsive smart fluid, also referred as a MR smart fluid, is consisted of magneto-responsive materials dispersed in various non-magnetizable mediums such as various oils, polyethers, and water [114]. The operation mechanism of MR smart fluid is also simple and quite similar to that of aforementioned ER smart fluids. Under applied *H* field, magnetic dipole-dipole moment is suddenly exerted between the magnetic materials to form fibril-like structures along the direction of *H* field, resulting in the solid-like phase transition exerting the mechanical and rheological changes (**Figure 9**) [115]. By turning off the *H* field, MR smart fluid conversely returns to the liquid-like state and mechanical strength is faded away. Therefore, MR smart fluids have similar advantages to ER smart fluids including the simple operations, fast-response, reversibility, and reproducibility [116]. However, MR smart fluids also possess distinctive characteristics of high initial yield stress, wider range of operational temperature, and wider choice of dispersing media compared with that of ER smart fluids [117,118]. With the aforementioned versatilities, MR smart fluids are widely applied in the fields of brakes, dampers, and clutches [119]. Various ferri/ferromagnetic materials like iron, magnetite

(Fe_3O_4), carbonyl iron, and iron carbonyls are adopted as magneto-responsive materials of MR smart fluids [120]. Furthermore, previous studies have set and reported some important factors and standards to attain high and stable performance of MR smart fluid. Firstly, high saturation magnetization and low coercivity/remanence are necessary for strong MR response and stable reversibility [121]. Secondly, high dispersion stability is required for effective operation of MR smart fluid by creation of strong and rigid fibril-like structures under applied *H* field [122]. Since most of magnetic materials have seriously high particle density and mass, it is hard to maintain stable dispersion stability. Dispersion stability of magnetic materials can be improved by reducing the particle size (especially in nano-scale range), adding additives like surfactant, or coating low density material [123,124]. Lastly, magnetic materials are in menace of corrosion, which significantly degrades the performance and reproducibility. Thus, protective or passive layer is usually introduced on the magnetic materials for anti-corrosion purpose and also preventing the agglomeration induced between the magnetic materials. In turn, it is required to design magneto-responsive materials and MR smart fluids by considering the aforementioned factors.

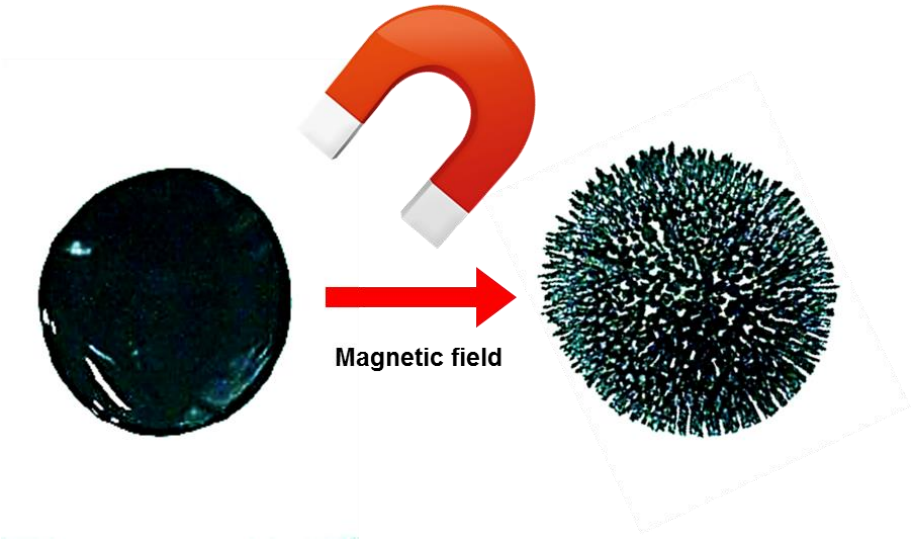

Figure 9. The mechanical and rheological changes of magneto-responsive smart fluid induced by application external magnetic field.

1.1.3.4. Photo-responsive smart fluid: PR smart fluid

Photo-responsive smart fluid, also known as PR smart fluid, is the latest smart fluid development among three major classes of smart fluids. PR smart fluids are composed of photosensitive (PR active) material with other supplementary materials like additives, gelators, and polymers dispersed in an organic media, and rheological changes are induced by lights (**Figure 10**) [125]. Various photosensitive organic molecules like azobenzene, stilbene, diarylethene, quinones, phenoxynaphthacene, and spiropyran are employed as PR active material and related photo-applications [126]. Comparing to ER and MR smart fluids, PR smart fluids have distinct advantages in spatiality, precision, and fine controllability owing to the direct pointing/positioning of light at the intended spot, readily controlled light intensity, and availability of various light source [127]. Hence, PR fluids have a great potential in fields of applications needing special spatiality including microrobotics, microvalve, flowsensors, and other microfluidic devices [128,129]. However, most of the PR active materials are complex organic materials, and it is hard to design a well-operating PR system without understanding the complicated chemistry lay behind. Thus, still relatively little attention has been

paid to PR smart fluid system than conventional ER and MR smart fluids. Also, PR smart fluids shows relatively weak mechanical and rheological changes compared to ER and MR smart fluids, which directly creates the fibril-like structure under applied field, because PR activity is solely based on the perplexed chemical interactions, micelle formation, entanglement, and photoisomerization of photosensitive molecule and other chemical additives. To formulate the well-operating PR smart fluid following factors must be taken into account. First of all, reversibility must be maintained in the PR smart fluid. It is known that the first-generation PR smart fluids are one-way active, meaning that reversibility is not attainable. In other word, after the rheological change induced by the light, first generation PR fluids are not able to revert back to the original state [130]. Thus, recent second-generation PR smart fluids are synthesized with photosensitive materials like spiropyran and azobenzene, which can reversibly photoisomerize upon exposure to UV and VIS light [131]. Secondly, simplification of operation mechanism is required. As mentioned above, the operational mechanism of PR smart fluids are complex than other smart fluids, thus it is required to invent the PR smart fluid with straightforward and simple mechanism while maintaining the

performance and reversibility.

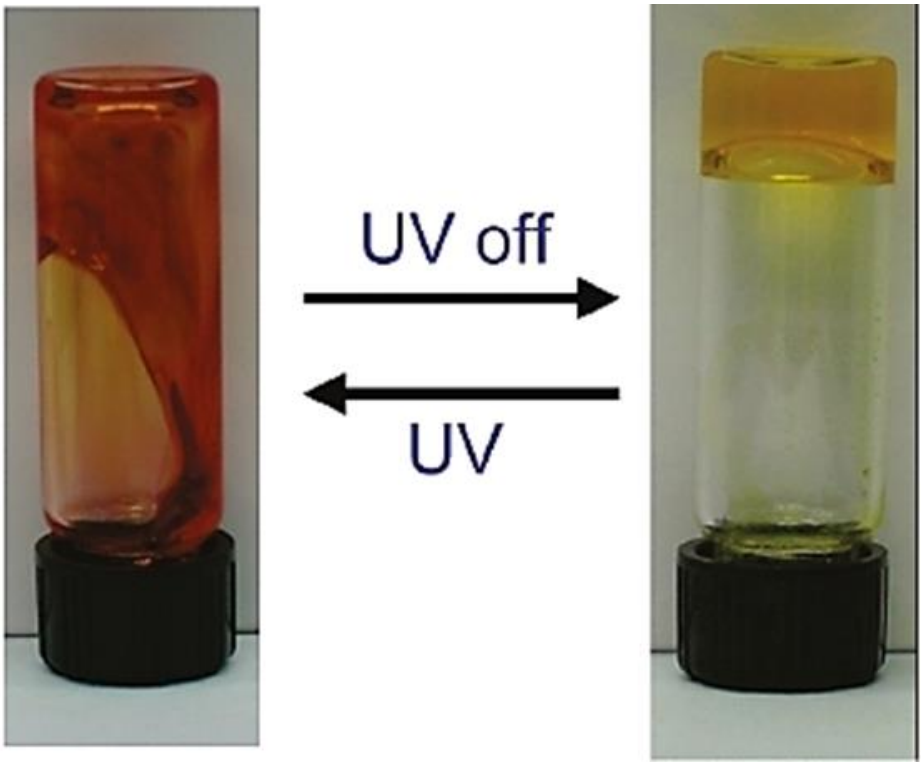

Figure 10. Reversible viscosity changes of photo-responsive smart fluid containing photosensitive spiropyran molecule under UV and VIS lights [131].

1.1.3.5. Dual stimuli-responsive smart fluid

As-mentioned three smart fluid systems have distinctive advantages but limitation, recent focus of smart fluid system is on the creation of a new fluid system responsive to multi-stimuli. Lately, electromagneto (EMR) smart fluid responsive to both *E* and *H* field is receiving a substantial interest. Especially, dual-stimuli responsive EMR smart fluids are known to possess various benefits like synergistic enhancement of mechanical and rheological property upon dual application of *E* and *H* field and reinforcing effect on the drawbacks of single-stimulus responsive materials [141]. To be more specific, ER smart fluids have some issues like low yield stress and narrow operating temperature hindering the practical commercialization. In case of MR smart fluids, problems like irreversible agglomeration, corrosion of magnetic material, and low dispersion stability are needed to be solved for practical application. In turn, various EMR materials have been synthesized and scrutinized by researchers and applied in EMR smart fluid applications [142,143]. For the preparation of EMR material, most commonly employed method is to synthesize materials as core/shell structures with different composition of inner core and outer shell [144]. By creating a core/shell material,

multi-functionality and reinforcing effect can be readily assigned and obtained. Some of previous studies have fabricated core/shell EMR materials of magnetite/polypyrrole, magnetite/polyaniline, and magnetite/silica and reported the successful EMR activity under dual application of *E* and *H* fields [145,146]. From the aforementioned studies, it is clearly observed that magnetite materials are employed as MR responsive materials, and other conducting polymers and silica materials serve as ER responsive, protective layer for magnetite, and dispersion stability enhancement materials. Accordingly, each incorporated materials successfully serve their roles and supplement the shortage of each materials. However, almost every dual stimuli-responsive smart fluid are focused and concentrated on the preparation of EMR smart fluids. Correspondingly, there is a necessity and better understanding for invention of multi-stimuli-responsive materials and smart fluid systems other than EMR smart fluid responsive to *E* field and *H* field.

1.2. Objectives and Outlines

1.2.1. Objectives

The aim of this dissertation is to describe the methodologies for preparation of silica nanomaterials-based ER, EMR, and EPR smart fluids susceptible to various external stimuli of *E* field, *H* field, and UV–VIS lights. In detail, silica nanomaterials are tailored in various morphologies, composited with magnetite, and functionalized with photosensitive spiropyran molecules to enhance the responsivity toward *E* field, *H* field, and lights. Sequentially, complete development and formulation strategy of each type of smart fluids using silica and derived nanomaterials are thoroughly illustrated. Each type of smart fluids are applied as both single stimuli-responsive ER, MR, and PR smart fluid and also as dual stimuli-responsive EMR and EPR smart fluids. Furthermore, operating mechanism and underlying theory of each types of smart fluid system under various external stimuli are systematically scrutinized.

1.2.2. Outlines

This dissertation focused on the formulation of various silica nanomaterials-based smart fluids and investigations of their practical

performances as ER, MR, PR, EMR, and EPR smart fluids. This dissertation involves the following subtopic:

I. Fabrication of $mSiO_2$ nanomaterials with different *L/D* for ER smart fluid application

II. Fabrication of multi-layered $SiO_2/TiO_2@Fe_3O_4/SiO_2$ nanomaterials for dual EMR smart fluid application

III. Fabrication of photosensitive SP-SiO_2 nanomaterials for dual EPR smar fluid application.

A detailed outline of the study is as follows:

1. Multi-gram scales of mesoporous silica ($mSiO_2$) nanomaterials with different aspect ratio (*L/D*) are successfully synthesized as electro-responsive materials by the modified Stöber method using CTAB as a surfactant. The *L/D* of $mSiO_2$ nanomaterials are readily fabricated as 1, 2, and 4 by changing the amount of added water while fixing the amount of all other reagents. As-synthesized $mSiO_2$ nanomaterials with different *L/D* are prepared as electro-responsive (ER) smart fluids by dispersing into the silicone oil. The ER activities of $mSiO_2$

nanomaterials with different *L/D*-based ER smart fluids are investigated under various experimental conditions as a function of shear rate and *E* field strength of ER smart fluid. Also, *E* field on-off test is conducted to verify the stabilities. From an in-depth analysis of ER smart fluid, it is revealed that each mSiO_2 nanomaterials-based ER fluids display high ER activity owing to the mesoporous nature (high surface area and porosity) of materials, which eventually lead to the improvement of dielectric properties. Furthermore, ER performance of ER smart fluids increased with the increased *L/D* of mSiO_2 nanomaterials. Such phenomenon is attributed to the enhancement in the dielectric properties and additional geometric effects of mechanical stability and flow resistance provided by the increments in *L/D*. Consequently, these experimental results of thorough and meticulous investigation may offer an opportunity for facile synthesis methods for formulation of high performance ER smart fluid.

2. Core/shell structured and multi-layered magnetite-embedded silica/titania nanoparticle-coated with outermost silica shell (SiO_2/TiO_2@Fe_3O_4/SiO_2) nanomaterial is successfully synthesized by combinations of sequential experimental methods like thermal

decomposition, sol-gel, and silylation methods. Each synthesis steps have added magneto- and electro-responsivity along with other positive features. In particular, core SiO_2/TiO_2 nanomaterial is prepared by combination of Stöber method and sol-gel method, which served as ER and dielectric property enhancement material. Continuously, numerous numbers of uniformly synthesized Fe_3O_4 nanomaterials are embedded onto the SiO_2/TiO_2 *via* silylation, which added the strong magneto-responsive (MR) characteristics. Lastly, thin SiO_2 shell was coated as finishing materials to integrate the advantages like dispersion stability, corrosion resistance, and prevention of irreversible flocculation during the MR process. The resulting core/shell structured $SiO_2/TiO_2@Fe_3O_4/SiO_2$ nanomaterials exhibit high responsivities as a single stimuli responsive MR and ER smart fluids under *H* and *E* field, respectively. Specifically, the MR and ER activities of $SiO_2/TiO_2@Fe_3O_4/SiO_2$-based smart fluids are examined by various tests including as a function of shear rates/strength of *H* and *E* field and on-off tests of external fields. Moreover, $SiO_2/TiO_2@Fe_3O_4/SiO_2$-based smart fluids showed synergistic electromagneto-responsive (EMR) characteristics under simultaneous application of *H* and *E* fields. In this regard, study

reported in this section provides a facile route and thorough understandings of synthesis of dual-stimuli EMR materials and their practical application.

3. In this section, electrophotorheological (EPR) smart fluid, which is dually responsive to ultra-violet and visible light (UV–VIS) and *E* fields, is carefully designed by adding spiropyran-doped silica (SP-SiO_2) nanomaterials into the dispersing medium specially formulated for EPR smart fluid. Particularly, SP molecules are easily coated onto the SiO_2 nanomaterials by silylation method. It is known that the photosensitive SP molecule are able to photo-isomerize under UV light as ring-opened zwitterionic merocyanine (MC) form, and reverts back to original form under VIS light, adding the high reversibility and photo-responsive (PR) characteristics to bearing EPR smart fluid. Also, EPR dispersing medium, composed of commercially available mineral oil and zwitterionic lecithin additive at the right concentration, greatly enhanced the dispersion stability of SP-SiO_2 nanomaterial and chemically enabled the EPR activity. Notably, UV-induced EPR system manifests increased shear stress induced by the interactions between MC and lecithin molecule, and decreased shear stress under

VIS light to demonstrate the reversible PR activity. Moreover, EPR fluid shows a positive ER activity under applied *E* field strength without any short circuit. Finally, even more increased shear stress is observed than single PR activity under dual application of UV light and *E* field attributed to the combined contributions from PR and ER activity. Consequently, EPR smart fluid reported in this section successfully derives the advantages of the PR and ER into one place, and demonstrate the synergistic effect of PR and ER smart fluids.

2. Experimental Details

2.1. Fabrication of $mSiO_2$ nanomaterials with different *L/D* for ER smart fluid application

2.1.1. Synthesis of $mSiO_2$ nanomaterials with different *L/D*

Three $mSiO_2$ nanomaterials with different *L/D* were prepared by the modified Stöber method [147]. Geometrical shape and *L/D* of $mSiO_2$ nanomaterials were easily controlled by changing the added amount of water while fixing the amount of other reagents. For the synthesis of $mSiO_2$ nanomaterials with *L/D* of 1 (sphere shape), water (30.0 mL), ethyl alcohol (EtOH, 5.0 mL), and ammonia solution (NH_4OH, 1.74 mL) were mixed by vigorous stirring. Sequentially, cetrimonium bromide (CTAB, 0.47 g) was added into the mixture and stirred for another 5 min. Succedingly, tetraethylortho silicate (TEOS, 1.0 mL) was injected into the mixture and reaction was proceed for 2 h. The resulting white cloudy solution was centrifuged with DI water and EtOH to collect the $mSiO_2$ nanomaterials. The resulting $mSiO_2$ nanomaterials were calcined at 600 ℃ for 2 h to remove the residues. The $mSiO_2$ nanomaterials with *L/D* of 2 (short-rod) and 4 (long-rod)

were fabricated by the same aforementioned experimental procedure, but using 131.0 mL and 64.0 mL of DI water, respectively.

2.1.2. Characteristic analysis of $mSiO_2$ nanomaterials with different *L/D*

The structures of three types of $mSiO_2$ nanomaterials were observed by transmission electron microscope (TEM) and field emission-scanning electron microscope (FE–SEM) characterization using JEM–200CX (JEOL) and JEOL–6700 (JEOL), respectively. Porosity of various $mSiO_2$ nanomaterials were determined by Barrett–Joyner–Halenda (BJH) and Brunauer–Emmett–Teller (BET) calculated from the N_2-sorption curve using an ASAP–2010 (Micrometrics). The fourier-transform infrared (FT-IR) spectra of $mSiO_2$ nanomaterials were acquired by FT-IR spectrum 400 system (PerkinElmer). The crystallinity of $mSiO_2$ nanomaterials were analyzed by determining the X-ray diffraction patterns using M18XHF–SRA (MAC Science Co.) and AXIS–His (KRATOS) spectrometers. The dielectric properties (permittivity and dielectric loss) of $mSiO_2$ nanomaterials-based ER smart fluids were examined using an impedance spectroscopy (Solatron–1260) coupled with dielectric interface

analyzer (Solatron–1296). The electrical conductivities of $mSiO_2$ nanomaterials were determined using physical properties measuring system (PPMS-14, Quantum design).

2.1.3. Electro-responsive activities of $mSiO_2$ nanomaterials with different *L/D*-based ER smart fluid

The $mSiO_2$-nanomaterials-based ER smart fluids are formulated according to the following procedure. Firstly, the $mSiO_2$-nanomaterials were dried in oven at 150 ℃ for 48 h to completely remove the moistures. Dried $mSiO_2$-nanomaterials were dispersed in 10.0 mL of silicone oil [poly(methylphenylsiloxane), viscosity = 100 cSt] by mechanical grinding (mortar and pestle) and magnetic stirring for overnight. The ER smart fluids were prepared as concentration of 3.0 wt% and no further additives were added. The electro-responsive activity of $mSiO_2$-nanomaterials-based ER smart fluids were investigated by AR2000 rheometer (TA instruments) coupled with components of cup (height: 30.0 mm and diameter: 30.0 mm), a concentric cylinder conical geometry (internal height: 30.0 mm, diameter: 28.0 mm), and Trek677B voltage generator. To prevent the physical interference, void gap was set between the cup and geometry

as 2.0 mm. The electro-responsive measurement was started by pouring the as-prepared ER smart fluids (3.0 wt%, 10.0 mL) in the cup and inserting a rotor. Before applying the *E* field, the mechanical shear (shear rate of 10.0 s^{-1}) was applied for 10 min to attain well-distributed state of mSiO_2 nanomaterials throughout the silicone oil. Finally, targeted strength of external *E* fields was applied to examine the ER activity of mSiO_2 nanomaterials-based ER smart fluids. Furthermore, the leakage currents (or leaking current) of ER smart fluids were directly measured from the voltage generator for the prevention of short circuit. The rheological measurements were repeated for three times to ensure the consistency of data.

2.2. Fabrication of $SiO_2/TiO_2@Fe_3O_4/SiO_2$ nanomaterials for EMR smart fluid application

2.2.1. Fabrication of SiO_2/TiO_2 core/shell nanomaterial

The SiO_2/TiO_2 core/shell nanomaterial was prepared by two step synthesis method. Firstly, core SiO_2 was synthesized according to the typical Stöber method and outer TiO_2 shell was introduced by the sol-gel method. In a typical synthesis of SiO_2 nanomaterial, EtOH (70.0 mL), water (3.0 mL), and NH_4OH (2.7 mL) were vigorously mixed by

the magnetic stirring for 20 min. Continuously, TEOS (2.1 mL) was drop-wisely injected into the mixture, and reaction was proceeded for 12 h while maintaining the temperature at 60 ℃. The resulting core SiO_2 nanomaterials were washed with DI water and EtOH for several times. For the continuous coating process of TiO_2 shell, as-synthesized SiO_2 nanomaterials were re-dispersed into EtOH (100.0 mL). And then, separately prepared solution consisted of titanium isopropoxide (TTIP, 6.0 mL), EtOH (36.0 mL), and acetonitrile (15.0 mL) was drop-wisely added to the SiO_2 colloidal EtOH solution. The sol-gel reaction for introducing TiO_2 shell was continued for 12 h with vigorous stirring at 4℃. Finally, white cloudy solution was centrifuged several times with EtOH and water to obtain the SiO_2/TiO_2 core/shell nanomaterials.

2.2.2. Fabrication of Fe_3O_4 nanomaterial

Uniform Fe_3O_4 nanomaterials with the size of *ca.* 12 nm were prepared by thermal decomposition method. In a typical synthesis of Fe_3O_4 nanomaterials, iron (III) chloride hexahydrate ($FeCl_3 \cdot 6H_2O$, 2.7 g) and sodium oleate (9.2 g) were dissolved into the mixture of DI water (15.0 mL), EtOH (20.0 mL), and n-hexane (35.0 mL) by

vigorous magnetic stirring. With the constant stirring, the resulting mixture was heated to 68 ℃, and reaction was kept for 4 h. After the heating step, brownish upper organic layer was washed three times with DI water, and heat (75 ℃) was re-applied to evaporate the n-hexane solution. After the evaporation process, iron-oleate complex was obtained. Continuously, iron-oleate complex (9.0 g) and oleic acid (1.4 g) were mixed into 1-octadecene (100.0 g). Prior to the thermal decomposition, aforementioned mixture was placed into the three neck flask with constant stirring and nitrogen gas purging. Under the nitrogen condition, the thermal decomposition of iron-oleate mixture was carried out by a steady increment of temperature upto 320 ℃ (heating rate of 3.2 ℃ min^{-1}). The thermal decomposition reaction was maintained for 30 min, and cooled down to room temperature. After the cooling process, Fe_3O_4 nanomaterials were precipitated by adding EtOH (300 mL) solution. The Fe_3O_4 nanomaterials were collected by the centrifugation, and dried in oven (120 ℃) for overnight to completely remove the moistures. Finally, Fe_3O_4 nanomaterials were dissolved in the cyclohexane (~0.5 wt%) and stored.

2.2.3. Fabrication of multi-layered $SiO_2/TiO_2@Fe_3O_4/SiO_2$ nanomaterial

The multi-layered $SiO_2/TiO_2@Fe_3O_4/SiO_2$ nanomaterial was synthesized according to the two step experimental methods of embedment of Fe_3O_4 nanomaterials on the SiO_2/TiO_2 core/shell nanomaterials and outermost SiO_2 shell coating process. The simple silylation method is employed as strategy for Fe_3O_4 nanomaterial embedding process onto the SiO_2/TiO_2 core/shell nanomaterials. Firstly, as-synthesized SiO_2/TiO_2 core/shell nanomaterials (1.0 g) were dispersed in EtOH (100.0 mL) solution, and 3-aminopropyltrimethoxysilane (APTES, 0.5 mL) was drop-wisely added. After 20 min of the reaction (allowing the condensation and hydrolysis of silane), as-prepared Fe_3O_4 colloidal solution (5.0 mL) was injected into the mixture, and ligand exchange reaction was continued for 6 h. Sequentially, NH_4OH (1.0 mL) was added to the above solution as a catalyst. And then, TEOS (2.5 mL) was added by the equivalently fractionated dropping method (0.5 mL per 2 h). After 10 h of injections, the reaction was continued for additional 2 h. Finally, brownish and cloudy solution was centrifuged and $SiO_2/TiO_2@Fe_3O_4/SiO_2$ nanomaterials were collected. The resulting

$SiO_2/TiO_2@Fe_3O_4/SiO_2$ nanomaterials were washed several times with EtOH and dried in the oven (120 ℃) for overnight.

2.2.4. Characteristic analysis of multi-layered $SiO_2/TiO_2@Fe_3O_4/SiO_2$ nanomaterial

The morphologies of SiO_2/TiO_2 core/shell, $SiO_2/TiO_2@Fe_3O_4$, and $SiO_2/TiO_2@Fe_3O_4/SiO_2$ nanomaterials were observed by the TEM analysis using JEM-200CX (JEOL). The elemental compositions (Si, Ti, O, and Fe) of nanomaterials were analyzed by the STEM elemental mapping obtained from the Tecnai F20 (FEI). The fourier-transform infrared (FT-IR) spectra of nanomaterials were examined using the FT-IR spectrum 400 instrument (PerkinElmer). The X-ray diffraction patterns of nanomaterials were explored by the M18XHF–SRA (MAC Science Co.) and AXIS–His (KRATOS) spectrometers for determination of crystallinities. The magnetization-related measurements (hysteresis loop and saturation magnetization) were assessed by the PPMS-14 (Quantum design).

2.2.5. Magneto-, electro-, and electromagneto-responsive activities of $SiO_2/TiO_2@Fe_3O_4/SiO_2$ nanomaterials-based EMR smart fluid

For the measurement of magneto-responsive (MR), electro-responsive (ER), and electromagneto-responsive (EMR) activities, the concentrations of smart fluids were differently set to attain maximized performances. In case of ER and EMR activity determination, smart fluids were formulated by dispersing nanomaterials into the silicone oil (100 cSt) with concentrations of 20.0 vol%. On the other hand, smart fluids were prepared as 50.0 vol% for the MR activity determination. For the preparation of smart fluids, proper amount of Fe_3O_4, $SiO_2/TiO_2@Fe_3O_4$, and $SiO_2/TiO_2@Fe_3O_4/SiO_2$ nanomaterials and silicone oil were well-mixed by the mechanical grinding (mortar and pestle) and sonication. After preparing the smart fluid, the MR activities of as-prepared smart fluids were investigated using a MCR301 rheometer installed with a parallel plate (d: 20.0 mm) and magnetic field generator (PS-MRD, Anton Paar). The gap distance between loading plate and parallel plate were set to 1.0 mm. Prior to measuring the MR activity mechanical shear (shear rate of 10.0 s^{-1}) was applied to ensure the homogeneous state of the smart fluids. The

ER activities of smart fluids were measured by AR2000 rheometer (TA instrument) equipped with a cup (diameter: 30.0 mm and height: 30.0 mm) and concentric cylinder type of geometry (diameter: 28.0 mm and height: 30.0 mm). The external *E* field was applied by the high voltage generator (TREK677B). The gap distance between the cup and geometry was set to 2.0 mm for the prevention of physical interferences. Prior to measuring the ER activities, smart fluids were well dispersed by applying the mechanical shear (shear rate of 10.0 s^{-1}) for 10 min. The dual EMR activities of smart fluids were investigated by using the AR2000 rheometer (TA instrument) equipped with cup (diameter: 30.0 mm and height: 30.0 mm) and concentric cylinder type of geometry (diameter: 28.0 mm and height: 30.0 mm). For the EMR measurement, *E* and *H* fields were simultaneously applied in the parallel/perpendicular directions. Prior to applying the external fields, 10 min of mechanical shear (shear rate of 10.0 s^{-1}) was applied to EMR smart fluid to ensure the homogeneous distribution of dispersed materials throughout the silicone oil medium.

2.3. Fabrication of SP-SiO_2 nanomaterials for EPR smart fluid application

2.3.1. Fabrication of SP-SiO_2 nanomaterials

Fabrication of SP-SiO_2 nanomaterials started with the preparation of core SiO_2 nanomaterials. Firstly, 50 nm-sized core SiO_2 nanomaterial was synthesized by the well-known Stöber method. In a typical synthesis of SiO_2 nanomaterials, DI water (1.6 mL), EtOH (80.0 mL), and NH_4OH (2.2 mL) were mixed by the magnetic stirring. Subsequently, TEOS (2.1 mL) was added into the mixture solution, and reaction was kept for 24 h at 60 ℃. The resulting SiO_2 nanomaterials were centrifuged and washed with EtOH for several times. For the silylation, SiO_2 nanomaterials were well dispersed into the water (10 mL) by sonication for 6 h. Continuously, EtOH (100.0 mL) was added to the as-prepared SiO_2 colloidal solution, and (3-glycidyloxypropyl)trimethoxysilane (GPTS, 2.5 mL) was added in a dropwise manner with vigorous magnetic stirring. The thickness of silane shell on the SiO_2 nanomaterials was controlled by varying the reaction times from 1 to 24 h. The resulting silylated-SiO_2 nanomaterials were retrieved by the centrifugation, and quickly re-dispersed into the EtOH (35.0 mL) by pipetting and sonication for 5 h.

Finally, 1-(2-Hydroxyethyl)-3,3-dimethylindolino-6' nitrobenzo pyrylospiran (SP molecule, 100.0 mg) was added to the silylated-SiO_2 mixture, and reaction vessel was wrapped with the aluminum foil to avoid the source of any external light. The reaction was continued for 24 h, and resulting SP-SiO_2 nanomaterials were collected by centrifugation using EtOH (30.0 mL). While collecting the SP-SiO_2 nanomaterials, supernatant solution was kept for the calculation of unreacted SP molecule, which was used for back-calculation of attached amount of SP molecule on the SP-SiO_2 nanomaterials. Furthermore, SiO_2 nanomaterials with the size of 100 and 250 nm were synthesized by changing the reaction parameters like temperature and added amount of reactant for the comparison purpose. For the preparation of 100 nm-sized SiO_2 nanomaterials, all other experimental steps are similar to the pre-mentioned 50 nm SiO_2 nanomaterials, but the reaction temperature was lowered to room temperature (25 ℃). For the synthesis of 250 nm-sized SiO_2 nanomaterials, added amount of reagent was changed as followings. The reaction was proceeded by mixing EtOH (200.0 mL), DI water (32.0 mL), and NH_4OH (42.3 mL). And then, TEOS (21.0 mL) was injected to the mixture, and 24 h reaction was carried at 25 ℃.

2.3.2. Formulation of dispersing medium

The EPR smart fluid (3.0 wt%) was formulated by following procedure. Firstly, SP-SiO_2 nanomaterials (0.3 g) were mechanically ground using a mortal and pestle. And then, ground SP-SiO_2 nanomaterials were dispersed into the mixture of mineral oil (11.0 mL) and lecithin molecules (0.185 g, equivalent to 2.36×10^{-4} moles) by magnetic stirring and sonication for 12 h and 1 h, respectively. There were no additives further added to the EPR smart fluid. The ER smart fluid without lecithin molecule (3.0 wt%) was formulated by the same procedures of adding finely ground SiO_2, silylated-SiO_2, and SP-SiO_2 nanomaterials (0.3 g) into the mineral oil (10 mL) by magnetic stirring for and sonication.

2.3.3. Characteristic analysis of SP-SiO_2 nanomaterials

The structures of SiO_2, silylated-SiO_2, and SP-SiO_2 nanoparticles were verified by the TEM observation and FE-SEM analysis using JEM-200CX (JEOL) and JEOL-6700 (JEOL), respectively. The porosity and BET surface area of as-synthesized nanomaterials were measured by BJH calculations obtained from the ASAP-2010 (Micrometrics). The atomic compositions (Si, N, and O atoms) of

nanomaterials were analyzed by the STEM observation using Tecnai F20 (FEI) installed with Gatan image filter. The nuclear magnetic resonance (NMR) peaks of GPTS silane-reacted SP molecule was determined by the proton (^{1}H) Avance-300 NMR (Bruker) instrument. [NMR peak data for GPTS silane-reacted SP molecule: ^{1}H NMR (300 MHz, MeOD) δ = 0.94 (m, 2H), 1.20 (s, 6H) 1.37 (m, 2H), 3.26–3.41 (m, 15H), 3.64–3.75 (m, 4H) 4.23–4.27 (m, 1H), 6.02–6.05 (d, 1H), 6.65–6.68 (d, 1H), 6.79–6.86 (m, 2H), 7.06–7.17 (m, 3H), 7.65–7.72 (d, 1H), 8.11–8.12 (d, 1H)]. The viscosities of lecithin dispersed mineral oils (dispersing medium for EPR smart fluid) were measured by AR2000 rheometer (TA instruments) equipped with parallel-plate (geometry diameter: 20.0 mm). The leakage currents of lecithin dispersed mineral oils were directly acquired from the high voltage generator (Trek677B). The UV–VIS absorption peaks of EPR smart fluid was determined by the Lambda 35 UV/VIS spectrophotometer (Perkin Elmer). The dielectric properties (permittivity and dielectric loss factor) of EPR and ER smart fluid were obtained using a dielectric interface (Solatron 1296) coupled with the frequency response analyzer (Solartron 1260). The real time PR activity under UV/VIS lights and fibril-like structure formation of EPR smart fluid under conditions of

VIS + *E* field and UV + *E* field was analyzed using the Nikon Lv100 optical microscope (OM) instrument (Nikon). The doping levels of SP molecules on the different-sized SiO_2 nanomaterials were determined by the following method. Firstly, the SP-SiO_2 nanoparticles were collected and the supernatant solutions (*ca.* 40 mL) were kept as previously discussed. It was expected that any unreacted SP molecules may left in the supernatant solution, therefore the amount of SP molecules attatched on SiO_2 nanomaterials may reversely calculated. Retrieved supernatant solution (0.5 mL) was diluted by mixing with the EtOH (2.5 mL). For the comparison and calculation, reference solution was formulated by dispersing SP molecules (100 mg) into the exact amount of the EtOH (40 mL), which was intentionally controlled as same concentrations of SP molecule used for the preparation of SP-SiO_2 nanoparticles. Similarly, this reference solution (0.5 mL) was diluted with EtOH (2.5 mL). The UV–VIS absorption spectra of the diluted supernatant solution and newly prepared reference solutions were determined using Lambda 35 UV/VIS spectrometer (PerkinElmer). The absorbance of the supernatant solution was compared with that of the reference solution to calculate the excess amount of SP molecule according to the following calculation relation:

$$A_{supernatant} / m_{supernatant\ SP} = A_{reference} / m_{reference\ SP},$$

From the above relation, $A_{supernatant}$ is the absorbance of the supernatant solution, $m_{supernatant\ SP}$ is the amount of excess (unreacted) SP molecules left in the supernatant solution, $A_{reference}$ is the absorbance of the reference and $m_{reference\ SP}$ is the amount of SP molecules in the reference solution (100 mg). By solving above relation, the amount of excess SP molecules in the supernatant solution was determined. Lastly, the mass of SP molecules coated on the SP-SiO_2 nanoparticles, m_{SP}, was calculated by solving the following relation:

$$m_{SP} = m_{total\ SP} - m_{supernatant\ SP},$$

where $m_{total\ SP}$ is fixed as known mass (100 mg) of SP molecule employed in the synthesis method.

2.3.4. Photo-, electro-, and electrophoto-responsive activities of SP-SiO_2 nanomaterials-based EPR smart fluid

All of photo-responsive (PR), electro-responsive (ER), and electrophoto-responsive (EPR) activities of EPR smart fluids were determined using a AR2000 rheometer (TA instruments) equipped

with cup (height: 30.0 mm and diameter: 30.0 mm) and concentric cylinder geometry (internal diameter: 28.0 mm and height: 30.0 mm). The external stimuli of *E* field, UV light, and VIS light were generated by using Trek677B high voltage generator, ENF-240C UV lamp (4 W cm^{-2}), and Siriu 300P xenon lamp (Zolix), respectively. The measurements of PR, ER, and EPR activities started with pouring the as-synthesized EPR or ER smart fluid (3.0 wt%, 10 mL) into a cup and inserting the concentric cylinder geometry. Before applying the external stimuli, mechanical shear (with rate of 10.0 s^{-1}) was applied for 20 min to attain well-dispersed state of nanomaterials in mineral oil. Finally, external stimuli were applied, and targeted ER, PR or EPR activities of EPR smart fluid were measured.

3. Results and Discussions

3.1. Fabrication of $mSiO_2$ nanomaterials with different *L/D* for ER smart fluid application

3.1.1. Synthesis of $mSiO_2$ nanomaterials with different *L/D*

The schematic illustration for the synthesis of $mSiO_2$ nanomaterials with different *L/D* was described in **Figure 11**. The *L/D* of $mSiO_2$ nanomaterials were readily controlled by varying the amount of added water. The structures of various $mSiO_2$ nanomaterials were examined by the TEM and FE-SEM analysis, as represented in **Figure 12**. For *L/D* of 1, uniform and spherical $mSiO_2$ nanomaterials were synthesized having a diameter of *ca.* 70 nm. Two other $mSiO_2$ nanomaterials with *L/D* of 2 and 4 showed similar diameters of *ca.* 60 nm, but different lengths of *ca.* 120 nm and *ca.* 240 nm respectively. Moreover, well-defined structures of $mSiO_2$ nanomaterials with different *L/D* were further verified by the FE-SEM analysis, as shown in **Figure 13**.

Accordingly, it can be deduced that the molar ratio of water plays a key role in the modification of *L/D* and evolutionary mechanism for morphology of $mSiO_2$ nanomaterials. Particularly, the main driving

forces for the reaction of $mSiO_2$ nanomaterials have changed from the silica-driven to silicate-surfactant micelle formation by increasing the amount of water. Therefore, starting spherical morphology of $mSiO_2$ nanomaterials gradually changed to a rod-like structure with higher *L/D* by increasing the added amount of water. Such anisotropic growth resulted from the dilution of silica and the surfactants (CTAB). To be more specific, when the amount of added water increase, then the growth of silica was suppressed in the relatively limited region owing to the directional deposition of silica. Notably, further increment in the amount of water re-decreases the *L/D* of $mSiO_2$ nanomaterial attributed to the decreased concentrations of the silica precursor. More detailed mechanisms for structural and length changes of $mSiO_2$ nanomaterials were described in the previous study [148,149]. In this study, the *L/D* of spherical and two rod-like $mSiO_2$ nanomaterials were precisely controlled to 1 (sphere), 2 (short-rod), and 4 (long-rod) by considering the pre-mentioned mechanisms of $mSiO_2$ nanomaterials. The physical parameters of three different kinds of $mSiO_2$ nanomaterials were listed in **Table 1**.

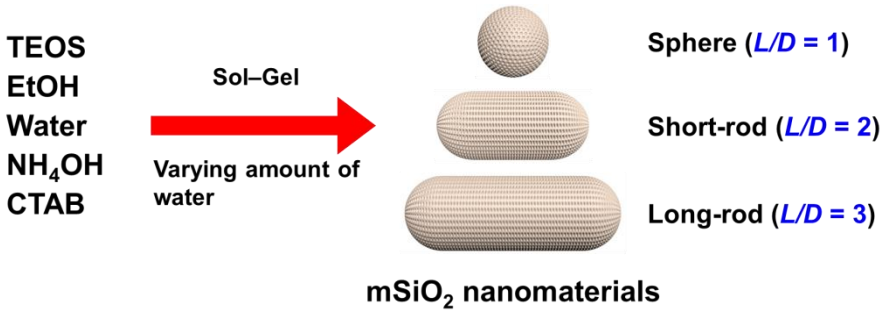

Figure 11. Schematic illustration of the synthesis of $mSiO_2$ nanomaterials with different *L/D*.

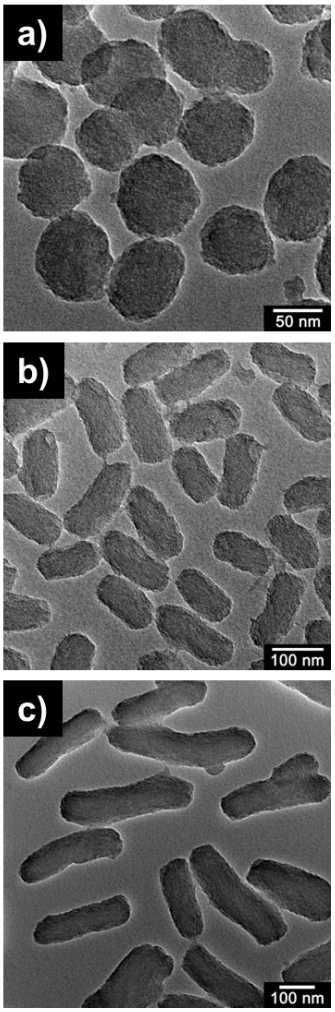

Figure 12. TEM micrographs of $mSiO_2$ nanomaterials with *L/D* of (a) 1 (sphere), 2 (short rod), and 4 (long rod).

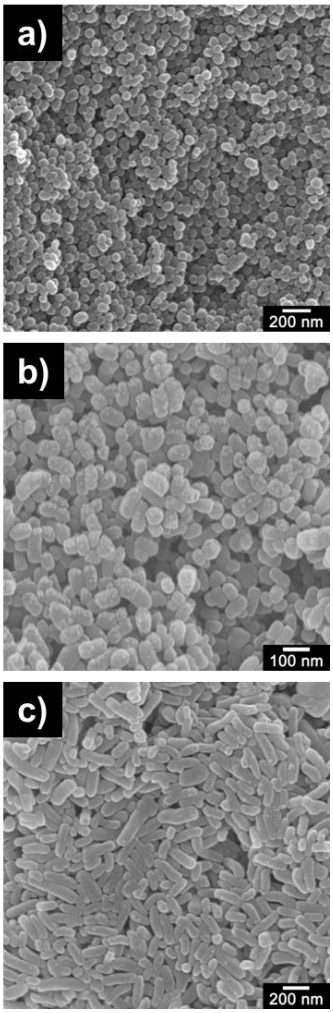

Figure 13. FE-SEM micrographs of $mSiO_2$ nanomaterials with *L/D* of (a) 1 (sphere), 2 (short rod), and 4 (long rod).

Table 1. Physical summary of $mSiO_2$ nanomaterials with different *L/D*.

Morphology	Length (*L*)[a]	Diameter (*D*)[a]	Aspect ratio (*L/D*)[b]
Sphere	*ca.* 70 nm	*ca.* 70 nm	1
Short rod	*ca.* 120 nm	*ca.* 60 nm	2
Long rod	*ca.* 240 nm	*ca.* 60 nm	4

[a] The average length and diameter of various $mSiO_2$ nanomaterials were ensured by TEM analysis (more than 50 nanomaterials were evaluated).

[b] The *L/D* was determined by dividing length by diameter of nanomaterials.

3.1.2. Characteristic analysis of $mSiO_2$ nanomaterials with different *L/D*

The porosity and porous natures of $mSiO_2$ nanomaterials were examined by the BET analysis calculated from the nitrogen adsorption-desorption (N_2-sorption) isotherms. From the N_2-sorption curves of $mSiO_2$ nanomaterials described in **Figure 14**, it was clearly observed that all $mSiO_2$ nanomaterials exhibited typical type IV hysteresis, indicating the porous natures. Also, the pore sizes of all $mSiO_2$ nanomaterials were determined to be *ca.* 2 nm, as shown in **Figure 15**. The detailed porosity (pore size and volume) and BET surface area of $mSiO_2$ nanomaterials are listed in **Table 2**. It was noticeable that the surface area of the three types of $mSiO_2$ nanomaterials were conspicuously high compared to the nonporous (conventional) SiO_2 nanomaterials with similar diameters attributed to the presence of numerous mesopores [150]. Continuously, crystallinities of $mSiO_2$ nanomaterials were determined by the XRD analysis (**Figure 16**). In particular, all of $mSiO_2$ nanomaterials manifested weak broad peaks between 20° and 30°, indicating the amorphous phases of materials. Thus, it was confirmed that all of $mSiO_2$ nanomaterials were similarly synthesized with amorphous

phases without any crystallinity. The molecular composition of various $mSiO_2$ nanomaterials were explored by the FT-IR investigation (**Figure 17**). The FT-IR spectra of all $mSiO_2$ nanomaterials displayed typical characteristic peaks of SiO_2 at 1100 cm^{-1}, around 1080–1050 cm^{-1}, and 900 cm^{-1}, which indicating the Si–O–Si asymmetric stretching, Si–O stretching vibrations, and Si–O bending, respectively [151]. Also, slight evidence of water molecules on $mSiO_2$ nanomaterials were detected at 3850–3780 cm^{-1}, 3400 cm^{-1}, and 1650 cm^{-1}, indicating the O–H stretching, –OH stretch, and H–O–H bending, respectively. In addition, carbon-related peaks originated from the CTAB surfactant were detected at 2980 cm^{-1} and 1460 cm^{-1}, which arose from the C–H stretching vibration and CH_2 scissoring mode vibration peaks, respectively. Therefore, it can be observed that slight amount of organic and water molecules were left in the $mSiO_2$ nanomaterials even after the calcination process. The reason for leftover species may attribute to the mesoporous nature of $mSiO_2$ nanomaterials bearing the numerous pores and internal voids, hindering the complete evaporation and combustion of residues. In order to gain more insight into the composition of leftover species, EDS analysis was further carried out on the $mSiO_2$ nanomaterials

(**Table 3**). Particularly, excess amounts of O (without formation of SiO_2) and C compositions were detected from the $mSiO_2$ nanomaterials. However, the amounts of atomic compositions (Si, O, and C) were similar for all $mSiO_2$ nanomaterials regardless of *L/D* and morphology of materials, implying that all samples were similarly constructed as SiO_2 material. Moreover, the electrical conductivities of $mSiO_2$ nanomaterials with *L/D* of 1, 2, and 4 were determined as 3.58×10^{-10}, 2.58×10^{-10}, and 1.59×10^{-10} S m^{-1}, respectively.

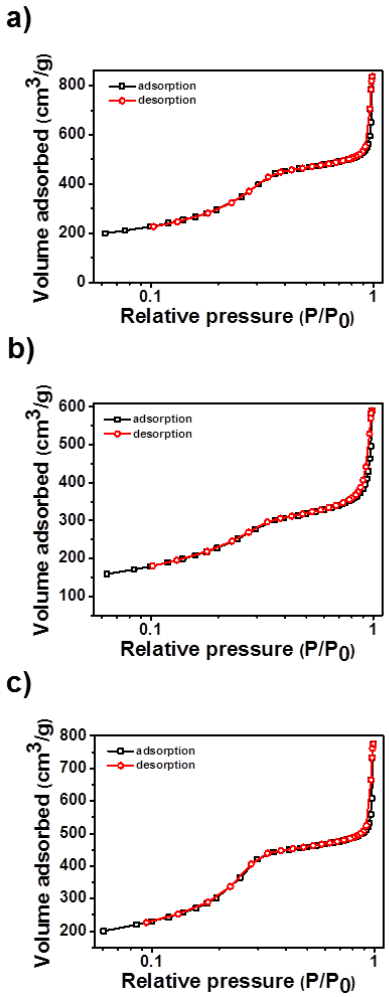

Figure 14. The N_2-sorption curves of $mSiO_2$ nanomaterials with *L/D* (a) 1 (sphere), (b) 2 (short rod), and 4 (long rod).

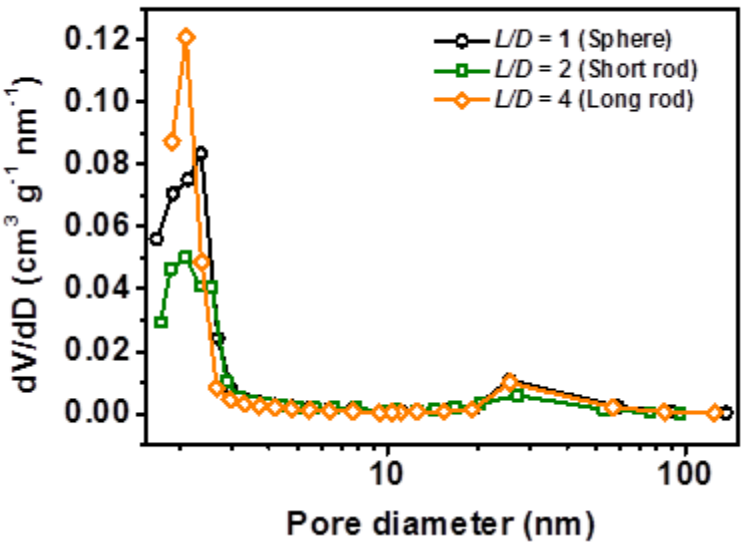

Figure 15. BJH pore distribution curves of $mSiO_2$ nanomaterials with *L/D* of 1, 2, and 4.

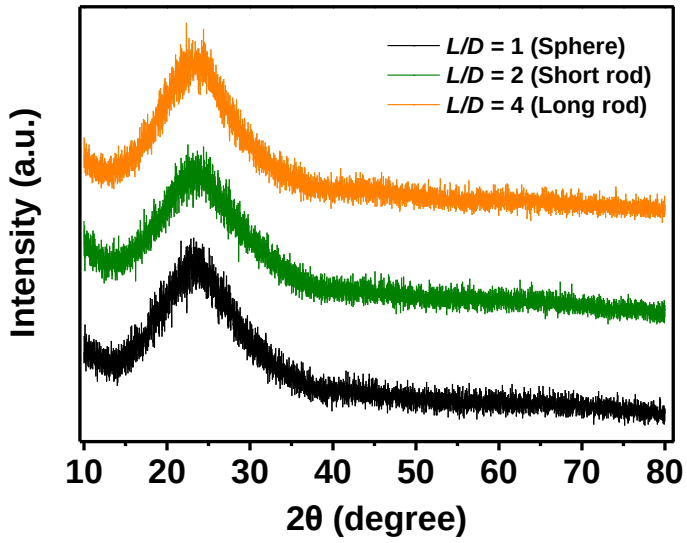

Figure 16. The XRD patterns of $mSiO_2$ nanomaterials with *L/D* of 1, 2, and 4.

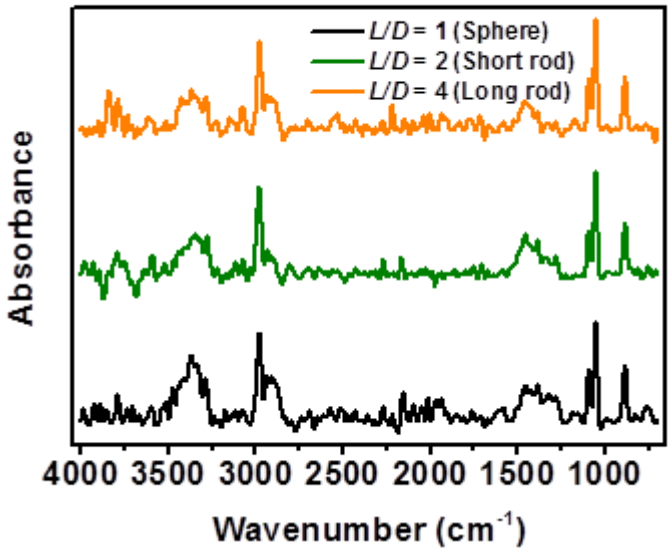

Figure 17. The FT-IR spectra of $mSiO_2$ nanomaterials with *L/D* of 1, 2, and 4.

Table 2. BET surface area and pore volume of $mSiO_2$ nanomaterials with different *L/D*.

L/D	Pore size (nm)	BET surface area ($m^2\ g^{-1}$)[a]	Pore volume ($cm^3\ g^{-1}$)[b]
1	2.1	1094.1	1.21
2	2.3	866.7	0.91
4	2.1	1176.1	1.20

[a] Calculated based on the BET method .

[b] Total pore volume of $mSiO_2$ particle.

Table 3. EDS analysis of mSiO_2 nanomaterials with different *L/*D. [a]

L/D	Si (atomic%)	O (atomic%)	C (atomic%)
1	29.31	69.47	1.22
2	28.99	69.81	1.20
4	29.32	68.88	1.80

[a] Atomic weight percent was acquired by EDS mode with 45 s, 10 μA of beam current, and 10 kV of accelerating voltage.

3.1.3. Electro-responsive activities of $mSiO_2$ nanomaterials with different *L/D*-based ER smart fluids

The ER activities of various $mSiO_2$-nanomaterials based ER smart fluids (3.0 wt%) were examined as a function of shear rate (r') under E field of 3.0 kV mm^{-1} (**Figure 18**). The leakage current of $mSiO_2$ nanomaterials-based ER smart fluid with *L/D* of 1, 2, and 4 were was 0.002, 0.003, and 0.004 mA, respectively. Low leakage currents indicated that all $mSiO_2$ nanomaterials were suitable for ER smart fluid applications; various $mSiO_2$ nanomaterials-based ER smart fluids were capable of exhibiting stable electro-responsivity under high strength of E field without an electrical short [152]. When external E field was applied, all $mSiO_2$ nanomaterials-based ER smart fluids suddenly showed shear stress curves ascribed to the formation of fibril-like structures by inter electrostatic interactions.

In the low shear rate region, the shear stress curves of all $mSiO_2$ nanomaterials-based ER smart fluids exhibited Bingham-plastic behaviors with slight fluctuations caused from the balancing between the electrostatic forces and hydrodynamic forces [153]. Slight fluctuations of shear stress curves from the typical Bingham-plastic models may originate from the mesoporous natures of $mSiO_2$

nanomaterials, which was in accordance with the ER activities of mesoporous zeolite- and MCM-41-based ER smart fluids [154]. Sudden and linear increase of shear stress curves were observed after passing the critical shear rate (r'_{crit}), illustrating the typical Newtonian behaviors. The Newtonian behaviors of ER smart fluids were originated from the domination of hydrodynamic forces over the electrostatic interactions [155]. Notably, the shear stresses of $mSiO_2$ nanomaterials increased with the increasing *L/D* in the order of 1, 2, and 4. Therefore, $mSiO_2$ nanomaterials with *L/D* of 4 exhibited the highest ER activity than other two $mSiO_2$ nanomaterials-based ER smart fluids under same experimental condition. These increment and varying ER activities of $mSiO_2$ nanomaterials may originate from the difference in *L/D* or geometrical effect, since all other factors like atomic compositions, fluid concentration, and other experimental methods were similarly set and fixed. The influence of *L/D* and related geometrical effect was further examined by measuring the ER activities of $mSiO_2$ nanomaterials-based ER smart fluid as functions of *E* field strength (fixing shear rate at 0.1 s^{-1}), as shown in **Figure 19**. The ER activities (yield stress, τ_y) of all $mSiO_2$ nanomaterials-based ER smart fluids increased by the 1.5 power of the *E* field strength

(power law relation: $\tau_y \propto E^{\alpha}$). Importantly, the ER measurement of all $mSiO_2$ nanomaterials-based ER smart fluids was stable up to *E* fields of 10.0 kV mm^{-1}, which is a very high voltage for ER smart fluids. The stability of $mSiO_2$ nanomaterials-based ER smart fluids at high voltages may originate from the high surface area of $mSiO_2$ materials. According to **Table 2**, all $mSiO_2$ nanomaterials were synthesized with large surface areas higher than 800 m^2 g^{-1}. In this regard, all $mSiO_2$ nanomaterials were constructed with high charge accumulation capabilities to withstand against the high voltages.

The real-time observations of ER activities of various $mSiO_2$ nanomaterials-based ER smart fluids were analyzed by the on-off test of applied *E* fields (**Figure 20**). By applying the *E* field (3.0 kV mm^{-1}), all ER smart fluids showed rapid increment in the shear stresses. When *E* field was turned off (0 kV mm^{-1}), the shear stresses were suddenly faded away and returned to the initial value. This real-time responsivity of ER smart fluids well suggested the characteristics of fast response and reversibility. Furthermore, practical and real-time fibril-like structure formation of $mSiO_2$ nanomaterials-based ER smart fluids were observed by the optical microscope (OM) analysis (**Figure 21**). In the initial state, all $mSiO_2$ nanomaterials were randomly

distributed in the silicone oil media without any specific structures. By applying the *E* fields, dispersed $mSiO_2$ nanomaterials rapidly constructed numerous fibril-like structures along the applied *E* field directions. It was noticeable that only few tens of milliseconds was required to construct the fibril-like structures, revealing the versatility of ER smart fluids.

More deep insight on the experimental result regarding on the increasing trends of ER activities with increments in *L/D* were considered and studied as following. In this study, the highest ER activities (shear stress) of the $mSiO_2$ nanomaterials with *L/D* of 1, 2, and 4 were determined as *ca.* 15.73, 26.25, and 47.67 Pa, respectively. It was confirmed that the $mSiO_2$ nanomaterials with higher *L/D* exerted higher ER performance compared with less dimensional $mSiO_2$ nanomaterials. According to the previous studies, higher performance of ER materials with high *L/D* can be explained in terms of the geometrical effect and dielectric properties [156,157]. Firstly, the geometrical effect can greatly affect the flow resistance and mechanical stability of ER materials in the dispersing medium [158]. With high flow resistance, materials are able to exert more steric-hindrance to withstand the mechanical shear, resulting in higher shear

stresses. The effects of flow resistance on the ER activities can be explained by following dynamic drag force (F_d) law: [159]

$$F_d = \frac{1}{2}\rho A v^2 C_d$$

From the above relation, ρ is the density of the dispersing medium, A represents the cross-sectional area of dispersed material, v is the relative velocity, and C_d is defined as the drag coefficient of the material. Particularly, the C_d value is directly depended on the geometry of material. For example, the C_d value of the sphere materials is known to be *ca*. 0.47, and this value increases with the *L/D* of materials. Accordingly, rod-like and fiber-typed materials with higher *L/D* possess larger flow resistance compared with that of sphere-shaped materials in terms of the F_d law. Furthermore, the effect of mechanical stability, which is known to be dependent according to the *L/D* of material, is another factor for varying ER performance of $mSiO_2$ nanomaterials. As shown in OM observation, $mSiO_2$ nanomaterials suddenly form fibril-like structures in the direction of the applied *E* fields. With the increments in *L/D*, longer materials form stronger fibril-like structures compared to sphere materials owing to the compactly overlapped materials and preventions of slippery, which eventually resulting in the improvement of mechanical stability and

ER activity. Moreover, changes in the *L/D* of material directly affect the dielectric properties of the material. Generally, the dielectric properties are closely related to the polarization ability of materials, which also greatly affect the ER activity [160,161]. To clarify the relations between dielectric property and ER activity, the dielectric constant (ε') and loss factor (ε'') curves of various $mSiO_2$ nanomaterials-based ER smart fluids were characterized as a function of *E* field frequency (*f*), as described in **Figure 22**.

The relation of dielectric properties and ER performance are usually explained by the achievable polarizability ($\Delta\varepsilon$) and relaxation time (λ) interpreted from the dielectric curves [162]. In general, good ER materials are known to show large $\Delta\varepsilon$ and short λ values [163,164]. The achievable polarizability (polarization tendency) is describing the magnitude of electrostatic interactions between ER materials; such term can be calculated from the differences of the static polarizability (ε_0, $f \rightarrow 0$) and fictitious polarizability (ε_∞, $f \rightarrow \infty$). The determined $\Delta\varepsilon$ values of $mSiO_2$ nanomaterials with *L/D* of 1, 2, and 4 were 0.66, 1.22, and 1.85, respectively (**Table 4**). Considering this result, increments in the *L/D* resulted in the stronger polarizability and electrostatic interactions between materials, and eventual enhancement in the ER

activity. Moreover, the polarization rate of ER smart fluids can be estimated from the relaxation time (λ), which is determined by the following equation: [165]

$$\lambda = \frac{1}{2}\pi f_{\max}$$

where f_{max} can be readily determined from the maximum peak of the ε" curve. The determined λ values of the $mSiO_2$ nanomaterials with *L/D* of 1, 2, and 4 were 0.031, 0.023, and 0.019 s, respectively. Thus, it can be concluded that $mSiO_2$ nanomaterial with *L/D* of 4 also have advantages in dielectric properties, which is denoted by the larger polarizability and faster polarization rate, compared to $mSiO_2$ nanomaterials with *L/D* of 1 and 2 as well as the geometrical effect. Previous study has explained the relations between the dielectric properties and the *L/D* of materials in terms of dipole moments. Specifically, Dukhin have examined the relation of dielectric property and *L/D* by examining the dipole moment (*p*) of various ellipsoidal particles, and following equation was set: [166]

$$p = V\varepsilon_0\varepsilon_c \frac{\varepsilon_p - \varepsilon_c}{\varepsilon_c + (\varepsilon_p - \varepsilon_c)A_z} E,$$

where ε_0 is the permittivity of the free space (8.854×10^{-12} F m^{-1}), ε_c is the permittivity of the dispersing medium, ε_p is the permittivity of

the dispersed materials, E is the electric field strength, and V is the total volume of the examined ellipsoids, described by following relation:

$$V = \frac{4}{3}\pi a^3 \frac{L}{a},$$

A_z, the depolarization factor of the employed ellipsoids, is defined as

$$A_z = (\xi^2 - 1)[\frac{\xi}{2}\ln\left(\frac{\xi+1}{\xi-1}\right) - 1],$$

where a is defined as the length of the minor axis of the ellipsoids, L is the length of the major axis of the ellipsoids, and ξ is the geometrical parameter known as the $\xi = L/\sqrt{L^2 - a^2}$. From these series of relations, it was clearly stated that the increment in L/D of material increased the dipole moment, which also lead to the enhancement of the polarization ability and dielectric property of material. Therefore, $mSiO_2$ nanomaterials with L/D of 4 exhibited the largeest $\Delta\varepsilon$ and shortest λ due to the increased magnitude of dipole moment. Conclusively, ER performances of ER smart fluids were enhanced with the increasing L/D of dispersed materials ascribed to the combined contributions of geometrical effect and improvement of dielectric properties.

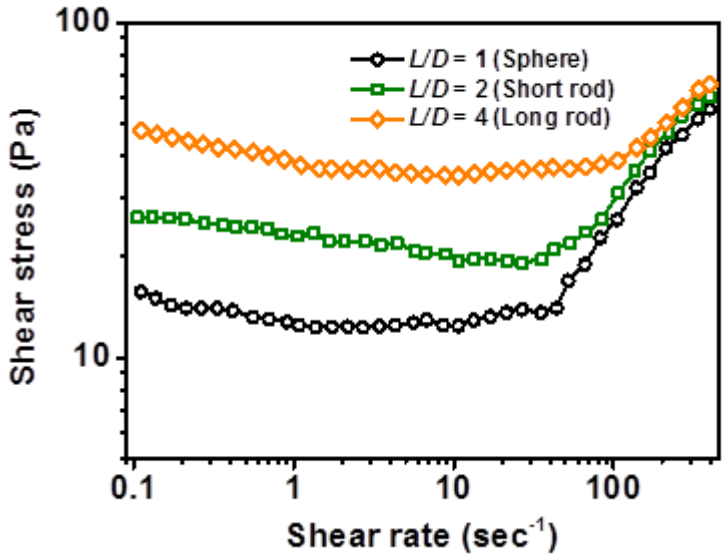

Figure 18. Shear stresses of various $mSiO_2$ nanomaterials-based ER smart fluids as a function of shear rate under 3.0 kV mm^{-1} of *E* field strength (3.0 wt% in silicone oil).

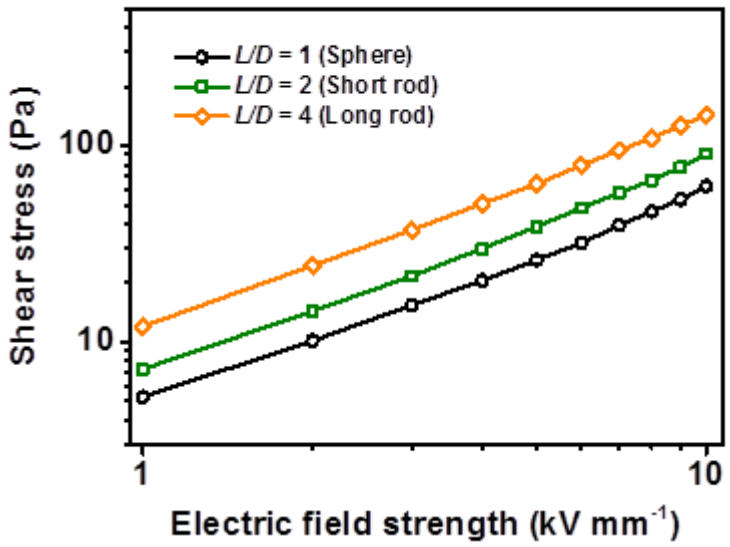

Figure 19. Shear stresses of various $mSiO_2$ nanomaterials-based ER smart fluids as a function of *E* field strength with fixed shear rate of 0.1 s^{-1}.

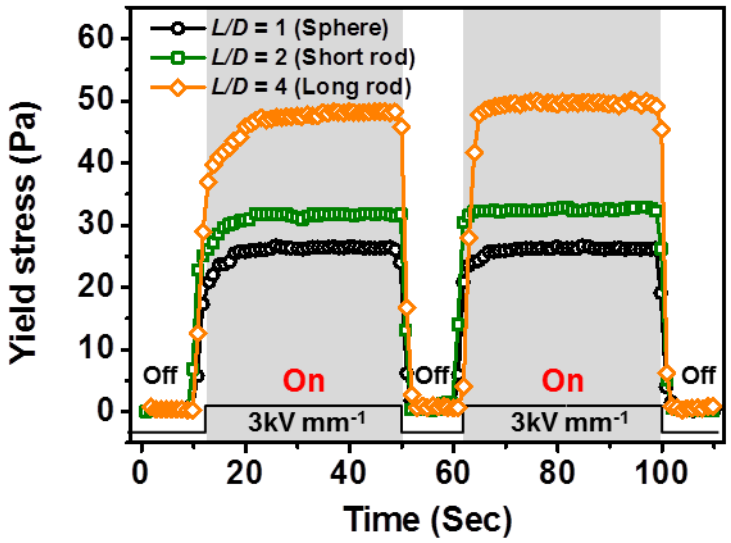

Figure 20. The *E* field on–off test of various $mSiO_2$-based smart ER fluids measured with fixed shear rate of 0.1 sec^{-1} (On state: 3.0 kV mm^{-1} and off state: 0.0 kV mm^{-1}).

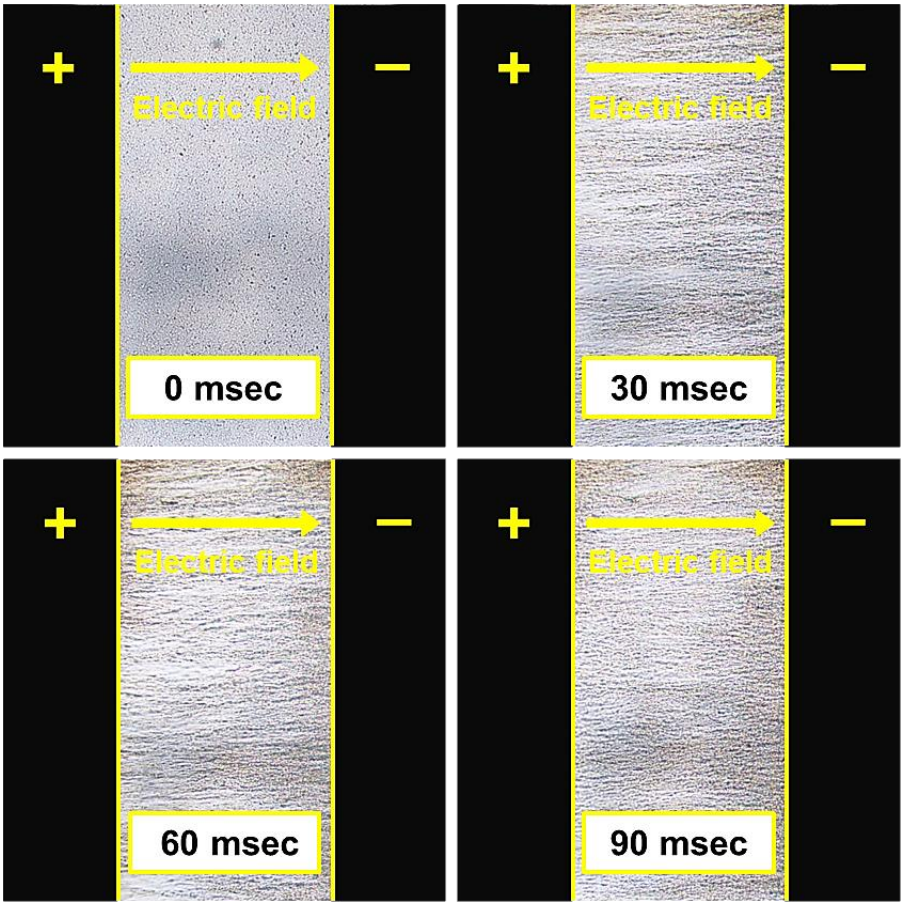

Figure 21. The real-time OM images of fibril-like structure formations of $mSiO_2$-based ER smart fluids.

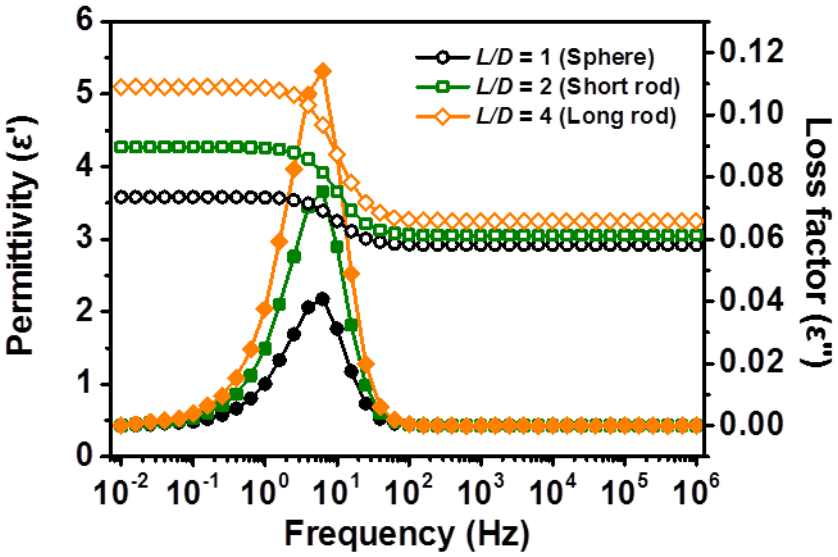

Figure 22. Permittivity (ε', open symbol) and loss factor (ε'', closed symbol) as a function of electric field frequency (f) for various $mSiO_2$ nanomaterials-based ER smart fluids.

Table 4. Dielectric parameters of various $mSiO_2$ nanomaterials-based ER smart fluids.[a]

L/D	ε_0	ε_∞	$\Delta\varepsilon = (\varepsilon_0 - \varepsilon_\infty)$	f_{max}[b] (Hz)	λ[c] (s)
1	3.58	2.92	0.66	5.31	0.031
2	4.27	3.05	1.22	6.81	0.023
4	5.1	3.25	1.85	8.31	0.019

[a] Dielectric properties were determined by impedance analyzer (1260, Solatron) coupled with dielectric interface (1296, Solatron).

[b] The local frequency of the peak from the dielectric loss factor ε'' and the f_{max} values were measured by non-linear regression using OriginPro.

[c] The relaxation time was measured using $\lambda = 1/(2\pi f_{max})$ relation (f_{max} is the maximum frequency of the loss peak).

3.2. Fabrication of $SiO_2/TiO_2@Fe_3O_4/SiO_2$ nanomaterials for EMR smart fluid application

3.2.1. Fabrication of $SiO_2/TiO_2@Fe_3O_4/SiO_2$ nanomaterial

Figure 23 represents the overall schematic illustrations of fabrication method for $SiO_2/TiO_2@Fe_3O_4/SiO_2$ nanomaterial. To synthesize the multi-layered nanomaterials responsive to *E* and *H* field with various advantages, each Fe_3O_4 nanomaterial and SiO_2/TiO_2 core/shell nanomaterials were separately synthesized at the first, and integrated using APTES silanes as linkage materials. Particularly, gram-scale quantities of Fe_3O_4 nanomaterials were prepared by the thermal decomposition of iron-oleate complex, which are synthesized from the reaction of sodium-oleate and iron chloride, in the presence of oleic acid as a surfactant. On the other hand, highly uniform SiO_2/TiO_2 core/shell nanomaterials were synthesized by sequential sol-gel methods. For the core SiO_2 template, well-known Stöber method was employed, and latter TiO_2 shell was coated as outer shells by sol-gel method using TTIP as a precursor. Accordingly, each Fe_3O_4 nanomaterial and SiO_2/TiO_2 core/shell nanomaterials were successfully prepared, and then Fe_3O_4 embedding step was followed. Prior to the Fe_3O_4 embedding process, it was essential to match the

surface polarities of two nanomaterials. Since Fe_3O_4 nanomaterials were synthesized by a thermal decomposition method and capped with the oleic acid, the surface property of resulting Fe_3O_4 nanomaterials are known to be hydrophobic owing to the surface-capped long alkane chains of oleic acid [167]. On the other hand, SiO_2/TiO_2 core/shell nanomaterials were fabricated as water-dispersible (polar) materials due to the employment of various polar solvents during the synthesis [168]. Hence, linkage materials are needed to adjust the surface polarities and increase the reactivity between two nanomaterials for successful embedding process. Among various linkage materials, APTES silane with the chemical formula of $NH_2–(CH_2)_3–Si–(OCH_3)_3$ was selected as linkage materials due to its simplicity and effectiveness of linking ability to various metal oxide and magnetic metal oxide nanomaterials including SiO_2, TiO_2, and Fe_3O_4 nanomaterials [169,170]. Notably, anchor methoxy groups of $–(OCH_3)_3$ are easily linked to the surface hydroxyl groups (–OH) of TiO_2 or SiO_2 by silylation (*i. e.* hydrolysis and condensation) reaction [171]. Moreover, it is known that methoxy groups of APTES silane are also able to replace the oleic acid molecules attached on the magnetic nanomaterials by ligand exchange [172]. Therefore, it was

expected that APTES silane would be an effective linkage molecule to connect the hydrophobic Fe_3O_4 and hydrophilic SiO_2/TiO_2 core/shell nanomaterials by aforementioned silylation and ligand exchange induced in the methoxy groups of APTES silane. In turn, numerous Fe_3O_4 nanomaterials were successfully embedded onto the SiO_2/TiO_2 core/shell materials to obtain the $SiO_2/TiO_2@Fe_3O_4$ nanomaterials. Finally, thin SiO_2 layer was introduced as the outermost shell after the embedding process by a sol-gel method, resulting in the multi-layered $SiO_2/TiO_2@Fe_3O_4/SiO_2$ nanomaterial.

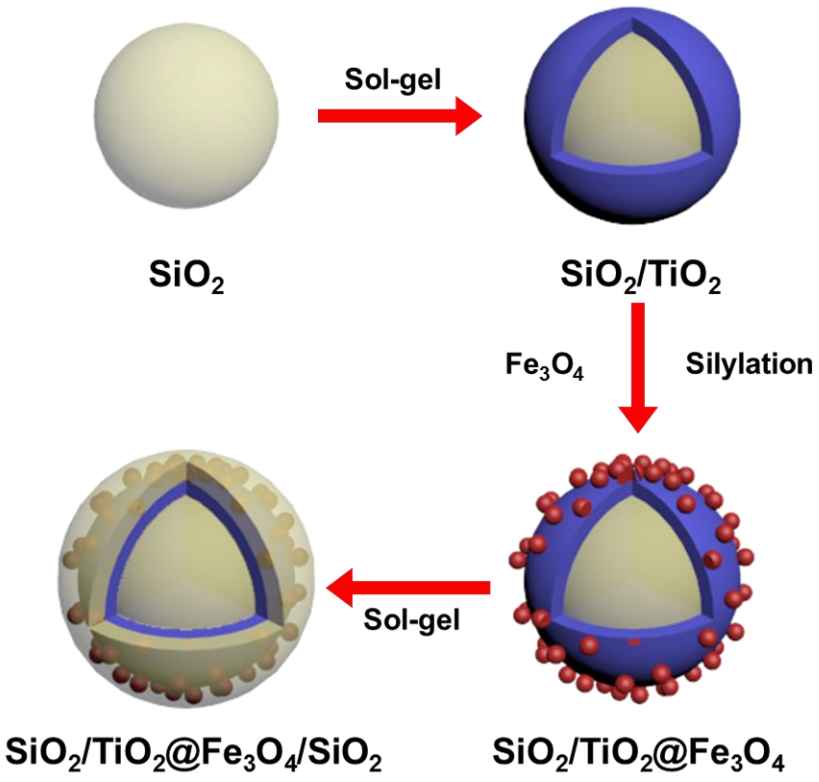

Figure 23. Schematic illustration of overall synthetic procedures of $SiO_2/TiO_2@Fe_3O_4/SiO_2$ nanomaterials.

3.2.2. Characteristic analysis of $SiO_2/TiO_2@Fe_3O_4/SiO_2$

Firstly, TEM analysis was carried out to observe the Fe_3O_4 nanomaterial, as shown in (**Figure 24**). In addition, morphologies and size of SiO_2/TiO_2 core/shell, $SiO_2/TiO_2@Fe_3O_4$, and $SiO_2/TiO_2@Fe_3O_4/SiO_2$ nanomaterials were also investigated by the TEM observation. (**Figure 25**). In case of SiO_2/TiO_2 core/shell nanomaterial, core SiO_2 was synthesized with a diameter of *ca*. 130 nm and outer TiO_2 shell was coated with the thickness of *ca*. 15 nm on each side to result in the total particle size of *ca*. 160 nm. With the sequential injection of APTES silane and Fe_3O_4 nanomaterials to SiO_2/TiO_2 core/shell nanomaterials-dispersed colloidal solution, $SiO_2/TiO_2@Fe_3O_4$ nanomaterials were synthesized as *ca*. 220 nm, indicating that silane and Fe_3O_4 nanomaterials combined layer was composed with thickness of *ca*. 60 nm. Finally, the particle size of $SiO_2/TiO_2@Fe_3O_4/SiO_2$ nanomaterial was revealed to be *ca*. 250 nm, thus outermost SiO_2 layer was coated as *ca*. 30 nm. It was confirmed that each nanomaterials were uniformly synthesized and final $SiO_2/TiO_2@Fe_3O_4/SiO_2$ nanomaterials were successfully prepared as multi-layered EMR nanomaterial.

To precisely confirm and visualize the internal compositions of as-synthesized nanomaterials, SiO_2/TiO_2 core/shell, $SiO_2/TiO_2@Fe_3O_4$, and $SiO_2/TiO_2@Fe_3O_4/SiO_2$ nanomaterials were examined by the STEM analysis, as shown in **Figure 26**. Only Si, Ti, and O elements are detected from the SiO_2/TiO_2 core/shell nanomaterial. Also, it was evident that the TiO_2 shell was well coated onto the core SiO_2 template nanomaterial. In case of $SiO_2/TiO_2@Fe_3O_4$ nanomaterial, additional Fe elements were detected throughout the outer surface of SiO_2/TiO_2, indicating the successful embedding of Fe_3O_4 nanomaterials on SiO_2/TiO_2 core/shell nanomaterials. Similarl to $SiO_2/TiO_2@Fe_3O_4$ nanomaterial, Fe, Si, Ti, and O elements were discovered from the final $SiO_2/TiO_2@Fe_3O_4/SiO_2$ nanomaterials. However, Si elements were detected as the outermost shell owing to the final coating of SiO_2 layer.

Moreover, elemental compositions of each sample were quantified by the EDS analysis, as described in **Table 5**. Similar to the STEM results, SiO_2/TiO_2 material was composed of Si, Ti, and O elements. Furthermore, it was verified that additional Fe elements were detected from $SiO_2/TiO_2@Fe_3O_4$, and $SiO_2/TiO_2@Fe_3O_4/SiO_2$ nanomaterials. However, $SiO_2/TiO_2@Fe_3O_4/SiO_2$ nanomaterials showed increased

amount of Si compositions due to the development of outermost SiO_2 shell.

The XRD patterns of nanomaterials were examined to evaluate the molecular structure, crystallinity, and magnetic phases, as shown in **Figure 27**. Particularly, the SiO_2/TiO_2 core/shell nanomaterial displayed a weak broad peak between 20 and 30°, which illustrated the amorphous phase of sol-gel formed SiO_2 and TiO_2 without any crystallinity. In case of Fe_3O_4 nanomaterials, prominent diffraction peaks were observed at 18.3, 30.1, 35.3, 36.8, 43.2, 53.3, 56.8, and 62.5°, which is assigned to the typical Fe_3O_4 (magnetite, JCPDS 75-0033) nanomaterial crystal planes of [111], [220], [311], [222], [400], [422], [511], and [440], respectively. After the embedding of Fe_3O_4 nanomaterial *via* silylation, $SiO_2/TiO_2@Fe_3O_4$ nanomaterials manifested both aforementioned characteristics of amorphous phase from the SiO_2/TiO_2 core/shell and sharp peaks of Fe_3O_4 nanomaterials. However, the intensity of the broad peak increased and slight noises were appeared on the XRD spectra of $SiO_2/TiO_2@Fe_3O_4$ nanomaterials compared to Fe_3O_4 nanomaterial owing to the formation of amorphous silane shell. Noticeably, even increased intensity of broad peak between 20 and 30° region was observed from

the final $SiO_2/TiO_2@Fe_3O_4/SiO_2$ nanomaterials owing to the additional coating of the outermost SiO_2 layer. Also, the chemical and molecular structures of samples were even closely examined by acquiring the FT-IR spectra of as-synthesized nanomaterials (**Figure 28**). Firstly, the SiO_2/TiO_2 core/shell nanomaterials showed distinguishable peaks at 1110, 1066, and 943 cm^{-1} attributed to the Si–O–Si asymmetric stretching, Si–O stretching, and Si–O–Ti bond, respectively [173]. Moreover, Fe_3O_4 nanomaterials showed strong absorption peaks related to the oleic acid, which was coated on the surface of Fe_3O_4 nanomaterial as capping molecules during the thermal decomposition. Specifically, distinguishable peaks of oleic acids were detected at 2921, 2851, 1711, and 1460 cm^{-1} due to the CH_2 asymmetric stretching, CH_2 symmetric stretching, C=O stretching vibration, and CH_2/CH_3 bending, respectively. It was clearly observed that the characteristics peaks of SiO_2/TiO_2 core/shell and Fe_3O_4 nanomaterials were detected with different intensities after each synthesis step. From the FT-IR spectrum of $SiO_2/TiO_2@Fe_3O_4$ nanomaterial, it was noticeable that the above-mentioned oleic acid-related absorption peaks were faded away after the embedding process of Fe_3O_4 nanomaterial on the SiO_2/TiO_2 nanomaterial. Such

disappearances of oleic acid-related peaks indicated the successful ligand exchange reaction took place between the oleic acid of Fe_3O_4 nanomaterial and APTES silane. Also, $SiO_2/TiO_2@Fe_3O_4$ showed absorption peaks near 1060 and 940 cm^{-1}, originating from the Si–O stretching, and Si–O–Ti bond, respectively. However, the intensities of SiO_2/TiO_2 nanomaterials-related absorption peaks were decreased after the embedding of Fe_3O_4 nanomaterial and formation of silane shell on SiO_2/TiO_2 core/shell nanomaterial. In case of $SiO_2/TiO_2@Fe_3O_4/SiO_2$ nanomaterial, the intensity of Si–O–Ti peak was significantly decreased and also oleic acid-related peaks were not detected at all. However, the peak intensity of Si–O stretching was increased, indicating the successful coating of outermost SiO_2 shells on $SiO_2/TiO_2@Fe_3O_4$ nanomaterial.

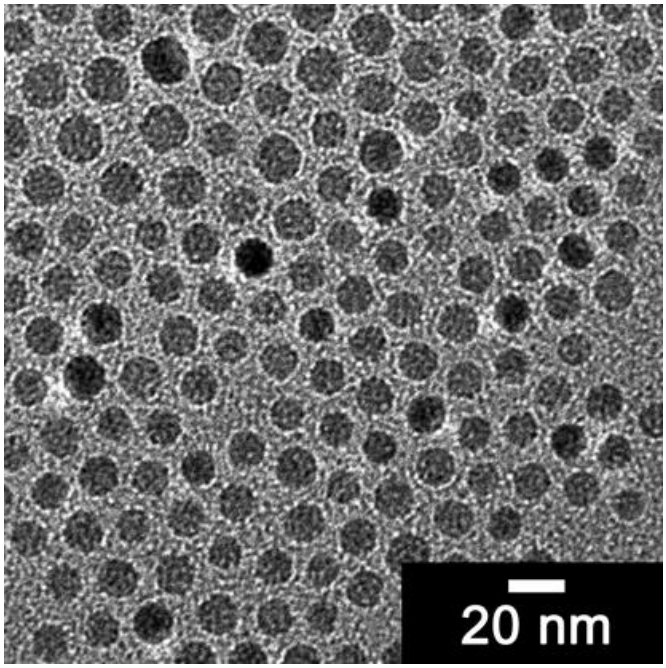

Figure 24. TEM micrograph of uniformly synthesized Fe_3O_4 nanomaterials.

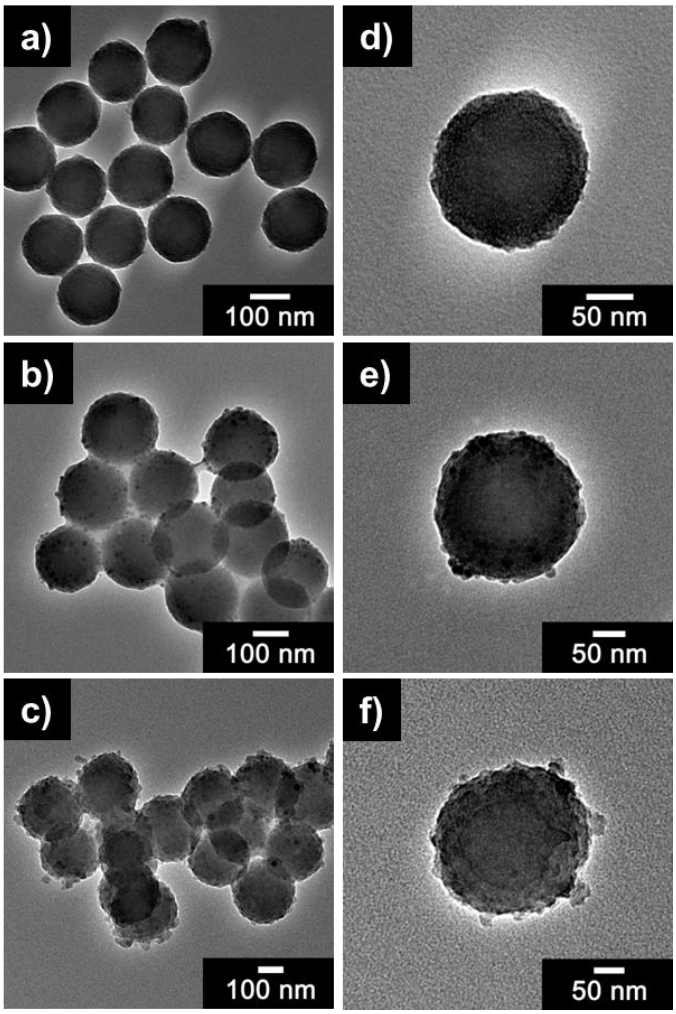

Figure 25. TEM micrograph (low magnification of (a) SiO_2/TiO_2 core/shell, (b) $SiO_2/TiO_2@Fe_3O_4$, and (c) $SiO_2/TiO_2@Fe_3O_4/SiO_2$ nanomaterials, and corresponding nanomaterials with high magnification (d, e, and f).

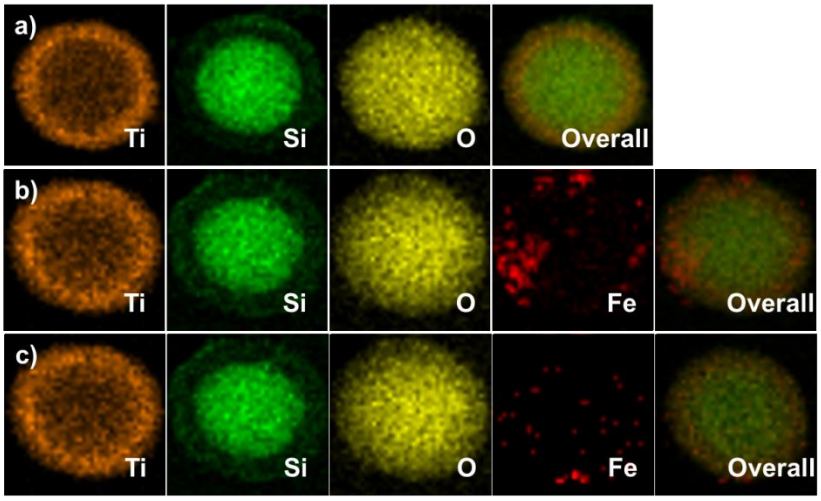

Figure 26. STEM elemental mapping images of (a) SiO_2/TiO_2 core/shell, (b) $SiO_2/TiO_2@Fe_3O_4$, and (c) $SiO_2/TiO_2@Fe_3O_4/SiO_2$ nanomaterials (detected elements: Si, Ti, O, and Fe).

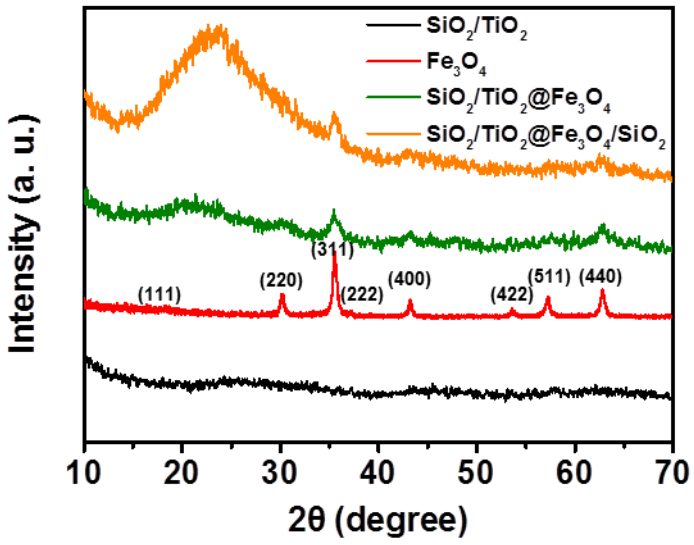

Figure 27. XRD patterns of SiO_2/TiO_2 core/shell, Fe_3O_4, $SiO_2/TiO_2@Fe_3O_4$, and $SiO_2/TiO_2@Fe_3O_4/SiO_2$ nanomaterials.

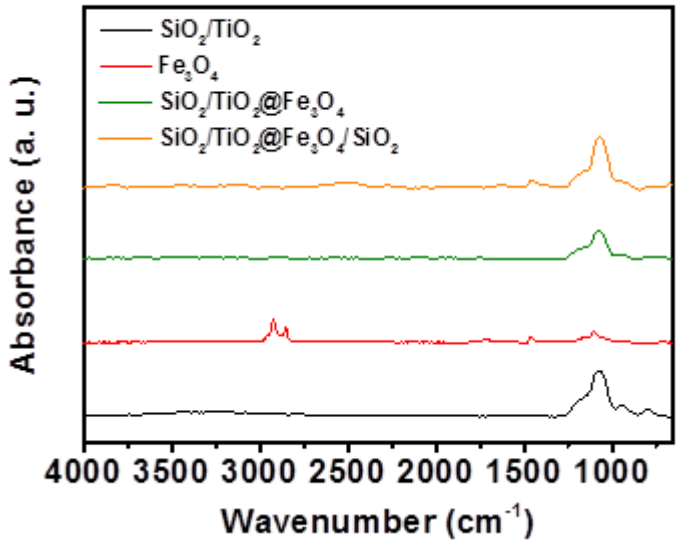

Figure 28. FT-IR spectra of SiO_2/TiO_2 core/shell, Fe_3O_4, $SiO_2/TiO_2@Fe_3O_4$, and $SiO_2/TiO_2@Fe_3O_4/SiO_2$ nanomaterials.

Table 5. Elemental compositions of Fe_3O_4, SiO_2/TiO_2 core/shell, $SiO_2/TiO_2@Fe_3O_4$, and $SiO_2/TiO_2@Fe_3O_4/SiO_2$ nanomaterials[a]

	O	Si	Ti	Fe
Fe_3O_4	51.9	-	-	48.1
SiO_2/TiO_2 core/shell	73.2	15.6	11.2	-
$SiO_2/TiO_2@Fe_3O_4$	70.7	14.6	7.5	7.2
$SiO_2/TiO_2@Fe_3O_4/SiO_2$	71.7	18.8	5.3	4.2

[a] All elements were quantified in atomic percentages. Atomic weight percent was acquired by EDS mode with 45 s, 10 μA of beam current, and 10 kV of accelerating voltage.

3.2.3. Magneto-, electro-, and electromagneto-responsive activities of $SiO_2/TiO_2@Fe_3O_4/SiO_2$ nanomaterials-based EMR smart fluid

Firstly, MR activities were measured for $SiO_2/TiO_2@Fe_3O_4/SiO_2$ nanomaterials-based EMR smart fluid. Prior to measuring the MR performance, magnetizations of Fe_3O_4, $SiO_2/TiO_2@Fe_3O_4$, and $SiO_2/TiO_2@Fe_3O_4/SiO_2$ determined as a function of *H* field strengths to overlook the magnetic properties of each nanomaterials, as shown in **Figure 29**. All nanomaterials exhibited typical hysteresis loop of the ferromagnetic materials, showing the suitability to MR smart fluid application [174]. The determined saturation magnetization from the magnetization curves for Fe_3O_4, $SiO_2/TiO_2@Fe_3O_4$, and $SiO_2/TiO_2@Fe_3O_4/SiO_2$ nanomaterials were 65.0, 46.8, and 36.5 emu g^{-1}, respectively. The saturation magnetization of nanomaterials decreased after the each sequential synthesis step, but the final multi-layered $SiO_2/TiO_2@Fe_3O_4/SiO_2$ nanomaterials showed a sufficient saturation magnetization for MR application according to the previous study [146]. The shear stresses of $SiO_2/TiO_2@Fe_3O_4/SiO_2$ nanomaterials-based EMR smart fluids were examined as a function of shear rate (r') at various applied *H* fields from 0.0 to 1.0 T with the increments of 0.2 T (**Figure 30**). With the applied *H* fields,

$SiO_2/TiO_2@Fe_3O_4/SiO_2$ nanomaterials-based EMR smart fluids showed large enhancements in shear stress compared to the initial zero-field condition (0.0 T). Such appearance of shear stresses is ascribed to the fibril-like structure formation induced by the magnetic dipole–dipole interaction of materials under applied *H* fields. Also, all shear stress curves of $SiO_2/TiO_2@Fe_3O_4/SiO_2$ nanomaterials-based EMR smart fluids showed a typical Bingham-plastic behavior, which were denoted as that the shear stress behavior independent of increasing shear rate, under various strengths of *H* fields. Accordingly, $SiO_2/TiO_2@Fe_3O_4/SiO_2$ nanomaterials-based EMR smart fluids exerted successful MR activities under applied *H* fields.

Furthermore, ER activities of $SiO_2/TiO_2@Fe_3O_4/SiO_2$ nanomaterials-based EMR smart fluid were characterized as a function of shear rate (r') under *E* field strengths 0.0 (zero-field condition) and 3.0 kV mm^{-1} (**Figure 31**). Without applied *E* field strength (0.0 kV mm^{-1}), shear stress curve of EMR smart fluid showed a typical Newtonian-like behavior, depicted by the gradual increment in the shear stress with the increasing shear rate. On the other hand, sudden appearance of the shear stress was observed with the application of external *E* field strength. In the low shear rate region, shear stress curves demonstrated

the typical Bingham-plastic behavior, and after passing the critical shear rate (r'_{crit}) shear stress proportionally increased with the increasing shear rate to show the Newtonian-like behavior. Such differences in rheological behavior were due to the balancing between the hydrodynamic and electrostatic forces generated from the mechanical shear and applied *E* fields, respectively. Thus, in the low shear rate region with low hydrodynamic force, electrostatic force dominated over hydrodynamic force to show the Bingham-plastic behavior, but at high shear rate region, hydrodynamic force overtook the electrostatic force to result in the Newtonian-like behavior. In addition, *E* field on-off test were conducted to verify the reversibility and reproducibility of ER activities of $SiO_2/TiO_2@Fe_3O_4/SiO_2$ nanomaterials-based EMR smart fluid, as shown in **Figure 32**. By applying the external *E* field of 3.0 kV mm^{-1}, EMR smart fluid showed sudden increase in the shear stress curves. By cutting off the *E* field (0.0 kV mm^{-1}), the shear stress curves reverted back to the original state. These experimental results suggested that the $SiO_2/TiO_2@Fe_3O_4/SiO_2$ nanomaterials-based EMR smart fluids displayed the successful EMR characteristics.

Finally, EMR characteristics of $SiO_2/TiO_2@Fe_3O_4/SiO_2$ nanomaterials-based EMR smart fluids were examined by the simultaneous applications of external *H* and *E* fields. Particularly, the EMR activities were conducted by applying *H* and *E* fields in parallel and perpendicular direction to observe the directional effect of the external fields on the EMR activity. Firstly, *H* and *E* fields were applied in the parallel direction, as shown in **Figure 33a**. With the applied *E* field, shear stress has increased, and further increment was discovered by applying the *H* fields. By cutting of the *E* and *H* fields step-wisely, shear stress curves also decreased in a step-wise manner. Compared to single stimulus ER activity, shear stress curves of parallel application of *H* and *E* fields manifested the increased performance, indicating the successful synergistic EMR activity contributed from both *H* and *E* fields. Moreover, *H* and *E* fields were applied to EMR smart fluids in perpendicular directions, as shown in **Figure 33b**. With the applied *E* field, EMR smart fluid showed increment in the shear stress similar to aforementioned parallel direction test. However, it was noticeable that the shear stress curves suddenly decreased after applying the *H* fields in the perpendicular direction. To gain in-depth insight into the directional effect of dual

external fields, real-time OM observation was conducted on the fibril-like structure formation of EMR smart fluids as shown in insets of **Figure 33**. It was clearly observed that the rigid and strong fibril-like structures were formed under parallel application of *H* and *E* fields. Conversely, nanomaterials showed random distribution and destructed structure under condition of perpendicular application of the external fields. To sum up, EMR smart fluid developed a high EMR activity under parallel application of dual external fields. Also, EMR activity succeeded the performance of single ER activity to illustrate the effectiveness of the dual EMR smart fluid compared to the single stimuli-responsive smart fluid.

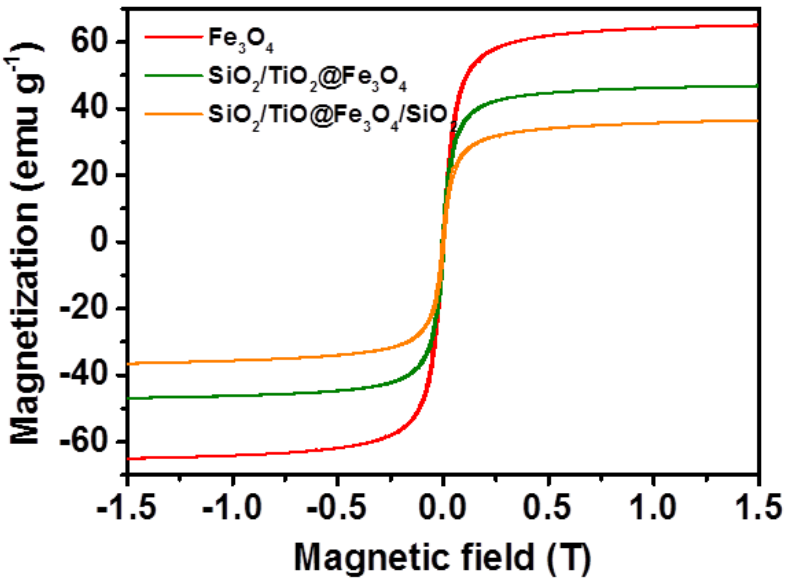

Figure 29. Hysteresis loop (magnetization versus an applied *H* field) of Fe_3O_4, $SiO_2/TiO_2@Fe_3O_4$, and $SiO_2/TiO_2@Fe_3O_4/SiO_2$ nanomaterials.

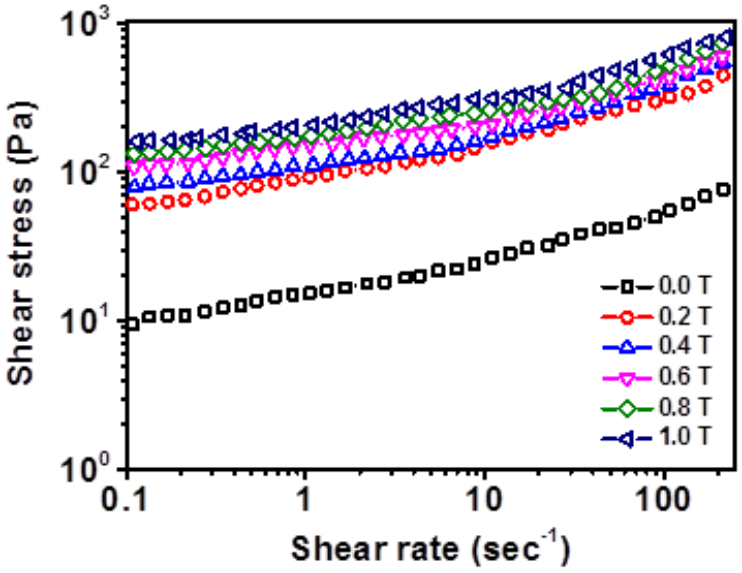

Figure 30. Shear stresses of $SiO_2/TiO_2@Fe_3O_4/SiO_2$ nanomaterials-based EMR smart fluids as a function of shear rate. The strength of applied *H* fields was varied from 0.0 to 1.0 T in increments of 0.2 T. The concentration EMR fluid smart fluid was set as 50.0 vol%.

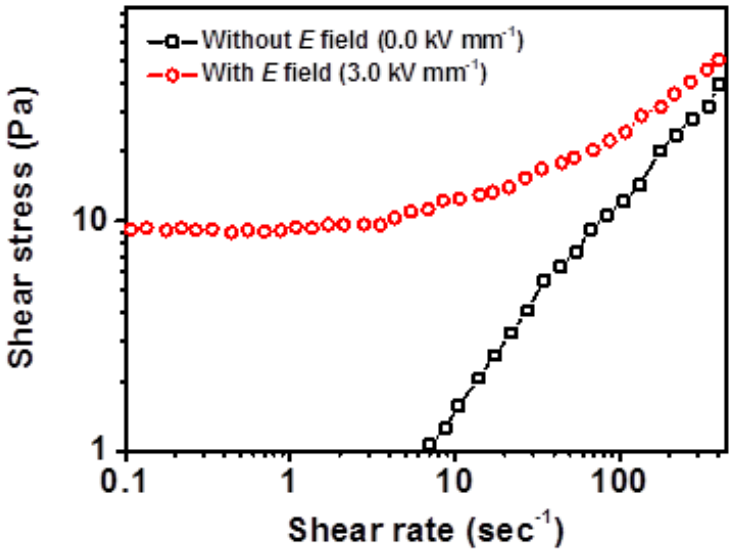

Figure 31. Shear stresses of $SiO_2/TiO_2@Fe_3O_4/SiO_2$ nanomaterials-based EMR smart fluids as a function of shear rate under zero-field (0.0 kV mm^{-1}) and *E* field (3.0 kV mm^{-1}) applied conditions. The concentration EMR fluid smart fluid was set as 20.0 vol%.

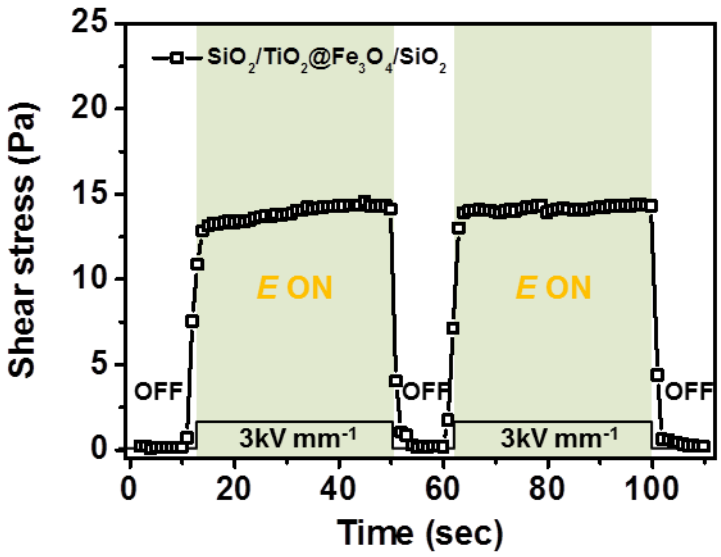

Figure 32. The *E* field on‐off test of $SiO_2/TiO_2@Fe_3O_4/SiO_2$ nanomaterials-based EMR smart fluids measured with fixed shear rate of 0.1 sec^{-1} (On state: 3.0 kV mm^{-1} and off state: 0.0 kV mm^{-1}).

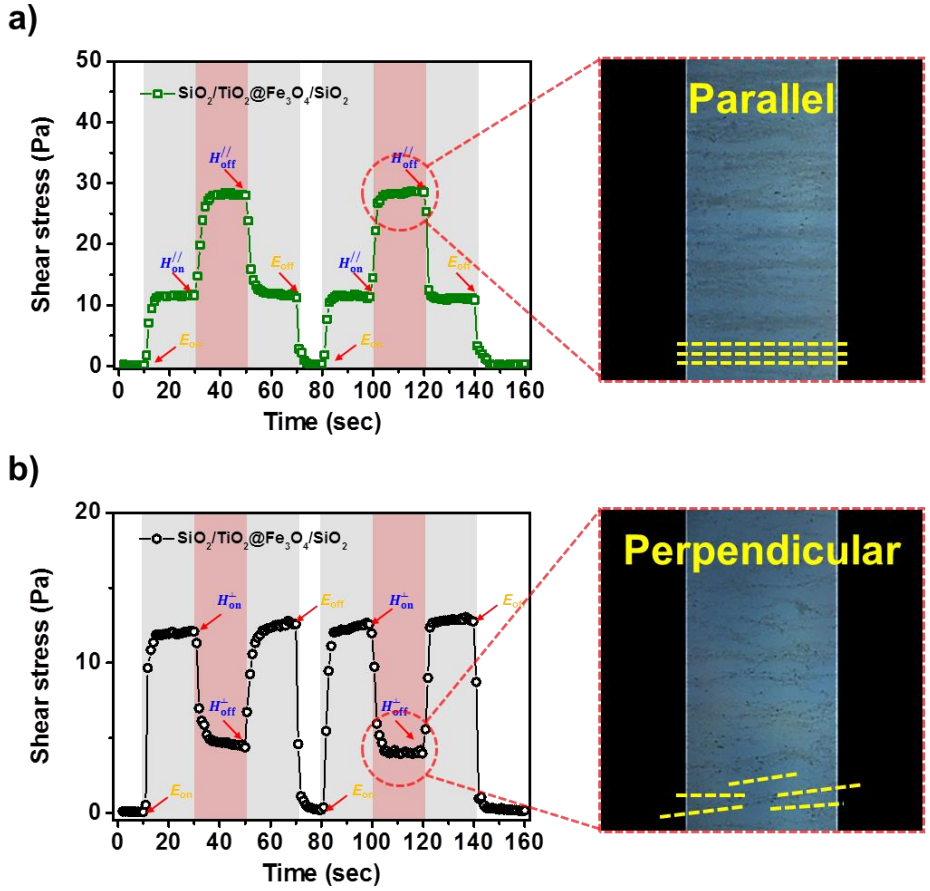

Figure 33. The on-off test of the $SiO_2/TiO_2@Fe_3O_4/SiO_2$ nanomaterials-based EMR smart fluids by switching and simultaneous applications of the *E* fields (3 kV mm_1) and *H* fields (0.2 T) at a constant shear rate of 0.1 s^{-1}. The directions of dual external field were applied in (a) perpendicular and (b) parallel directions. The boxed images placed right of the shear stress curves present the real-time OM observations of fibril-like structure formations of EMR smart fluids under perpendicular and parallel conditions. The concentration EMR fluid smart fluid was set as 20.0 vol%.

3.3. Fabrication of SP-SiO_2 nanomaterials for EPR smart fluid application

3.3.1. Fabrication and characteristic analysis of SP-SiO_2 nanomaterials

The strategy for formulation of EPR smart fluid is divided into two parts: (1) Synthesis of dispersing material for EPR smart fluid responsive to both light and *E* field and (2) Invention of dispersing medium capable of both PR and ER smart fluid applications. Overall synthesis method for fabrication of EPR material is described in **Figure 34**. Firstly, SiO_2 nanomaterial was prepared as core-template by well-known Stöber method. And then, the surface of SiO_2 nanomaterial was coated with silane shell (silylated) by dropwise addition of GPTS silane to obtain the silylated-SiO_2 nanomaterial. Finally, epoxide group on the silane shell of silylated-SiO_2 and hydroxyl group of SP–OH molecule is connected *via* ring opening reaction to attain photosensitive SP molecules decorated SP-SiO_2 nanomaterial (according to the context, SP-SiO_2 nanomaterial is also referred as EPR material in the text). The connection between SP molecule and GPTS was verified by H^1 NMR. Reaction mechanism and resulting H^1 NMR peaks of GPTS silane connected SP–OH

molecules were described in **Figure 35**. In this study, SiO_2 nanomaterial served as both ER and core template material for introduction of PR active SP molecule to prepare the SP-SiO_2 nanomaterial. It is known that SiO_2 is one of the most widely used materials in the field of the ER application owing to various advantages like suitable conductivity for ER application, mass production availability, feasible controllability for sizes, and readiness of surface treatment [175,176].

From the point of view of PR smart fluid application, final SP-SiO_2 nanomaterials act as one large photosensitive material. Mechanism for the reversible photoisomerization between SP and MC molecule on the SP-SiO_2 nanomaterial under UV (λ = 365 nm) and VIS light is shown in **Figure 36**. The resulting photoisomerized EPR material exerted different characteristics in polarity and charge-charge interaction ability due to the formation of zwitterions in MC form.

For the successful operation of EPR smart fluid system, two parameters have been controlled upon fabrication of EPR materials; size of core SiO_2 nanomaterial and thickness of silane shell. In general, the PR smart fluid is operated by the chemical interactions within the dispersed medium, thus dispersion stability must be enhanced to

prevent the degradation of PR performance by the sedimentation. To increase the dispersion stability, size of core SiO_2 nanomaterial should be reduced. For the latter, silane shell thickness must be optimized to maximize the SP loading amount to design high performance PR smart fluid. Particularly, SiO_2 nanomaterials are fabricated in three different sizes of 50, 100, and 250 nm, and dispersion stability of each material was compared by measuring the sedimentation ratio (R), as shown in **Figure 37**. After passing 60 h, 50 nm sized SiO_2 nanomaterials showed remarkable dispersion stability of 0.95, which was extremely high compared to 100 nm (R = 0.82), and 250 nm (R = 0.59) sized SiO_2 nanomaterial. Therefore, 50 nm SiO_2 nanomaterials was adopted as core template for EPR material.

Also, silane shell thickness was controlled by changing the silylation times as 1, 3, 6, 12, and 24 h (**Figure 38**). Notably, silane shell thickness of 50 nm sized silylated-SiO_2 with different silylation times were determined to be *ca*. 1, 4, 6, 10, and 19 nm for reaction time of 1, 3, 6, 12, and 24 h, respectively. Each silylated-SiO_2 are reacted with fixed amount (100 mg) of SP–OH molecule and resulting SP loading amounts of final SP-SiO_2 nanomaterials were calculated by determining the leftover SP amount in the supernatant solution using

UV-VIS spectrometer analysis (**Figure 39**) and relations described in the experimental section.

Particularly, attached amount of SP molecule increased from 58.0 mg to 66.4 mg with the increased reaction time from 1 to 24 h. However, there was no significant difference between SP loading amount of 12 h treated silylated-SiO_2 (66.6 mg) and 24 h treated silylated-SiO_2 (66.4 mg). Hence, optimized silane treatment time was determined as 12 h with SP loading amount of 66.6 mg (1.89×10^{-4} mol). Loaded SP molecule on SP-SiO_2 nanomaterials with different silylation times are listed in **Table 6**.

To investigate the morphology of as-synthesized EPR material, TEM analysis was carried out for SiO_2, silylated-SiO_2, and SP-SiO_2 nanomaterials, as shown in **Figure 40**. Highly uniform SiO_2, silylated-SiO_2, and SP-SiO_2 nanomaterials were synthesized and sizes were determined as *ca*. 50, 60, and 63 nm, respectively. It was clearly observed that the sizes of nanomaterials were gradually increased by the silane shell coating and SP decoration process. Also, SEM micrographs of each nanomaterial supported the well-defined structures of each nanomaterial (**Figure 41**). Note that, SP-SiO_2 showed slightly bumpy outer surface owing to the deposition of SP molecules in

relative to the SiO_2 and silylated-SiO_2 nanomaterials, suggesting the presence of SP molecule on the outer shell. Structural changes of each nanomaterial were further examined by BET method and BJH measurement associated with N_2-sorption curves (**Table 7**). Surface area of silylated-SiO_2 nanomaterial decreased compared to SiO_2 nanomaterial due to the increased size of material after the silylation. Notably, SP-SiO_2 nanomaterials showed further increased surface areas attributed to the successful deposition of SP molecules. Furthermore, elemental composition of SiO_2, silylated-SiO_2, and SP-SiO_2 nanomaterials were examined by STEM analysis (**Figure 42**). For SiO_2 and silylated-SiO_2 nanomaterials, only Si and O elements are detected throughout the particles. In case of SP-SiO_2 nanomaterial, additional N element was clearly observed according to the N atom presented in the indole part of SP molecule. Judging from these results, EPR material was successfully synthesized with high uniformness with the SP molecule decoration on the outer shell.

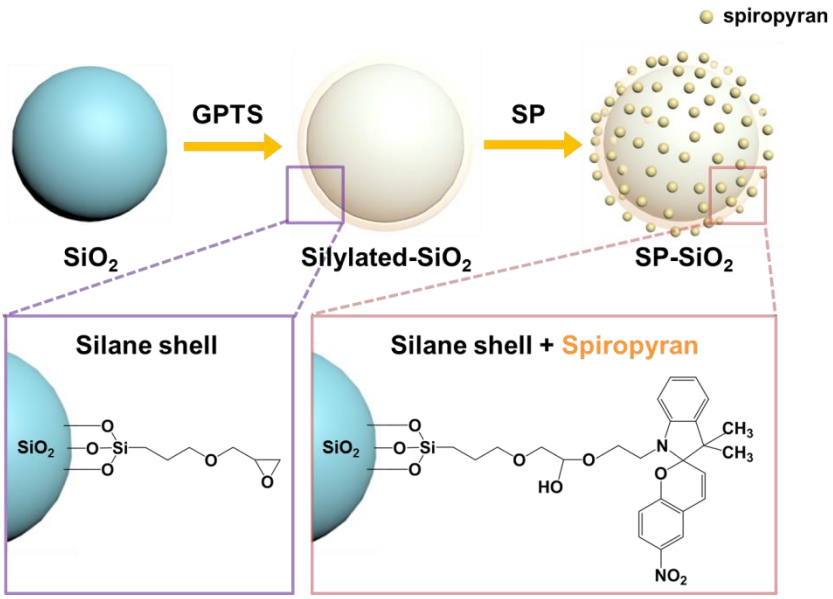

Figure 34. Schematic illustration of the synthesis method of the spiropyran-decorated silica ($SP\text{-}SiO_2$) nanomaterials.

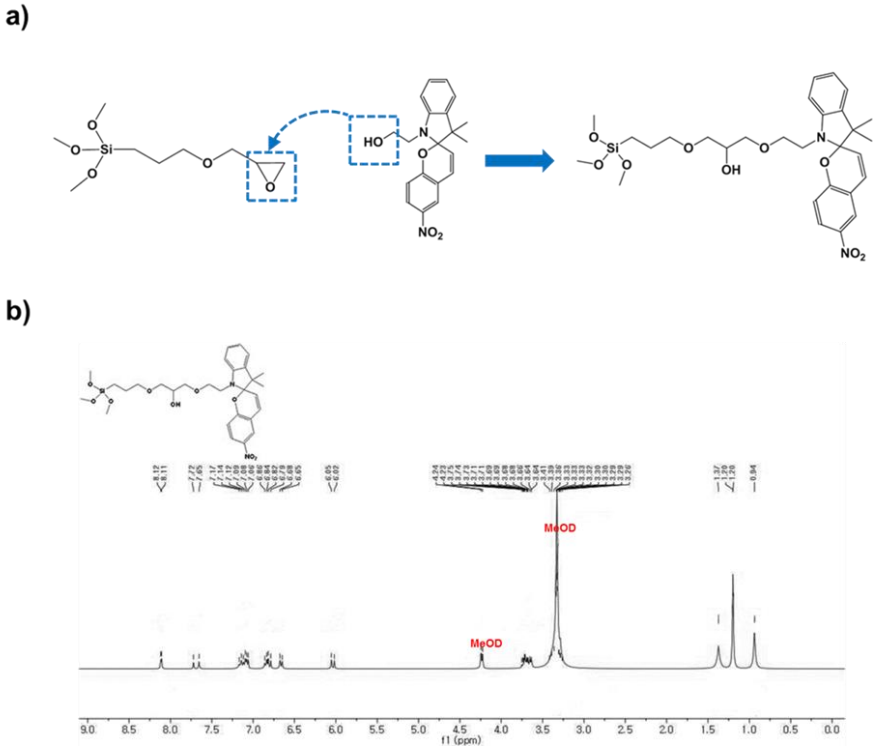

Figure 35. a) Reaction mechanism between GPTS silane and SP–OH and b) Resulting ^{1}H NMR peaks for product of GPTS and SP–OH reaction.

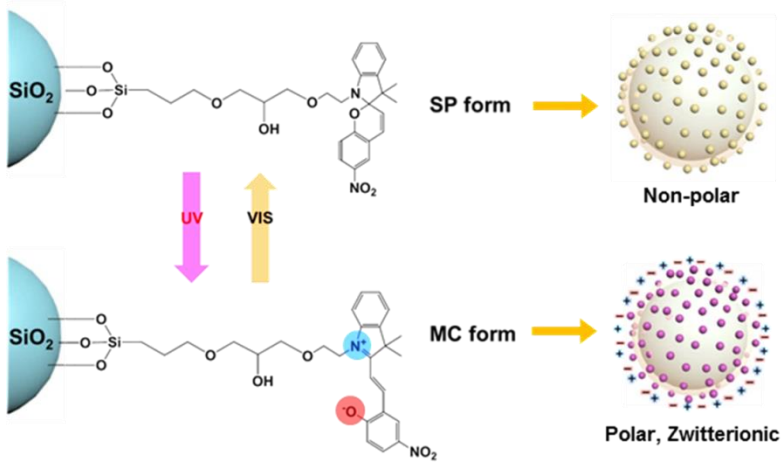

Figure 36. Schematic illustration of the reversible photoisomerization mechanism of spiropyran (SP) molecule into the merocyanine (MC) molecule on SP-SiO_2 nanomaterials under ultraviolet (UV) (λ =365 nm) and visible (VIS) light illumination.

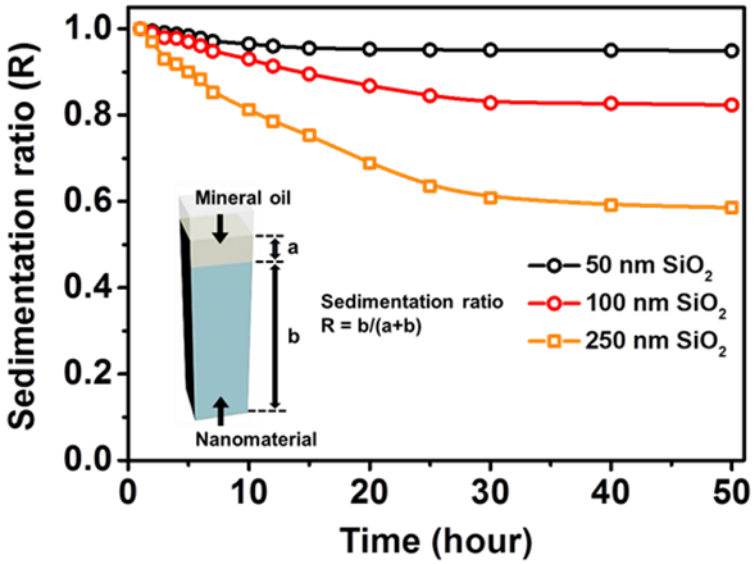

Figure 37. Dispersion stabilities of 50, 100 and 250 nm sized SiO_2 nanomaterials dispersed in mineral oil (inset: illustration and definition of sedimentation ratio).

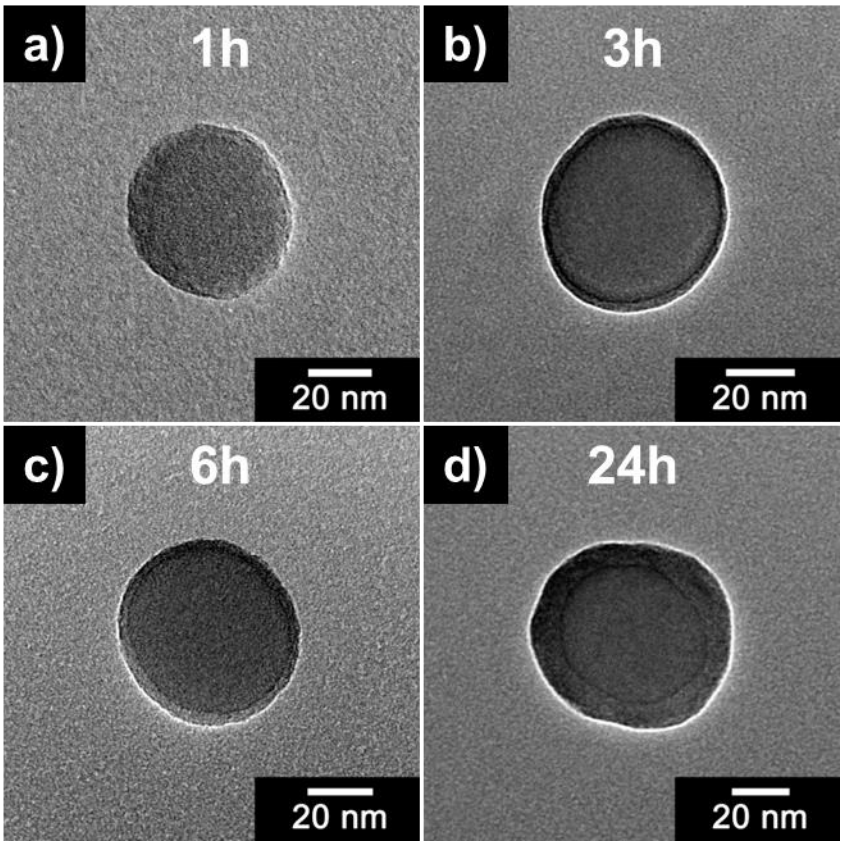

Figure 38. TEM micrographs of 50 nm sized SiO_2 nanomaterials silylated by GPTS silane in with different treatment times of a) 1h, 3h, 6h and 24 h, respectively.

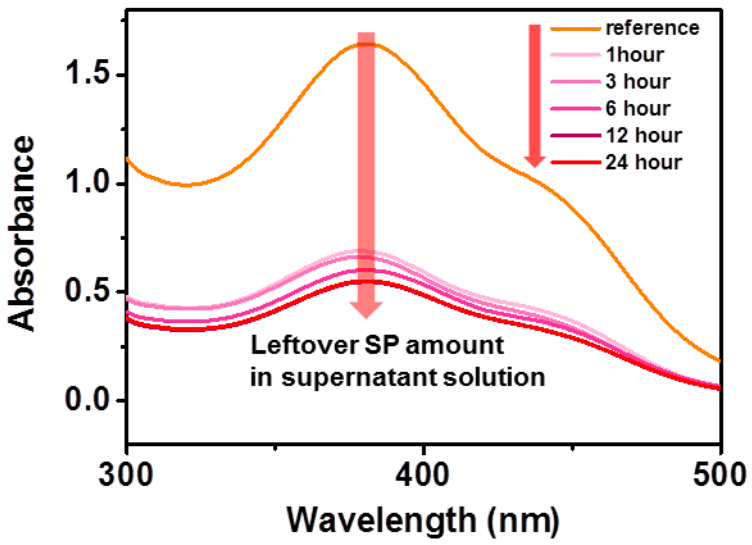

Figure 39. UV–VIS absorption spectra of leftover solutions after centrifugation of SP-SiO_2 nanomaterials fabricated in different silylation times.

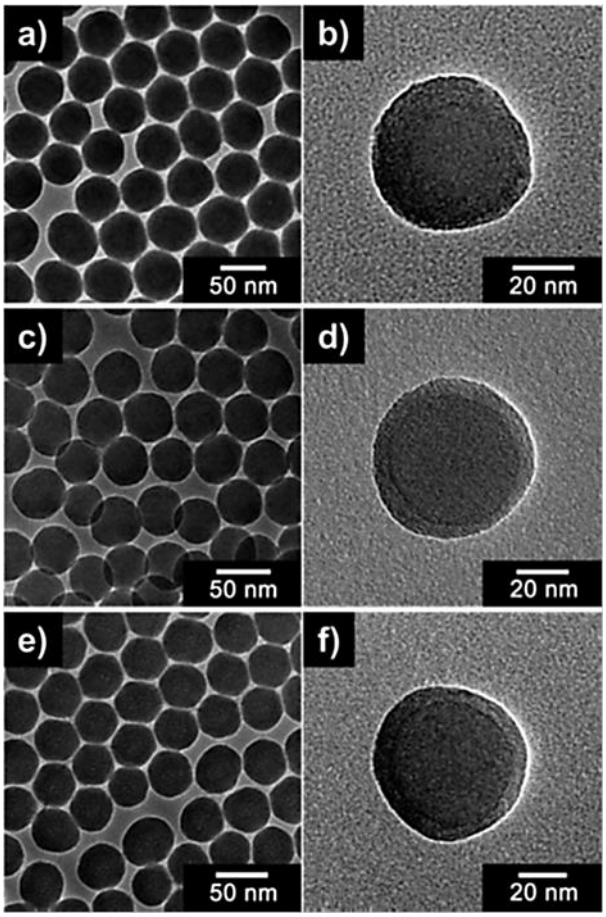

Figure 40. TEM micrographs of (a, b) SiO_2, (c, d) silylated-SiO_2, and (e, f) SP-SiO_2 nanomaterials (corresponding high magnified TEM images (b, d, and f)).

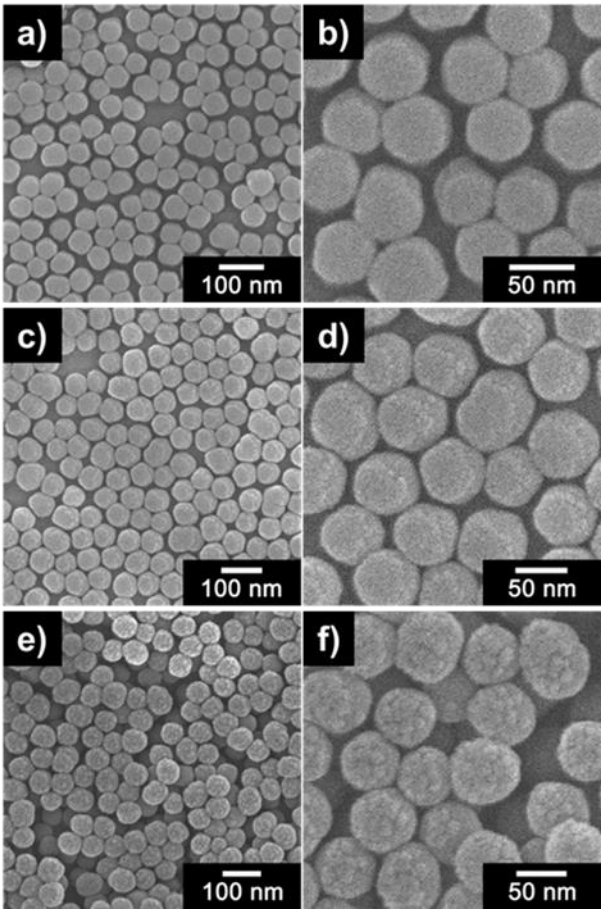

Figure 41. SEM micrographs of (a, b) SiO_2, (c, d) silylated-SiO_2, and (e, f) SP-SiO_2 nanomaterials (corresponding high magnified TEM images (b, d, and f)).

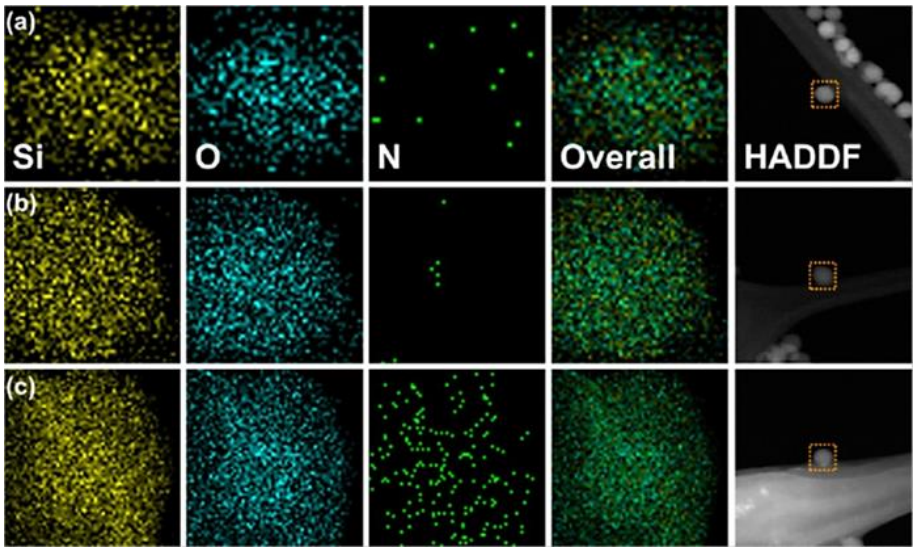

Figure 42. STEM elemental mapping images of (a) SiO_2, (b) silylated-SiO_2, and (c) SP-SiO_2 nanomaterials (detected elements: Si, O, and N).

Table 6. Attached amount of spiropyran on the 50 nm sized SP-SiO_2 nanomaterials as a function of silylation times.

Silylation time	Silane thickness[a]	Attached spiropyran (mg)[b]	Attached spiropyran (mole)[c]
1 h	*ca*. 1 nm	58.1	1.65×10^{-4}
3 h	*ca*. 4 nm	59.7	1.70×10^{-4}
6 h	*ca*. 6 nm	63.3	1.79×10^{-4}
12 h	*ca*. 10 nm	66.6	1.89×10^{-4}
24 h	*ca*. 19 nm	66.4	1.88×10^{-4}

[a] Averages of silane thickness was determined from TEM micrograph (averaging more than 50 particles).

[b] Attached amount of SP molecule was calculated by subtraction of leftover spiropyran from starting amount of SP molecule (100 mg – amount of leftover SP molecule in supernatant solution).[c] Average molecular weight of SP–OH is 352.39 g $mole^{-1}$ (information from TCI Co.)

Table 7. BET surface area and pore volume of SiO_2, silylated-SiO_2 and SP-SiO_2.

Morphology	BET surface area (m^2 g^{-1})[a]	Pore volume (cm^3 g^{-1})[b]
SiO_2	48.43	0.253 cm^3 g^{-1}
Silylated-SiO_2	35.31	0.273 cm^3 g^{-1}
SP-SiO_2	43.68	0.378 cm^3 g^{-1}

[a] Calculated by BET method.

[b] Total pore volume.

3.3.2. Formulation of dispersing medium

For the second stage of preparing EPR smart fluid, dispersing medium for EPR system must be compatible for both PR and ER smart fluid application. However, dispersing medium for PR and ER smart fluids are completely different from each other. For instance, PR smart fluid is usually prepared using organic solvent or aqueous mixture, which can afford the micelle formation, photogelation, and photoisomerization of chemicals [91]. However, dispersing mediums for ER smart fluids are limited to oils like silicone, mineral, and vegetable oil [177]. These oils have high breakdown strength to withstand the high electric voltage and contents of moisture, ions, or other additives in ER smart fluids are minimized to prevent the electric short induced by the large leakage current, which deteriorates the ER effect. Differences between PR and ER smart fluid applications were summarized in **Table 8**.

Accordingly, the task needed to be solved for this study was to invent a dispersing medium for EPR smart fluid by mixing the completely different features of two PR and ER mediums. The EPR dispersing medium was prepared by two experimental steps of a) selecting an appropriate base oil and b) addition of lecithin additives, which induced

the PR activity by the micelle formation along with the prevention of MC aggregation of EPR nanomaterials. Each steps of EPR smart fluid preparation process was verified and supported by various characteristic analyses.

To select an appropriate base oil, SP-SiO_2 nanomaterials were dissolved into widely-used silicone and mineral oil and availability for reversible photoisomerization of SP molecule was verified by subjecting to UV light (λ = 365 nm) and VIS light. In case of silicone oil, SP-SiO_2 nanomaterials containing fluid turned into purplish color by UV irradiation indicating the SP → MC transformation, but no reversible color change was observed by VIS light subjection (**Figure 43**). This non-reversible photoisomerization may have originated from the stabilization of MC molecule in the silicone oil. Specifically, polar MC molecule gained stability in the silicone oil by dipole-dipole interaction to Si and O atoms of siloxane bond, and did not converted back to the non-polar SP form *via* ring closing.

For mineral oil, EPR material also turned into reddish color, indicating the successful photoisomerization by UV light. Nevertheless, color changed EPR materials suddenly aggregated to each other and rapidly settled to the bottom (**Figure 44**). This phenomenon is referred

as MC aggregation marked by the charge-charge interaction of zwitterionic MC molecules [82]. To resolve the MC aggregation of EPR material, lecithin molecule was added to the mineral oil as an additive.

The hypothesis was set as that lecithin molecule can interact with MC molecule *via* charge-charge interaction to prevent the aggregation of EPR materials. Particularly, lecithin is a one kind of phospholipid consisted of long hydrophobic tail and zwitterionic head part. Owing to the hydrophobicity of tail part, lecithin molecule was well dissolved into hydrophobic mineral oil, but not in silicone oil having siliphilicity (**Figure 45**). Therefore, further conditions are only investigated for mineral oil, which seemed to be a more appropriate choice as base oil for the preparation of EPR smart fluid. Furthermore, effect of lecithin on mineral oil was investigated by measuring the viscosity and leakage current as a function of added amounts of lecithin molecule. Since lecithin is viscous organic molecule, overfull addition may induce the electric short of fluid to degrade the ER activity. Added amounts of lecithin to mineral oil were set to be in ratio with maximized SP loading amount (1.89×10^{-4} moles) in moles, and resulting mixtures were labelled as 0.5, 0.75, 1.0, 1.25, and 1.5 ratio mixtures. For the

viscosity examination, varying amount of lecithin did not drastically affect or change the viscosity, but slight increment was observed with the increased amount of lecithin (**Figure 46**).

However, leakage currents of lecithin + mineral oil mixtures showed large differences according to the amount of lecithin molecules under applied *E* field strength of 2.0 kV mm^{-1}. Determined leakage currents for 0.5, 0.75, 1, 1.25, and 1.5 ratio mixtures were 0.001, 0.003, 0.013, 0.025, and 1.222 mA, respectively. Leakage currents of lecithin + mineral oil mixtures increased with the added amounts of lecithin ascribed to the increasing number of zwitterions. It was noticeable that 1.5 ratio mixtures showed large leakage current with intermittent electric short inappropriate for ER activity. Considering these result, added amount of lecithin additive was set in ratio of 1.25:1.0 for lecithin to SP molecules for preparation of EPR smart fluids.

Additionally, photo-reversibility and dispersion stability of as-prepared EPR smart fluid was examined. Importantly, EPR smart fluid manifested reversible color change to indicate the successful photoisomerization between SP and MC (**Figure 47**). Moreover, UV subjected EPR smart fluid showed ultra-dispersibility without any aggregation or sedimentation of EPR material, which implied that

lecithin have played pivotal role for preventing the MC aggregation as intended (**Figure 48**). Specifically, zwitterionic head of lecithin molecules formed charge-charge interaction with MC molecule, preventing the self-aggregation of EPR materials. With the VIS light application, MC form reverts back to non-ionic SP form and EPR material is released from the lecithin. These binding and releasing operation of EPR material and lecithin not just prevented the MC aggregation, but also produced the PR activity, which will be discussed in the later section.

To further clarify the successful formation of EPR smart fluid, UV–VIS spectra were examined to investigate the light induced effect (**Figure 49**). Particularly, EPR smart fluid was exposed to UV light (λ = 365 nm) and absorption spectra was recorded in interval of 1 min. Without UV irradiation in the beginning, EPR smart fluid showed almost no absorption peak in the presented range of wavelength. By applying the UV light, a strong absorption peak appeared at wavelength of 540 nm, indicating the SP → MC isomerization of EPR material [178]. Noticeably, there was no further absorbance change in the spectrum after passing 3 min of UV irradiation, which indicated that UV conversion is completed within 3 min. Moreover, absorption peak

at wavelength of 540 nm greatly decreased after applying VIS light for 3 min, suggesting the successful MC → SP reversible isomerization. Considering these results, reversible photoisomerization of EPR material is completed within 3 min, and PR activity may induce in this time interval. Consequently, EPR smart fluid was successfully prepared by facilitation of various parameter control experiments on template size (50 nm SiO_2), silylation time (12 h), medium selection (mineral oil), and additives (lecithin).

Figure 43. Digital photographs of the SP-SiO_2 nanomaterials dispersed in silicone oil after treatment with UV (λ = 365 nm) and VIS light. (Silicone oil. Left: blank oil; middle: containing SP-SiO_2 nanomaterials; right: containing SP-SiO_2 nanomaterials + lecithin).

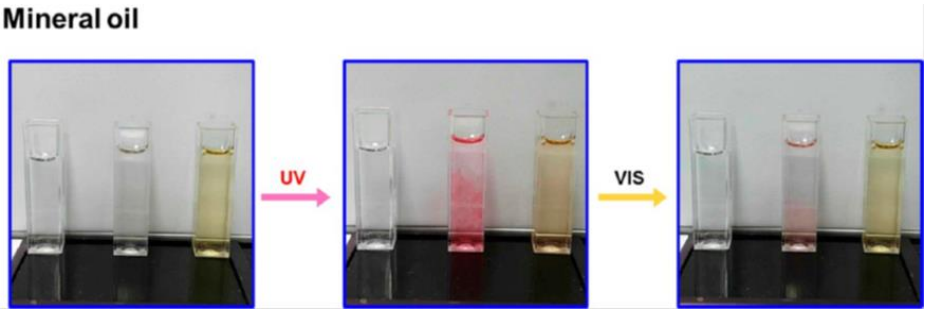

Figure 44. Digital photographs of the SP-SiO_2 nanomaterials dispersed in mineral oil after treatment with UV (λ = 365 nm) and VIS light. (Mineral oil. Left: blank oil; middle: containing SP-SiO_2 nanomaterials; right: containing SP-SiO_2 nanomaterials + lecithin).

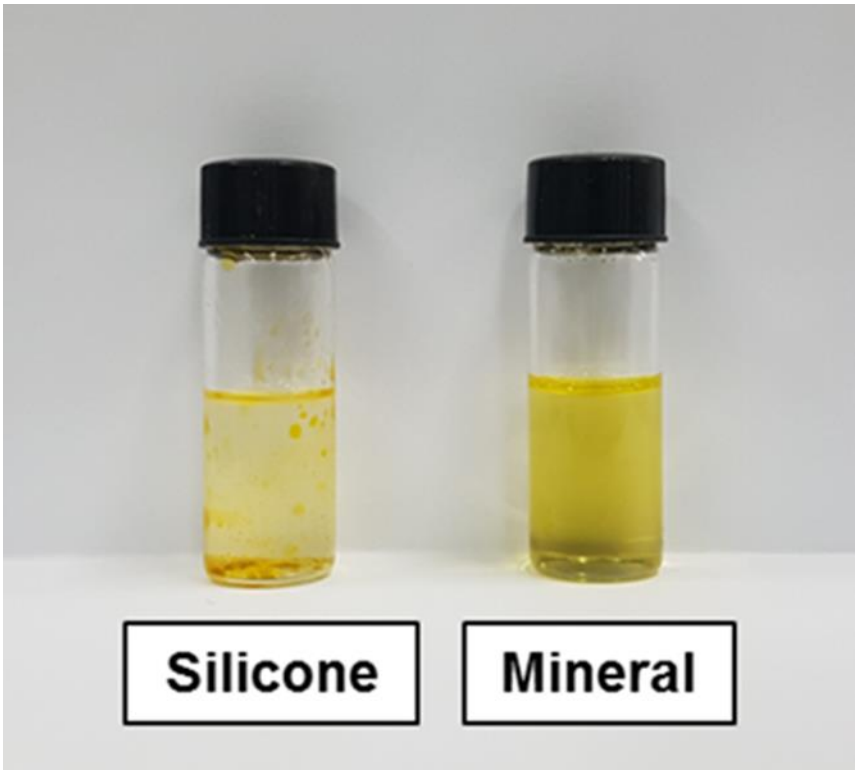

Figure 45. Digital photographs of lecithin added silicone (left) and mineral (right) oil.

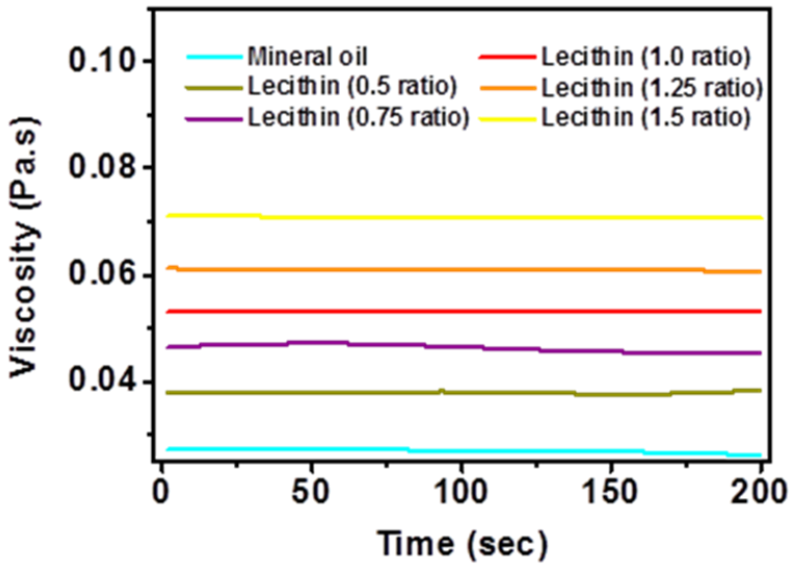

Figure 46. Viscosities of mineral oil mixed with various amounts of lecithin molecules with fixed shear rate of 0.1 s^{-1}.

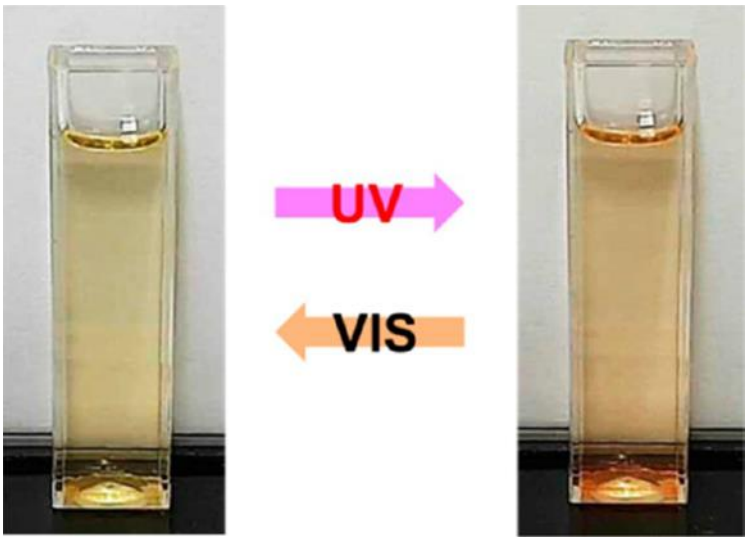

Figure 47. Reversible color change of the EPR smart fluid composed of SP-SiO_2 nanomaterials, lecithin, and mineral oil under UV and VIS light illumination. No sedimentation was occurred in the EPR smart fluid after subjection to lights.

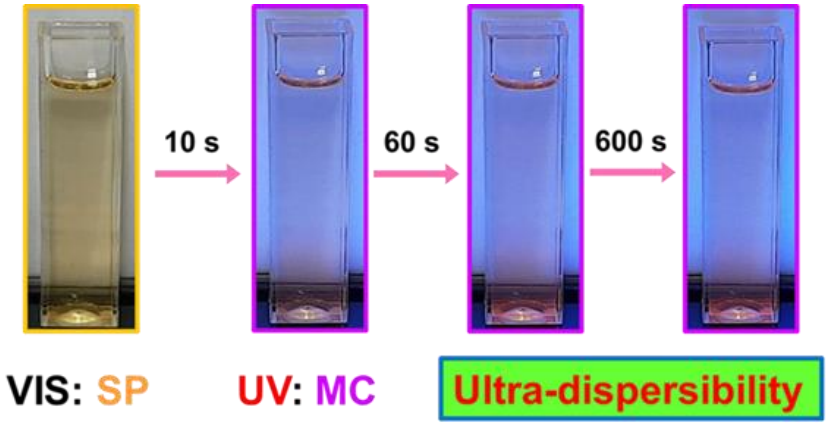

Figure 48. Ultra-dispersibility of UV-irradiated EPR smart fluid without any inducement of MC aggregations.

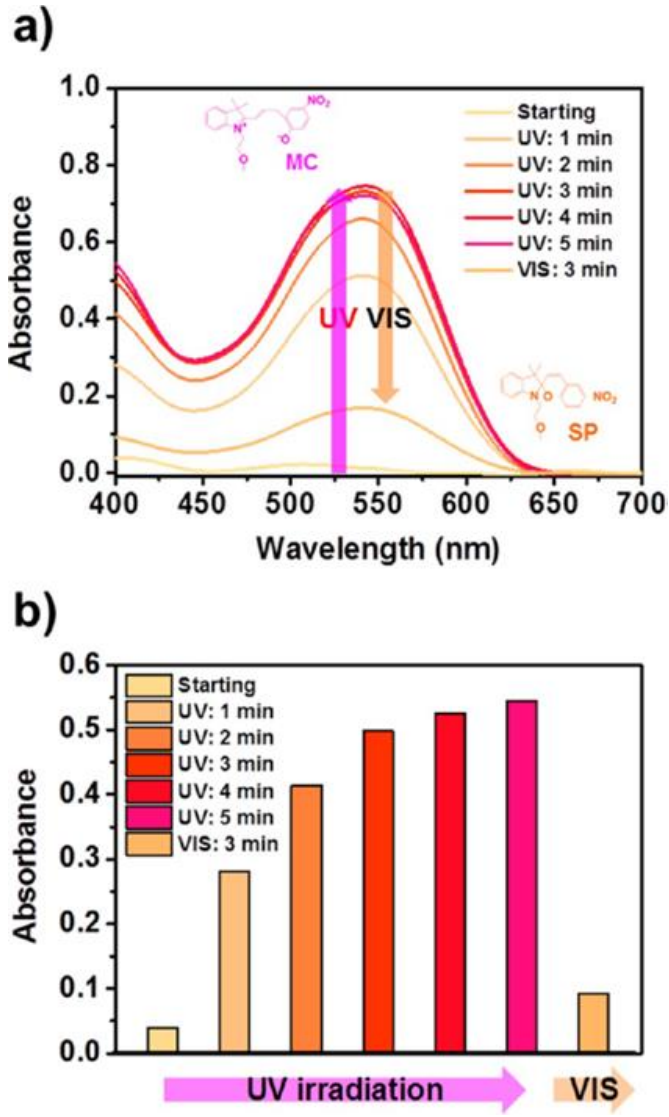

Figure 49. (a) The UV－VIS spectra of EPR smart fluids under UV (λ = 365 nm) and VIS light irradiation. (b) Corresponding absorbance changes of the UV－VIS spectra.

Table 8. Comparisons between ER and PR smart fluids.

	Electrorheological (ER) fluid	Photorheological (PR) fluid
External stimuli	Electric field (up to 5.0 kV mm^{-1})	UV or VIS light
Dispersing medium	Oils like silicone, mineral, vegetable, and *etc*.	Organic solvent (polar or nonpolar)
Dispersant	Polarizable particle (nano to micro-sized)	Photosensitive molecule, additives, gelator and *etc*.
Phase	Two (colloid + oil)	One (molecules dissolved in solvent)
Conductivity	Low (best near 10^{-7} S cm^{-1})	Depending on the compositions

3.3.3. Photo-, electro-, and electrophoto-responsive activities of SP-SiO_2 nanomaterials-based EPR smart fluid

Prior to measuring the rheological activity of as-formulated EPR smart fluid, dielectric properties of SP-SiO_2 nanomaterial were compared to SiO_2 and silylated-SiO_2 nanomaterials to overlook the potentiality of SP-SiO_2 as an ER material. According to the previous studies, dielectric property of material is closely related to the polarizability, which directly affects the ER activity [179]. **Figure 50** represents the dielectric constant (ε') and dielectric loss factor (ε'') of SiO_2, silylated-SiO_2, and SP-SiO_2 nanomaterials dispersed in the mineral oil (normal ER smart fluid) as a function of electric field frequency (f). In general, good ER activity is characterized by a large achievable polarizability ($\Delta\varepsilon$) and small relaxation time (λ). Former is related to the polarization tendency of materials and latter is ascribed to the polarization rate of materials [180]. The achievable polarizability is determined from the difference between static polarizability (ε_0, where $f \rightarrow 0$) and fictitious polarizability (ε_∞, where $f \rightarrow \infty$) of the dielectric constant curve [181]. The determined $\Delta\varepsilon$ of SiO_2, silylated-SiO_2, and SP-SiO_2 nanomaterials-based ER smart fluids were 0.37, 0.46, and 0.81, respectively. Relatively large $\Delta\varepsilon$ of SP-SiO_2 nanomaterials inferred that

it has larger polarization tendency compared to SiO_2 and silylated-SiO_2 nanomaterials attributed to the presence of organic SP molecule, which has highly polarizable conjugated π bond in the structure. Fortunately, SP molecule depositions have assigned photo-responsiveness as well as the high dielectric property to the SP-SiO_2 nanomaterial. Moreover, relaxation time of each material was assessed by the following equation: [165]

$$\lambda = \frac{1}{2\pi f_{max}}$$

where f_{max} is referred to maximum electric field frequency of dielectric loss factor curve. Calculated λ of SiO_2, silylated-SiO_2, and SP-SiO_2 nanomaterials were 0.048, 0.043, and 0.039 s, respectively. Therefore, SP-SiO_2 nanomaterial can polarize relatively faster compared to SiO_2 and silylated-SiO_2 nanomaterial. Moreover, dielectric properties of lecithin added EPR smart fluid was investigated to gain deeper insight into the effect of lecithin on polarization and ER activity (**Figure 51**). For the clear observation of lecithin effect, lecithin-mineral oil mixture without EPR material was prepared as well as the EPR smart fluid. It was noticeable that the lecithin-mineral oil mixture manifested extremely large $\Delta\varepsilon$ of 16.66 ascribed to the large polarizability of lecithin with polarizable groups like carbonyl and

amine, which was completely higher than prepared ER smart fluids without lecithin. Moreover, EPR smart fluid showed even increased $\Delta\varepsilon$ of 23.2 due to the combined dielectric increasing effect induced by the SP and lecithin molecules. As a result, prepared EPR smart fluid may have a good potentiality for ER smart fluid application due to the large dielectric property and resulting enhanced polarizability. Detailed dielectric properties of EPR smart fluid, lecithin + mineral oil, and 3 ER smart fluids are listed in **Table 9**.

Practical ER activities of EPR smart fluid and three ER smart fluids composed of only nanomaterials and mineral oil without lecithin were measured as a function of shear rate (τ') under E field strength of 2.0 kV mm^{-1} (**Figure 52**). With the applied E field, EPR and ER smart fluids exhibited the shear stress curves generated by the formation of fibril-like chains within the fluids. Bingham-plastic behavior of plateau curves were observed for all samples in the low shear rate region due to the balancing between the electrostatic static force of arranged particles and hydrodynamic force from the mechanical shear. After passing the critical shear rate (τ_{crit}), all samples showed Newtonian behavior denoted by the proportional increment of shear stress to shear rate. Among ER smart fluids without lecithin, SP-SiO_2-based ER smart

fluids manifested the highest ER performance attributed to the enhanced dielectric property from SP molecule. Determined ER performance of SiO_2-, silylated-SiO_2-, SP-SiO_2-based ER smart fluids, and EPR smart fluids were *ca*. 7.7, 9.4, 14.1, and 57.5 Pa, respectively. Remarkably, EPR smart fluids manifested 4-fold enhanced ER activity compared to SP-SiO_2-based ER smart fluids without lecithin molecule. Considering these results, EPR smart fluids are well-designed to present the superb ER performance owing to the combined enhancement of dielectric properties contributed from the SP and lecithin organic molecules. To investigate the effect of photoisomerization of SP molecule on ER activity, EPR smart fluids were exposed to UV and VIS light for 3 min and shear stress curves were measured under *E* field strength of 2.0 kV mm^{-1}, as shown in **Figure 53**. Noticeably, UV induced EPR smart fluid displayed shear stress of *ca*. 115.3 Pa, which was 2- and 8-fold higher value compared to the VIS light applied EPR smart fluid and SP-SiO_2-based ER smart fluid. These results suggested that the interactions of zwitterionic MC and lecithin molecules (UV induced effect) had impact on the ER activity of EPR smart fluid. Also, three times repeated ER smart fluid application results of UV–VIS subjected EPR smart fluid were

similarly determined, suggesting the stability and non-degradation of EPR materials by external stimuli.

Furthermore, stability of EPR smart fluid against *E* field strength was even closely evaluated by varying the *E* field strength and cyclic on-off test. Spcifically, ER performance of EPR smart fluids exposed to VIS and UV light for 3 min were measured as a function of *E* field strength, as described in **Figure 54**. The applied *E* field strengths were increased up to 2.0 kV mm^{-1} by the increment of 0.5 kV mm^{-1}. The yield stress of EPR smart fluids were stably and linearly increased by 1.5 powers of *E* field strengths up to 2.0 kV mm^{-1}. However, EPR smart fluid could not withstand the *E* field above 2.0 kV mm^{-1} owing to the electric shorts caused by the zwitterions of lecithin molecules. In addition, *E* field cyclic on-off test was conducted on the EPR smart fluids (**Figure 55**). With the applied *E* field, EPR smart fluids manifested immediate shear stresses and faded away by cutting off the *E* field. This alternation of *E* field on-off process was repeated for five times and EPR smart fluids exhibited similar values of shear stresses during the cycles, indicating the reversibility of the fluid. Therefore, EPR smart fluids were composed with sufficient stability and reversibility without degradation of composing materials under high *E* field strength and

exposing to light sources.

In order to achieve an in-depth insight into the effect of UV–VIS light on EPR system, PR activity and EPR activity were examined by simultaneous application of external stimuli. **Figure 56** shows the rheological change of EPR smart fluid under various conditions of stimuli applications. Conditions for different stimuli applications are divided in the time interval of 300 s as following: a) No stimuli for 0 to 100 s, b) VIS light for 100 to 400 s, c) UV irradiation 400 to 700 s, d) VIS light + *E* field for 700 to 1000 s, and e) UV light + *E* field 1000 to 1300 s. Specifically, PR activities of EPR smart fluid are examined in the time range of 100 to 700 s, where only UV and VIS lights are applied, and EPR activities were investigated by the simultaneous application of light and *E* field (2.0 kV mm^{-1}) in the time interval of 700 to 1300 s. PR performance of EPR smart fluid is closely examined by magnifying the range of 100 to 700 s, as shown in **Figure 57**. Under UV irradiation, shear stress of EPR smart fluid gradually increased up to *ca*. 0.8 Pa (400 s). With the VIS light application, shear stress curve steadily decreased to the original state *ca*. 0.45 Pa. This increasing and decreasing shear stress behavior under UV and VIS light clearly presented the reversible PR activities of EPR smart fluid.

The mechanism for the PR activity induced in the EPR smart fluid is proposed as follows. When EPR material is in MC form, head part of lecithin molecules binds to the surface of EPR material to form micellar structure, and hydrophobic tail part of lecithin molecules binds to hydrophobic mineral oil, resulting in ordered (or well-distributed) assemblies of lecithin and EPR material micelle with high stability, producing an increased shear stress. In case of EPR material in SP form, non-polar EPR materials may draw each other owing to the intermolecular force, resulting in a non-homogeneous distribution and relatively aggregated state. In this regard, EPR material in MC form exhibited higher PR activity due to stabilization and well-arranged state arose from the sequential binding of EPR material, lecithin, and mineral oil compared to SP phased EPR material.

Returning to the **Figure 56**, EPR performances were assessed in interval between 700 to 1300 s. Under the dual stimuli of VIS light and electric field, EPR smart fluid exhibited greatly increased shear stress of *ca*. 57.5 Pa compared to PR only-active region due to the inherently high performance of ER activity. Notably, EPR smart fluid manifested the highest shear stress of *ca*. 115.3 Pa under simultaneous application of UV irradiation and *E* field strength. To further clarify the drastic

enhancement of EPR performance under UV + *E* field, real-time OM observation was carried out for two different conditions. For VIS + *E* field, EPR materials formed partially disconnected or weak fibril-like structures. On the contrary, EPR materials showed numerous formations of fully-connected fibril-like structures for UV + *E* field application. Tentative mechanisms for enhanced EPR activity of EPR smart fluid under UV irradiation and *E* field strength and resulting fibril-like structure formations observed by OM analysis are illustrated in **Figure 58**. In particular, EPR materials are well-distributed throughout the dispersing medium, and in this condition more rigid and fully-connected fibril-like structure can be created with the *E* field application compared to non-homogeneously distributed VIS induced EPR smart fluid. Judging from these experimental results, binding mechanism of SP-SiO_2 nanomaterials, lecithin, and mineral oil not just provided the PR activity, but successfully contributed to the high EPR activity under dual application of UV light and *E* field. In short, the ER, PR, and EPR activities of EPR smart fluid under various conditions of external stimuli were summarized in **Table 10**. Consequently, this newly-designed EPR smart fluid successfully illustrated the ER, PR, and combined EPR activity depending on the sources and combination

of external stimuli.

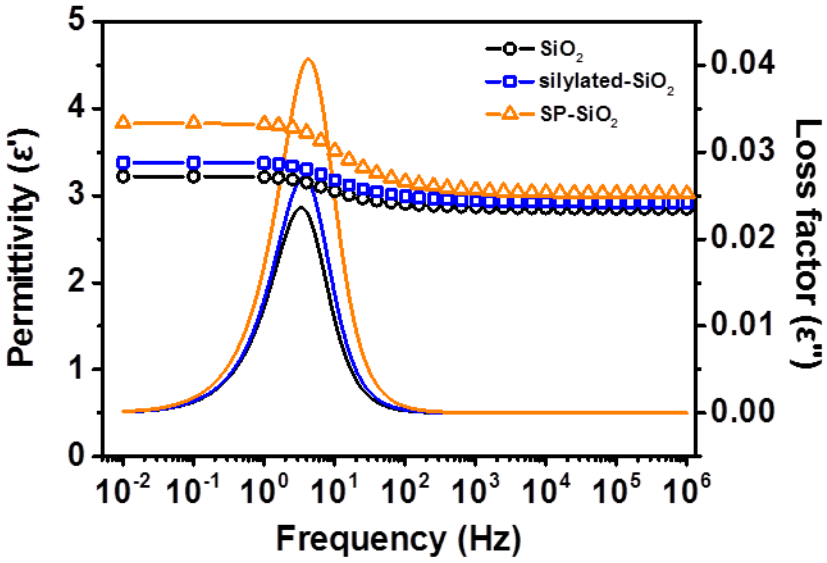

Figure 50. Dielectric constant (ε') and loss factor (ε'') of (a) SiO_2, silylated-SiO_2, and SP-SiO_2 nanomaterials-based ER smart fluids without lecithin as a function of *E* field frequency (*f*).

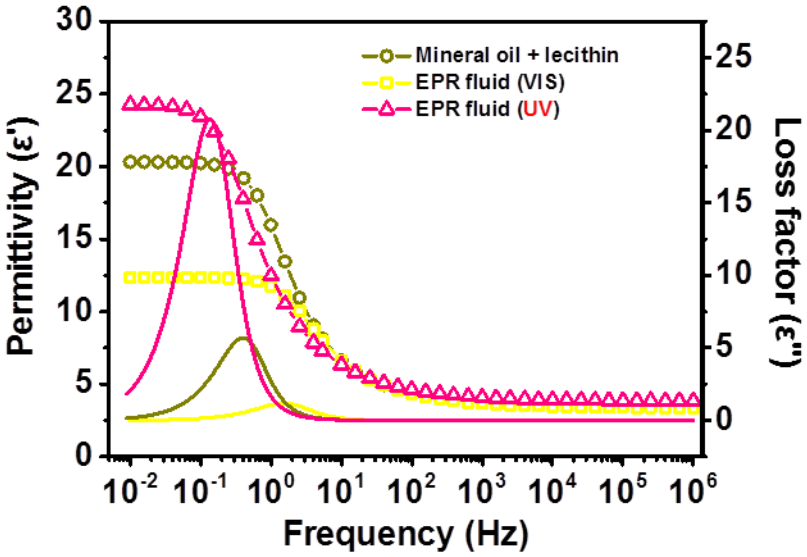

Figure 51. Dielectric constant (ε') and loss factor (ε'') EPR smart fluids under UV and VIS light applications as a function of *E* field frequency (*f*).

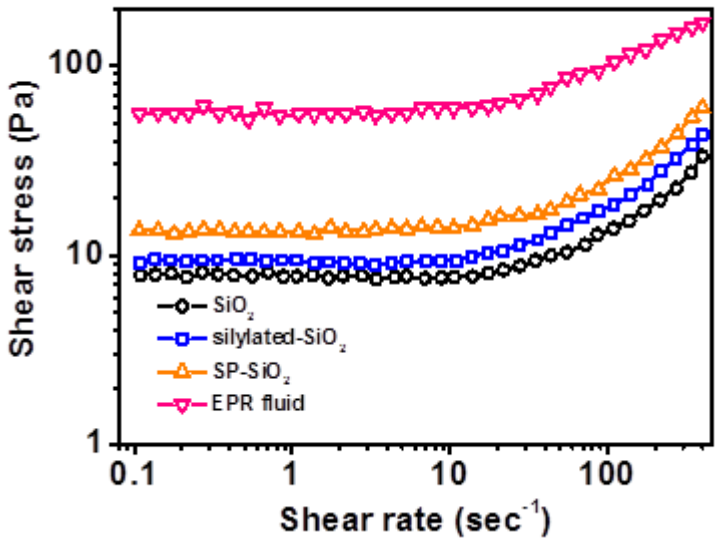

Figure 52. Shear stress curves of three ER smart fluids and EPR fluid as a function of shear rate (s^{-1}) under 2.0 kV mm^{-1} of *E* field strength.

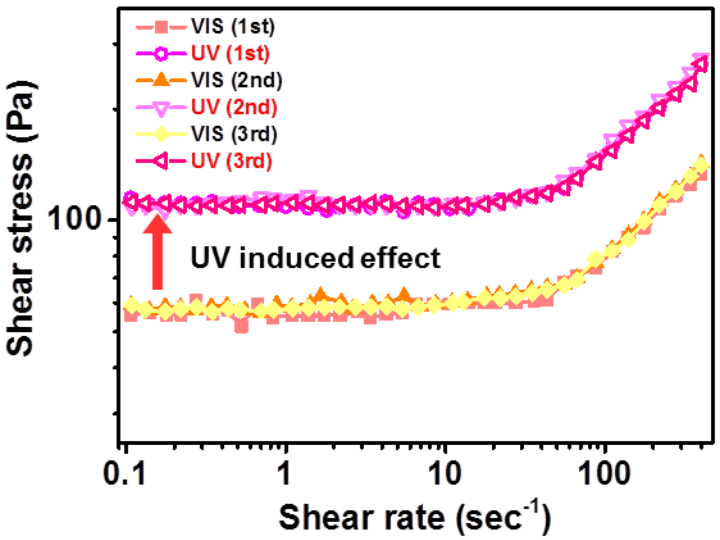

Figure 53. Shear stress curves of EPR smart fluid exposed to UV and VIS light (3 min) as a function of shear rate (s^{-1}) under 2.0 kV mm^{-1} of *E* field strength.

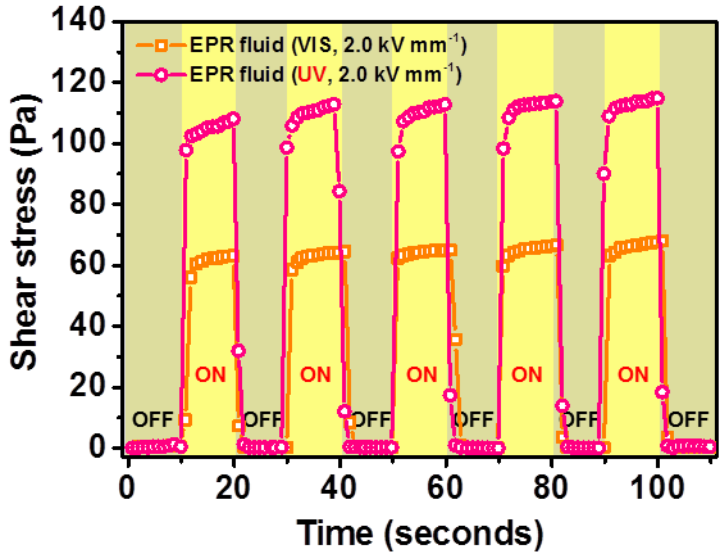

Figure 54. Yield stress of the EPR smart fluid exposed to UV and VIS light (3 min) as a function of *E* field strength (fixed shear rate of 0.1 s^{-1}).

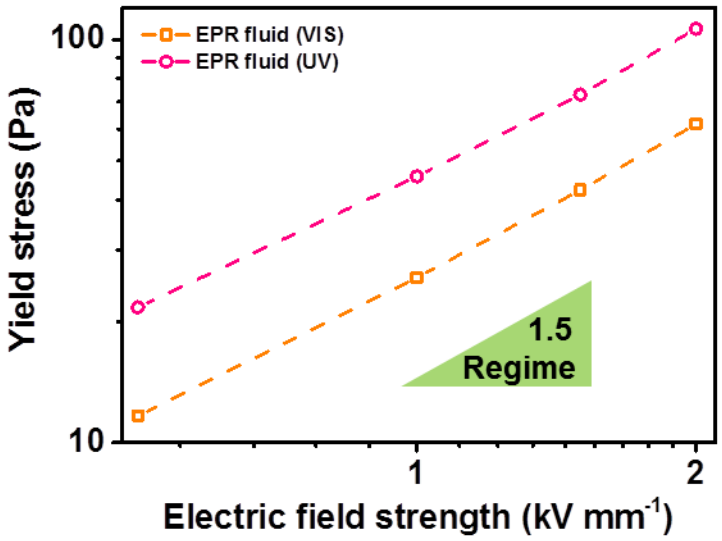

Figure 55. The *E* field on-off test of the EPR smart fluid by alternation of the *E* field strength with fixed shear rate of 0.1 s^{-1}.

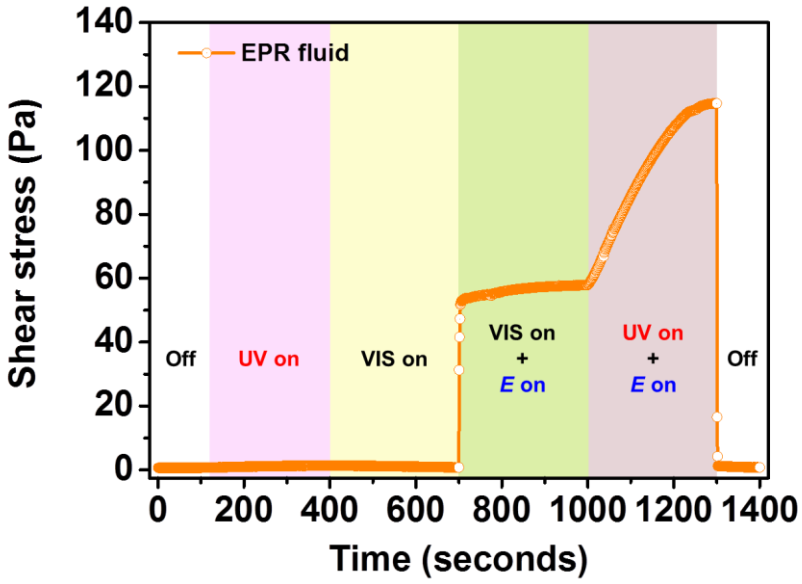

Figure 56. The real-time observation of EPR activity of EPR smart fluid under various conditions: UV light irradiation (4 W cm^{-2}), VIS light illumination, and *E* field (2.0 kV mm^{-1}) at the fixed shear rate of 0.1 s^{-1}.

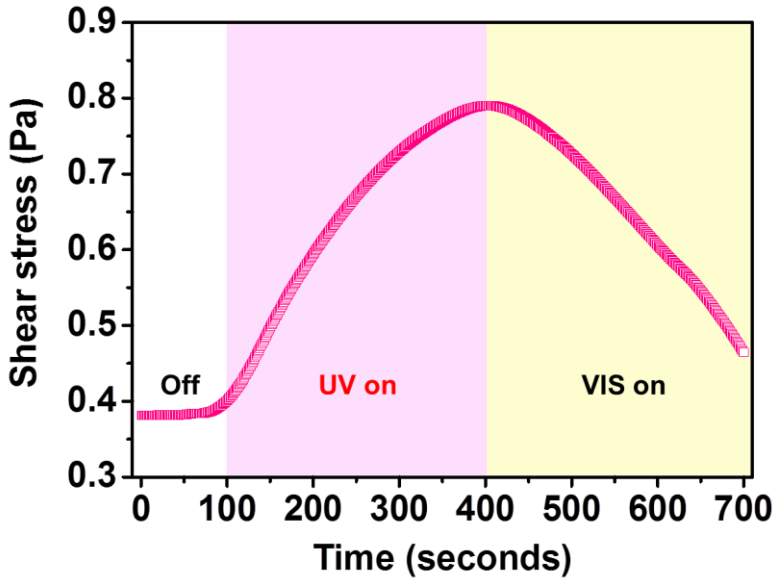

Figure 57. Magnified PR activity of EPR smart fluid over the time intervals from 0 to 700 s.

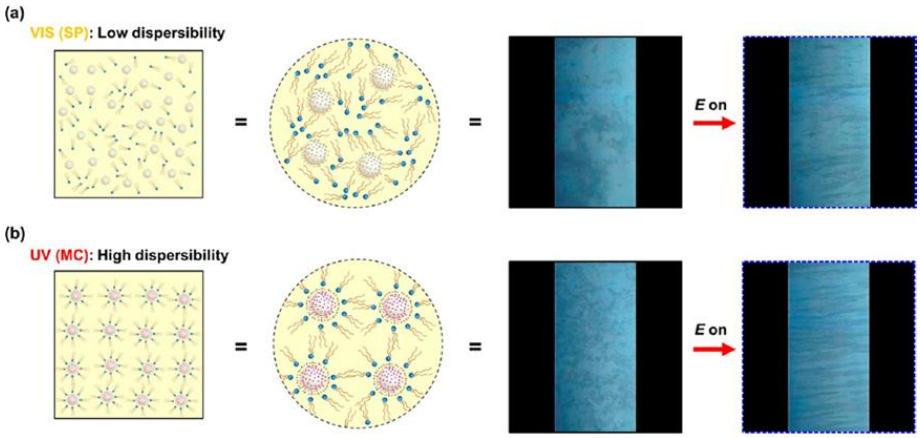

Figure 58. Proposed mechanism of the distributed state of SP-SiO_2 nanomaterials under (a) VIS light and (b) UV light, and resulting differences of fibril-like structure formations under applied *E* field strength of 2.0 kV mm^{-1}.

Table 9. Dielectric properties of EPR fluid, lecithin + mineral oil and ER fluids.[a]

Sample[b]	ε_0	ε_∞	$\Delta\varepsilon = (\varepsilon_0 - \varepsilon_\infty)$	f_{max} (Hz)[c]	λ (s)[d]
SiO_2-based ER smart fluid	2.85	3.22	0.37	3.27	0.048
Silylated-SiO_2-based smart ER fluid	2.92	3.38	0.46	3.65	0.043
SP-SiO_2-based ER smart fluid	3.02	3.83	0.81	4.08	0.039
Lecithin + mineral oil	3.66	20.32	16.66	0.71	0.22
EPR fluid (VIS)	3.37	12.36	8.99	1.63	0.098
EPR fluid (UV)	3.85	24.28	20.43	0.22	0.72

[a] Dielectric parameters were acquired by impedance analyzer (Solatron 1260) installed with dielectric interface (Solatron 1296).

[b] Concentration of ER and EPR fluids are set to 3.0 wt% in mineral oil. UV/VIS light was applied for 3min prior to determine the dielectric properties of EPR fluids.

[c] The f_{max} values of ER fluids were determined by nonlinear regression using OriginPro program.

[d] The relaxation time was determined using $\lambda = 1/(2\pi f_{max})$ relation.

Table 10. Detailed description of ER, PR and EPR activities of ER smart fluids and EPR smart fluid.

Sample[a]	*E* field strength	Light source[b]	Highest yield stress[c]
SiO_2-based ER smart fluid	2.0 kV mm^{-1}	-	7.7 Pa
Silylated-SiO_2-based ER smart fluid	2.0 kV mm^{-1}	-	9.4 Pa
SP-SiO_2-based ER smart fluid	2.0 kV mm^{-1}	-	14.1 Pa
EPR smart fluid (PR activity)	-	UV light	0.8 Pa
EPR smart fluid (ER activity)	2.0 kV mm^{-1}	VIS light	57.5 Pa
EPR smart fluid (EPR activity)	2.0 kV mm^{-1}	UV light	115.3 Pa

[a] Concentrations of EPR and ER fluids were set to 3.0 wt% in mineral oil.

[b] Intensity of UV light was 4 W cm^{-2}.

[c] Highest yield stress was determined from the origin program.

4. Conclusion

Three types of ER, EMR, and EPR smart fluids were successfully prepared by employing various mesoporous and hybridized silica nanomaterials; $mSiO_2$ nanomaterials with different *L/D*, $SiO_2/TiO_2@Fe_3O_4/SiO_2$ nanomaterial, and SP-SiO_2 nanomaterial. As-formulated smart fluids were highly responsive to external fields of *E* field, *H* field, and UV–VIS light, and successful rheological/mechanical changes were induced. The subtopic is concluded in the view point of each subtopic as follows:

1. The $mSiO_2$ nanomaterials with different *L/D* were facilely synthesized by the modified Stöber method using CTAB as a surfactant. The *L/D* of $mSiO_2$ nanomaterials were easily controlled by changing the amount of added water while fixing the amount of all other reagents. As-synthesized $mSiO_2$ nanomaterials were formulated as ER smart fluids by dispersing into silicone oil. The resulting $mSiO_2$ nanomaterials-based ER smart fluids displayed high ER performance under applied *E* field due to the enhanced dielectric properties and dispersion stabilities. Such enhancement in dielectric properties and dispersion stabilities were originated from the mesoporous nature and

high surface of $mSiO_2$ nanomaterials. Furthermore, the ER responsivity of $mSiO_2$ nanomaterials showed increasing trend with increment in *L/D* owing to the combined contributions from the geometrical effect and dipole moments.

2. The multi-layered $SiO_2/TiO_2@Fe_3O_4/SiO_2$ nanomaterials were successfully fabricated by the combination of various experimental methods like thermal decomposition, sol-gel, and silylation. Particularly, numerous Fe_3O_4 nanomaterials bearing the magnetic property was easily embedded into the ER responsive SiO_2/TiO_2 core/shell nanomaterial using APTES silane, which allowed the simultaneous ligand exchange and silylation reactions. The outermost SiO_2 shell coating added a corrosion resistance and improved dispersion stability characteristics to the final $SiO_2/TiO_2@Fe_3O_4/SiO_2$ nanomaterials. The resulting $SiO_2/TiO_2@Fe_3O_4/SiO_2$ nanomaterials-based EMR smart fluids demonstrated a successful ER and MR activity under applied *E* and *H* field, respectively. Moreover, synergistic effect of dual stimuli application was observed in the conditions of simultaneous application of *E* and *H* fields in the parallel direction.

3. Photosensitive SP-SiO_2 nanomaterials were readily prepared by the decoration of SP molecules onto the 50 nm-sized SiO_2 nanomaterials

via silylation. To formulate the dual compatible dispersing media for PR and ER applications, appropriate amount of lecithin molecule was added to the mineral oil. The EPR smart fluid was successfully formulated by dispersing as-synthesized SP-SiO_2 nanomaterials into the EPR dispersing media. Consequently, SP-SiO_2 nanomaterials-based EPR smart fluids showed a reversible PR activity attributed to the two different binding mechanisms of photo-isomerized SP molecule; non-polar SP under VIS light and polar MC under UV light, and lecithin molecule. Also, SP-SiO_2 nanomaterials-based EPR smart fluids exhibited sufficient ER characteristics due to the presence of SiO_2 core materials. Finally, EPR smart fluids manifested a successful dual EPR activity under simultaneous applications of UV–VIS lights and *E* fields. Notably, the EPR performance of UV-irradiated EPR smart fluid demonstrated the 144 fold- and 2 fold- higher shear stresses in relative to single stimuli-applied PR and ER activity, denoting the successful combined effects of PR and ER responsivity in one place.

References

[1] A. Bianco, H.-M. Cheng, T. Enoki, Y. Gogotsi, R. H. Hurt, N. Koratkar, T. Kyotani, M. Monthioux, C. R. Park, J. M. D. Tacson, J. Zhang, Carbon, **2013**, 65, 1.

[2] D. Stievenard, B. Legrand, Prog. Surf. Sci., **2010**, 2, 441.

[3] T. Tsuzuki, Int. J. Nanotechnol., **2009**, 6, 567.

[4] C. Sanchez, P. Belleville, M. Popall, L. Nicole, Chem. Soc. Rev., **2011**, 40, 696.

[5] A. C. Grimsdale, K. Mullen, Angew. Chem. Int. Ed., **2005**, 44, 5592.

[6] Q. Zhang, J.-Q. Huang, W.-Z. Qian, Y.-Y. Zhang, F. Wei, Small, **2013**, 9, 1237.

[7] K. Ariga, T. Mori, J. P. Hill, Adv. Mater, **2012**, 24, 158.

[8] R. Valiev, Nature, **2002**, 419, 887.

[9] N. Saleh, H.-J. Kim, T. Phenrat, K. Matyjaszewski, R. D. Tilton, G. V. Lowry, Environ. Sci. Technol., **2008**, 42, 3349.

[10] B. S. Avinash, V. S. Chaturmurkha, H. S. Jayanna, C. S. Naveen, M. P. Rajeeva, B. M. Harish, S. Suresh, A. R. Lamani, AIP Conf. Proc., **2016**, 1728, 020426.

[11] C. R. M. Wronski, Br. J. Appl. Phys., **1967**, 18, 1731.

[12] Y. Huang, X. Duan, C. M. Lieber, Small, **2005**, 1, 142.

[13] S. Lee, J.-Y. Hong, J. Jang, J. Colloid Interface Sci., **2013**, 398, 22.

[14] W. Zhou, L. Yan, Y. Wang, Y. Zhang, Appl. Phys. Lett., **2006**, 89, 013105.

[15] J. Liu, D. M. Aruguete, M. Murayama, M. F. Hochell Jr., Environ. Sci. Technol., **2009**, 43, 8178.

[16] Y. Guo, K. Xu, C. Wu, J. Zhao, Y. Xie, Chem. Soc. Rev., **2015**,

44, 637.
[17] Z.-Y. Zhou, N. Tian, J.-T. Li, I. Broadwell, S.-G. Sun, Chem. Soc. Rev., **2011**, 40, 4167.
[18] F. Sanchez, K. Sobolev, Constr. Build. Mater., **2010**, 24, 2060.
[19] G. Chen, I. Roy, C. Yang, P. N. Prasad, Chem. Rev., **2016**, 116, 2826.
[20] G. Chen, H. Qiu, P. N. Prasad, X. Chen, Chem. Rev., **2014**, 114, 5161.
[21] C. P. Brown, Nat. Rev. Rheumatol., **2013**, 9, 614.
[22] J. R. Bakke, K. L. Pickrahn, T. P. Brennan, S. F. Bent, Nanoscale, **2011**, 3, 3482.
[23] A. T. Bell, Science, **2003**, 299, 1688.
[24] H. Gleiter, Acta Mater., **2000**, 14, 1.
[25] Y. Li, W. Kim, Y. Zhang, M. Rolandi, D. Wang, H. Dai, J. Phys. Chem. B, **2001**, 105, 11424.
[26] J. Fan, S. W. Boettcher, G. D. Stucky, Chem. Mater., **2006**, 18, 6391.
[27] N. Anton, J.-P. Benoit, P. Saulnier, J. Control Release, **2008**, 128, 185.
[28] J. Gao, H. Gu, B. Xu, Accounts. Chem. Res., **2009**, 42, 1097.
[29] T. Zhai, X. Fang, M. Liao, X. Xu, H. Zeng, B. Yoshino, D. Golberg, Sensors, **2009**, 9, 6504.
[30] D. R. Radu, C.-Y. Lai, K. Jeftinija, E. W. Rowe, S. Jeftinija, V. S.-Y. Lin, J. Am. Chem. Soc., **2004**, 126, 13216.
[31] R. P. Bagwe, L. R. Hilliard, W. Tan, Langmuir, **2006**, 22, 4357.
[32] F. Tang, L. Li, D. Chen, Adv. Mater., **2012**, 24, 1504.
[33] C. Bharti, U. Nagaich, A. K. Pal, N. Gulati, Int. J. Pharm Investig, **2015**, 5, 124.
[34] J. J. Gaitero, I. Campillo, A. Guerrero, Cement Concrete Res., **2008**, 38, 1112.

[35] T. Tsutsui, M. Yahiro, H. Yokogawa, K. Kawano, M. Yokoyama, Adv. Mater., **2001**, 13, 1149.
[36] A. Sayari, B.-H. Han, Y. Yang, J. Am. Chem. Soc., **2004**, 126, 14348.
[37] H. M. Lim, J. Lee, J.-H. Jeong, S.-G. Oh, S.-H. Lee, Engineering, **2010**, 2, 998.
[38] C. Huan, S.Shu-Qing, Chin. Phys. B, **2014**, 23, 088102.
[39] A. E. Voinescu, M. Kellermeier, A. M. Carnerup, A.-K. Larsson, D. Touraud, S. T. Hyde, W. Kunz, J. Cryst. Growth, **2007**, 306, 152.
[40] F. J. Arriagada, K. Osseo-Asare, J. Colloid Interface Sci., **1999**, 211, 210.
[41] A. Liberman, N. Mendez, W. C. Trogler, A. C. Kummel, Sur. Sci. Rep., **2014**, 69, 132.
[42] G. J. Owens, R. K. Singh, F. Foroutan, M. Alaqaysi, C.-M. Han, C. Mahapatra, H.-W. Kim, J. Knowles, Prog. Mater. Sci., **2016**, 77, 1.
[43] L. P. Singh, S. K. Bhattacharyya, R. Kumar, G. Mishra, U. Sharma, G. Singh, S. Ahalawat, Adv. Colloid Interfac., **2014**, 214, 17.
[44] W. Stöber, A. Fink, J. Colloid Interface Sci., **1968**, 26, 62.
[45] S. L. Greasley, S. J. Page, S. Sirovica, S. Chen, R. A. Martin, A. Riveiro, J. V. Hanna, A. E. Porter, J. R. Jones, J. Colloid Interface Sci., **2016**, 469, 213.
[46] K. Nozawa, H. Gailhanou, L. Raison, P. Panizza, H. Ushiki, E. Sellier, J. P. Delville, M. H. Delville, Langmuir, **2005**, 21, 1516.
[47] Y. Han, Z. Lu, Z. Teng, J. Liang, Z. Guo, D. Wang, M.-Y. Han, W. Yang, Langmuir, **2017**, 33, 5879.
[48] C.-M. Yoon, S. Lee, S. H. Hong, J. Jang, J. Colloid Interface Sci., **2015**, 438, 14.
[49] S. Lee, C.-M. Yoon, J.-Y. Hong, J. Jang, J. Mater. Chem. C, **2014**, 2, 6010.
[50] I. A. Rahman, V. Padavettan, J. Nanomater, **2012**, 2012, 132424.

[51] X.-C. Guo, P. Dong, Langmuir, **1999**, 15, 5535.
[52] D. Napierska, L. C. J. Thomassen, V. Rabolli, D. Lison, L. Gonzalez, M. Kirsch-Volders, J. A. Martens, P. H. Hoet, Small, **2009**, 5, 846.
[53] C. O. Metin, L. W. Lake, C. R. Miranda, Q. P. Nguyen, J. Nanopart. Res., **2011**, 13, 839.
[54] J. D. Rimer, R. F. Lobo, D. G. Vlachos, Langmuir, **2005**, 21, 8960.
[55] K. S. Rao, K. El-Hami, T. Kodaki, K. Matsushige, K. Makino, J. Colloid Interface Sci., **2005**, 289, 125.
[56] T. Yu, A. Malugin, H. Ghandehari, ACS Nano, **2011**, 5, 5717.
[57] N. Kröger, R. Deutzmann, M. Sumper, Science, **1999**, 286, 1129.
[58] L. M. Rossi, L. Shi, F. H. Quina, Z. Rosenzweig, Langmuir, **2005**, 21, 4277.
[59] J. L. Vivero-Escoto, I. I. Slowing, C.-W. Wu, V. S.-Y. Lin, J. Am. Chem. Soc., **2009**, 131, 3462.
[60] L. P. Singh, S. K. Agarwal, S. K. Bhattacharyya, U. Sharma, S. Ahalawat, Nanomater. Nanotechnol., **2011**, 1, 44.
[61] Y. Otsubo, M. Sekine, S. Katayama, J. Colloid Interface Sci., **1992**, 150, 324.
[62] A. A. Beltran-Osuna, B. Cao, G. Cheng, S. C. Jana, M. P. Espe, B. Lama, Langmuir, **2012**, 28, 9700.
[63] J. Ryu, W. Kim, J. Yun, K. Lee, J. Lee, J. H. Kim, J. J. Kim, J. Jang, ACS Appl. Mater. Interfaces, **2018**, 10, 11843.
[64] P. Wang, S. M. Zakeeruddin, P. Comte, I. Exnar, M. Gratzel J. Am. Chem. Soc., **2003**, 125, 1166.
[65] H. Abe, I. Abe, K. Sato, M. Naito, J. Am. Ceram. Soc., **2005**, 88, 1359.
[66] H. Dun, W. Zhang, Y. Wei, S. Xiuqing, Y. Li, L. Chen, Anal. Chem., **2004**, 76, 5016.

[67] D. K. Yi, S. T. Selvan, S. S. Lee, G. C. Papaefthymiou, D. Kundaliya, J. Y. Ying, J. Am. Chem. Soc., **2005**, 127, 4990.
[68] P. K. Jal, S. Patel, B. K. Mishra, Talanta, **2004**, 62, 1005.
[69] H. Y. Son, K. R. Kim, J. B. Lee, T. H. L. Kim, J. Jang, S. J. Kim, M. S. Yoon, J. W. Kim, Y. S. Nam, Scientific Reports, **2017**, 7, 14728.
[70] S. Wang, Z. Ahmad, J. E. Mark, Chem. Mater., **1994**, 6, 943.
[71] J. Wang, S. Zhang, Nanoscale, **2014**, 6, 4418.
[72] A. Walcarius, Chem. Mater., **2001**, 13, 3351.
[73] A. Bitar, N. M. Ahmad, H. Fessi, A. Elaissari, Drug Discov. Today, **2012**, 17, 1147.
[74] U. Goeri, A. Hunsche, A. Mueller, H. G. Koban, Rubber Chem. Technol., **1997**, 70, 608.
[75] Y. Sun, Z. Zhang, C. P. Wong, J. Colloid Interface Sci., **2005**, 292, 436.
[76] V. Biju, Chem. Soc. Rev., **2014**, 43, 744.
[77] H. K. Hunt, C. Soteropulos, A. M. Armani, Sensors, **2010**, 10, 9317.
[78] Y. Xie, C. A. S. Hill, Z. Xiao, H. Militz, C. Mai, Compos. Part A-Appl. S, **2010**, 41, 806.
[79] P. V. D. Voort, E. F. Vansant, J. Liq. Chromatogr. R. T., **1996**, 19, 2723.
[80] J. D. L. Grange, J. L. Markham, Langmuir, **1993**, 9, 1749.
[81] I. Shimizu, H. Okabayashi, K. Taga, Colloid. Polym. Sci., **1997**, 275, 555.
[82] M. Ueda, H.-B. Kim, K. Ichimura, J. Mater. Chem., 1994, 4, 883.
[83] S. I. Stoeva, F. Huo, J.-S. Lee, C. A. Mirkin, J. Am. Chem. Soc., **2005**, 127, 15362.
[84] S. Kim, Y. Jang, W.-K. Oh, C. Kim, J. Jang, Adv. Healthcare. Mater., **2014**, 3, 1097.
[85] J.-Y. Hong, J. Jang, Soft Matter, **2010**, 6, 4669.

[86] S. Liu, M.-Y. Han, Chem. Asian. J., **2010**, 5, 36.
[87] J. Yin, X. Wang, R. Chang, X. Zhao, Soft Matter, **2012**, 8, 294.
[88] Y. D. Liu, H. J. Choi, Soft Matter, **2012**, 8, 11961.
[89] J.-Y. Hong, M. Choi, C. Kim, J. Colloid Interface Sci., **2010**, 347, 177.
[90] S. G. Kim, J. Y. Lim, J. H. Sung, H. J. Choi, Y. Seo, Polymer, **2007**, 48, 6622.
[91] C.-M. Yoon, Y. Jang, J. Noh, J. Kim, J. Jang, ACS Nano, **2017**, 11, 9789.
[92] Y. D. Liu, F. F. Fang, H. J. Choi, Soft Matter, **2011**, 7, 2782.
[93] M. S. Cho, Y. H. Cho, H. J. Choi, M. S. Jhon, Langmuir, **2003**, 19, 5875.
[94] B. J. Park, F. F. Fang, H. J. Choi, Soft Matter, **2010**, 6, 5246.
[95] Y. D. Liu, F. F. Fang, H. J. Choi, Mater. Lett., **2010**, 64, 154.
[96] F. F. Fang, H. J. Choi, M. S. Jhon, Colloid Surface A, **2009**, 351, 46.
[97] B.-X. Wang, Y. Zhao, X.-P. Zhao, Colloid Surface A, **2007**, 295, 27.
[98] M. Zhang, X. Gong, W. Wen, Electrophoresis, **2009**, 30, 3116.
[99] P. Sheng, W. Wen, Annu. Rev. Fluid. Mec., **2011**, 44, 143.
[100] C. A. Kim, M. S. Jhon, H. J. Choi, Chem. Mater., **2001**, 13, 1243.
[101] S. Lee, J. Lee, S. H. Hwang, J. Yun, J. Jang, ACS Nano, **2015**, 9, 4939.
[102] W. L. Zhang, H. J. Choi, Chem Commun., **2011**, 47, 12286.
[103] J.-Y. Hong, J. Jang, Chem. Commun., **2012**, 8, 3348.
[104] K.-Y. Shin, S. Lee, S. H. Hong, J. Jang, ACS Appl. Mater. Interfaces, **2014**, 6, 5531.
[105] J.-Y. Hong, E. Kwon, J. Jang, Soft Matter, **2009**, 5, 951.
[106] N. Makris, S. A. Burton, D. P. Taylor, Smart Mater. Struct.,

1996, 5, 551.
[107] M. Parthasarathy, D. J. Klingenberg, Mater. Sci. Eng., **1996**, 17, 57.
[108] H. Block, J. P. Kelly, A. Qin, T. Watson, Langmuir, **1990**, 6, 6.
[109] C.-M. Yoon, J. Noh, Y. Jang, J. Jang, RSC Adv., **2017**, 7, 19754.
[110] D. D. Lin, Z. J. Zhang, B. Y. Zhao, L. S. Chen, K. Hu, Smart Mater. Struct., **2006**, 15, 1641.
[111] G. C. Teare, N. M. Ratcliffe, J. Mater. Chem., **1996**, 6, 301.
[112] F. Ikazaki, K. Uchida, T. Kawakami, K. Edamura, K. Sakurai, H. Anzai, Y. Asako, J. Phys. D Appl. Phys., **1998**, 31, 336.
[113] T. Hao, Adv. Mater., **2001**, 13, 1847.
[114] I. B. Jang, H. B. Kim, J. Y. Lee, J. L. You, H. J. Choi, J. Appl. Phys., **2005**, 97, 10Q912.
[115] S. T. Lim, M. S. Cho, I. B. Jang, H. J. Choi, J. Magn. Magn. Mater., **2004**, 282, 170.
[116] J. S. Choi, B. J. Park, M. S. Cho, H. J. Choi, J. Magn. Magn. Mater., **2006**, 304, e374.
[117] S. T. Lim, M. S. Cho, I. B. Jang, H. J. Choi, M. S. Chon, IEEE T. Magn, **2004**, 40, 3033.
[118] S. T. Lim, H. J. Choi, M. S. Jhon, IEEE T. Magn, **2005**, 41, 3745.
[119] S. J. Dyke, B. F. Spencer Jr., M. K. Sain, J. D. Carlson, Smart Mater. Struct., **1996**, 5, 565.
[120] J. de Vicente, D. J. Klingenberg, R. Hidalgo-Alvarez, Soft Matter, **2011**, 7, 3701.
[121] J. M. Ginder, L. C. Davis, Appl. Phys. Lett., **1994**, 65, 3410.
[122] B. D. Chin, J. H. Park, M. H. Kwon, O. O. Park, Rheol. Acta, **2001**, 40, 211.
[123] K. H. Song, B. J. Park, H. J. Choi, IEEE T. Magn, **2009**, 45, 4045.

[124] M. Mrlik, M. Ilčíková, V. Pavlinek, J. Mosnáček, P. Peer, P. Filip, J. Colloid Interface Sci., **2013**, 396, 146.
[125] M.-Y. Cho, J.-S. Kim, H. J. Choi, S.-B. Choi, G.-W. Kim, Smart Mater. Struct., **2017**, 26, 054007.
[126] M. Pereira, C. R. Leal, A. J. Parola, U. M. Scheven, Langmuir, **2010**, 26, 16715.
[127] S. Peng, Q. Guo, T. C. Hughes, P. G. Hartley, Langmuir, **2014**, 30, 866.
[128] K. Sun, R. Kumar, D. E. Falvey, S. R. Raghavan, J. Am. Chem. Soc., **2009**, 131, 7135.
[129] A. M. Ketner, R. Kumar, T. S. Davies, P. W. Elder, S. R. Raghavan, J. Am. Chem. Soc., **2007**, 129, 1553.
[130] L. E. Schmidt, Y. Leterrier, J.-M. Vesin, M. Wilhelm, J.-A. E. Manson, Macromol. Mater. Eng, **2005**, 290, 1115.
[131] H.-Y. Lee, K. K. Diehn, K. Sun, T. Chen, S. R. Raghavan, J. Am. Chem. Soc., **2011**, 133, 8461.
[132] K. Minagawa, T. Watanabe, K. Koyama, M. Sasaki, Langmuir, **1994**, 10, 3926.
[133] K. Koyama, K. Minagawa, T. Watanabe, Y. Kumakura, J.-i. Takimoto, J. Non-Newtonian Fluid Mech., **1995**, 58, 195.
[134] W. Wen, P. Sheng, Physica B, **2003**, 338, 343.
[135] C. Echeverria, P. Soares, A. Robalo, L. Pereira, C. M. M. Novo, I. Ferreira, J. P. Borges, Mater. Design, **2015**, 86, 745.
[136] J.-G. Guan, J. Huang, S.-L. Zhao, R.-Z. Yuan, Wuhan. Univ. Technol., **2001**, 15, 599.
[137] J. de Vicente, A. V. Delgado, R. C. Plaza, J. D. G. Duran, F. Gonzalez-Cabellero, Langmuir, **2000**, 16, 7954.
[138] A. Shibayama, T. Miyazaki, K. Yamaguchi, K. Murakami, T. Fujita, Int. J. Mod, Phys. B, **2002**, 16, 2405.
[139] S. K. Tan, X. P. Song, Q. Li, H. Y. Guo, S. Ji, H. Zhao, Adv.

Mater. Res., **2011**, 211-212, 775.
[140] X. Tian, K. He, B. Wang, S. Yu, C. Hao, K. Chen, Q. Lei, Colloid Surface A, **2016**, 498, 185.
[141] D. E. Park, H. S. Chae, H. J. Choi, A. Maity, J. Mater. Chem. C, **2015**, 3, 3150.
[142] S. K. Tan, X. P. Song, Q. Li, H. Y. Guo, S. Ji, H. Zhao, Mater. Sci. Forum, **2011**, 687, 519.
[143] B. Sim, H. S. Chae, H. J. Choi, eXPRESS Polym. Lett., **2015**, 9, 736.
[144] F. F. Fang, Y. D. Liu, H. J. Choi, Colloid Polym. Sci., **2013**, 291, 1781.
[145] J. Noh, S. Hong, C.-M. Yoon, S. Lee, J. Jang, Chem. Commun, **2017**, 53, 6645.
[146] S. Lee, J. Noh, S. Hong, Y. K. Kim, J. Jang, Chem. Mater., **2016**, 28, 2624.
[147] H. Wang, P. V. D. Voort, H. Qu, S. Liu, J. Nanopart. Res., **2013**, 15, 1501.
[148] C.-M. Yoon, K. Lee, J. Noh, S. Lee, J. Jang, J. Mater. Chem. C, **2016**, 4, 1713.
[149] K. Lee, C.-M. Yoon, J. Noh, J. Jang, Chem. Commun., **2016**, 52, 4231.
[150] E. A. Ustinov, Langmuir, **2008**, 24, 6668.
[151] J. Liu, S. Ma, L. Zang, Appl. Surf. Sci., **2013**, 265, 393.
[152] M. S. Cho, H. J. Choi, W.-S. Ahn, Langmuir, **2004**, 20, 202.
[153] J. Wu, T. Jin, F. Liu, J. Guo, P. Cui, Y. Cheng, G. Xu, J. Mater. Chem. C, **2014**, 2, 7541.
[154] H. J. Choi, M. S. Cho, K.-K. Kang, W.-S. Ahn, Microporous Mesoporous Mater., **2000**, 39, 19.
[155] Y. D. Liu, X.-M. Quan, B. M. Lee, I. G. Kim, H. J. Choi, J. Mater. Sci., **2014**, 49, 2618.

[156] J. Yin, R. Chang, Y. Kai, X. Zhao, Soft Matter, **2013**, 9, 3910.
[157] S. Park, M. Cho, S. Lim, H. J. Choi, M. Jhon, Macromol. Chem. Phys., 2005, **26**, 1563.
[158] J. Yin, X. Xia, L. Xiang, X. Zhao, J. Mater. Chem., 2010, **20**, 7096.
[159] N. Moradian, D. S.-K. Ting, S. Cheng, Exp. Therm. Fluid Sci., 2009, **33**, 460.
[160] Y. Sun, M. Thomas, J. Masounave, Smart Mater. Struct., 2009, **18**, 024004.
[161] Z.-J. Tan, X.-W. Zou, W.-B. Zhang, Z.-Z. Jin, Phys. Rev. E, 1999, **59**, 3177.
[162] J. Yin, X. Xia, L. Xiang, X. Zhao, Smart Mater. Struct., 2011, **20**, 015002.
[163] B. Wang, X. Zhao, Langmuir, 2005, **21**, 6553.
[164] J. Wu, Z. Song, F. Liu, J. Guo, Y. Cheng, S. Ma, G. Xu, NPG Asia Materials, 2016, **8**, e322.
[165] C.-M. Yoon, J. Ryu, J. Yun, Y. K. Kim, J. Jang, ACS Appl. Mater. Interfaces, 2018, **10**, 6570.
[166] S. S. Dukhin, Dielectric Properties of Disperse Systems, Wiley-Interscience, New York, 1971.
[167] Z. Xu, Y. Sun, J. Am. Chem. Sco., 2007, **129**, 8698.
[168] Y. Jang, S. Kim, S. Lee, C.-M. Yoon, I. Lee, J. Jang, Chem. Eur. J., 2017, **23**, 1.
[169] R. De Palma, S. Peeters, M. J. V. Bael, H. V. D. Rul, K. Bonroy, W. Laureyn, J. Mullens, G. Borghs, G. Maes, Chem. Mater., 2007, **19**, 1821.
[170] M. Sabzi, S. M. Mirabedini, J. Zohurianan-Mehr, M. Atai, Prog. Org. Coating, 2009, **65**, 222.
[171] A. M. Demin, A. G. Pershina, V. V. Ivanov, K. V. Nevskaya, O. B. Shevelev, A. S. Minin, I. V. Byzov, A. E. Sazanov, V. P. Krasnov,

L. M. Ogorodova, Int. J. Nanomedicine, 2016, **11**, 4451.
[172] A. M. Demin, V. P. Krasnov, V. N. Crarushin, Mendeleev Commun., 2013, **23**, 14.
[173] A. N. Murashkevich, A. S. Lavitskaya, T. I. Barannikova, I. M. Zharskii, J. Appl. Spectrosc., 2008, **75**, 730.
[174] R. Han, W. Li, M. Zhu, D. Zhou, F. Li, Sci. Rep., 2014, **4**, 7493.
[175] C.-L. Li, J.-K. Chen, S.-K. Fan, F.-H. Ko, F.-C., Chang, ACS Appl. Mater. Interfaces, 2012, **4**, 5650.
[176] Y. Liu, F.-H. Liao, J.-R. Li, S.-H. Zhang, S.-M. Chen, C.-G. Wei, S. Gao, Scripta Mater., 2006, **54**, 125.
[177] R. Stanway, Mater. Sci. Tech. Ser., 2004, **20**, 931.
[178] A. Julia-Lopez, J. Hernando, D. Ruiz-Molina, P. Gonzalez-Monje, J. Sedo, C. Roschini, Angew. Chem. Int. Ed., 2016, **55**, 15044.
[179] J. Yin, X. Xia, X. Wang, X. Zhao, Soft Matter, 2011, **7**, 10978.
[180] C.-M. Yoon, G. Lee, J. Noh, C. Lee, O. J. Cheong, J. Jang, Chem. Commun., 2016, **52**, 4808.
[181] C.-M. Yoon, S. H. Hong, J. Jang, J. Colloid Interfaces Sci., 2015, **438**, 14.

국문초록

지능형 유체는 외부 자극에 감응할 수 있는 분산물질이 용매에 분산되어 이루어져 있다. 이러한 지능형 유체는 다양한 외부 자극에 감응하여 유변적/물성적 변화를 일으킬 수 있다. 지능형 유체는 빠른 반응성, 낮은 소비전력, 그리고 가역성 등의 다양한 장점으로 인해 학계와 산업분야에서 큰 관심을 받고 있다. 지능형 유체 중에서도 인가된 전기장, 자기장, 빛 하에서 반응할 수 있는 전기반응형, 자기반응형, 광반응형 유체들이 매우 많은 관심을 받고 있다. 근래에는 나노 기술의 발전과 함께 종래의 마이크로 크기 지능형 유체 분산물질이 나노 물질로 점점 대체 되고 있다. 다양한 나노 물질 중에서도 실리카 나노 물질은 대량 생산의 용이성, 균일성, 열 안정성, 크기 조절, 혼합의 용이성 등의 장점으로 인해 지능형 유체의 분산물질로써 적합하다. 하지만, 외부 자극에 더욱 감응성이 높은 실리카 나노 물질 개발의 필요성은 여전히 대두 되고 있다.

본 논문에서는 전기장, 자기장, 빛에 효과적으로 반응할 수 있는 실리카 나노 물질을 기반으로 한 지능형 유체의

효과적인 제조 방법에 대한 접근법과 유변적/물성적 변화의 성능 향상에 관한 방법을 제시한다. 첫 번째로, 실리카 나노 막대를 다공성 및 다양한 종횡비로 제조하여서 지능형 유체의 분산물질로 활용하였다. 그 결과, 다공성 실리카 나노 막대는 향상된 유전율과 분산성으로 인해 높은 전기반응성을 보여주었다. 두 번째로, 다층 구조의 산화철이 도입된 실리카 나노 물질을 순차적인 방법으로 제조하였다. 다양한 물질의 성공적인 혼합을 통해 다층 구조의 산화철이 도입된 실리카 나노 물질은 전기장과 자기장에 동시에 반응하는 특성을 보여주었다. 마지막으로, 간단한 실란 처리를 통해서 감광성의 스피로피란을 도입한 실리카 나노 물질을 제조하였다. 스피로피란이 도입된 실리카 나노 물질은 전기장과 빛에 우수한 동시 반응성을 보여주었다. 본 논문은 전기장, 자기장, 빛에 감응하는 실리카 나노물질을 기반으로 하는 지능형 유체들의 제조법과 함께 다양한 외부 자극으로의 감응성 향상에 대한 높은 잠재성을 시사한다.

주요어: 실리카 나노물질, 지능형 유체, 자극 감응성, 전기장, 자기장, 빛

학 번: 2013-23167

감사의 글

먼저, 태어났을 때부터, 미국 유학 기간, 박사학위 과정을 포함한 모든 인생의 기간 동안 저와 함께 하시고 더 나은 방향으로 나아가게 해주신 하나님께 감사드립니다. 2013년에 아무것도 모른 채로 막연히 대학원에 진학하였지만, 막상 모든 시간이 지나고 보니 고분자재료 연구실에서 박사학위를 받게 된 것은 저에게 다시 돌아올 수 없는 행운이라고 생각합니다. 박사학위 기간동안 학문적으로도 인격적으로도 부족한 저의 모습을 많이 느낄 수 있었고 많이 발버둥쳤지만, 역시 좀 더 잘 할 수 있지 않았을까 하는 아쉬움이 많이 남습니다. 많은 분들의 도움을 통해서 제가 무사히 학위를 받을 수 있었습니다. 평생에 한번뿐인 이 박사학위가 부끄럽지 않게 사회에 나가서도 모든 일에 최선을 다하고 고분자재료 연구실의 정신을 잊지 않겠습니다. 매우 짧은 이 글을 통해서 고마운 분들에게 저의 감사함을 전달하고자 합니다.

저의 지도 교수님이신 장정식 교수님께 진심으로 감사를 전하고 싶습니다. 처음 등교하였던 날, 아침 7시에 일을 하고

계시던 교수님의 모습이 아직도 선합니다. 부족한 저를 학문적으로도 훌륭히 지도하여 주셨고, 저를 인격적으로도 신앙적으로도 이끌어 주셔서 너무 감사합니다. 교수님의 부지런하신 모습, 포기하지 않는 모습, 그리고 솔선수범 하시는 모습을 항상 되새기며, 아직 많이 부족하지만 교수님을 조금이나마 닮아갈 수 있는 사람이 되도록 노력하겠습니다. 교수님 다시 한번 모든 것들에 감사드립니다. 또한, 바쁘신 와중에도 저의 논문을 심사해 주셨던 조재영, 김영규, 이종찬 교수님을 비롯하여 임순호 박사님께 깊은 감사인사를 드립니다.

다음으로 실험실 생활을 함께하였던 모든 분들에게 감사하다는 말씀을 전하고 싶습니다. 실험실 생활 동안 많은 좋은 추억을 만들어주신 선배님과 후배님들 에게 정말 감사드리고 제가 폐를 끼쳤던 부분에 대해서 죄송하다는 말을 동시에 전하고 싶습니다. 실험과 논문작성의 방법을 물심양면으로 알려주었던 이제는 교수가 된 저의 사수 승애, 부족한 나를 정말 잘 따라주었던 미래의 교수가 될 부사수 정철이, 모든 운동을 함께 하였던 팀 선배 근영이형, 삶의 요령을 알려주셨던 임스형, ER의 모든 기반을 닦아놓으신 진용이형, 평생 기억에 남을 추억을 공유한 삼형제 중

동생들인 경섭이와 갑을병정욱재, 총각일 때부터 웃음이 예쁜 윤기, 그리고 이젠 동기가 아닌 후배가 된 영덕이, 축구와 농구를 정말 재밌게 같이 한 잘생긴 기수와 사대주의 해준이, 같은 교회를 다니지만 아직 얼굴은 못 본 내 옆자리 경희, 많은 실험과 논문을 함께쓴 너무 고마운 윤선이, 나 때문에 고생이 많았을 재간 넘치는 중원이, 긴다리로 오토바이를 타는 원주, 타잔과 같은 배드민턴 왕 우영이, 나 때문에 정말 고생 많았을 정균이, 군대를 씩씩하게 잘 다녀온 성근이, 비트코인 부자 지후, 더 빨리 친해지지 못해서 아쉬웠던 지현이, 연구를 열심히 하는 모습으로 항상 귀감이 된 준섭이형, 축구의 재미를 알게해주었던 동훈이형, 재밌는 말씀을 많이 해주셨던 조성훈 교수님, 항상 재치 넘치는 성대모사왕 인규, 영덕이 대신 동기가 된 고은이, 석사24 예리, 그리고 MRS를 함께하고 많이 표현 못 했지만 항상 고마웠던 2013학번 재문이, 주영이, 재훈이, 정섭이. 너무 감사하였던 민규형, 충현이, 승희, 희경이, 송희, 세나, 선혜, 소진이, 경환이형, 종민이, 진욱이, 현택이형, 그리고 은우형. 이 모든 고분자재료 연구실 선배님들과 후배님들에게 감사하다는 말씀을 전하고 싶습니다.

그리고 저의 소중한 지인들과 친구들에게 감사함을

전달합니다. 우선, 이제는 정말 가족과 같은 멘붕 멤버들, 대장이자 맏형이신 “만리장성” 연준형님, 나보다 운동을 더 많이 하는 “육손” 제갈이, 2005년부터 함께하고 계속 함께할 “Fungus” 봉균이, 같은 과에서 같은 대학원으로 온 “badger” 제원이, 여전히 눈빛이 촉촉한 “젖날” 영빈이, 아직도 미스터리한 “으악새” 형철이, 모든 것을 다 가진 “The man” 경진이, 그리고 명예회원이된 “타바코” 동하, 명예회원2 성원이, 명예회원3 광현이에게 감사합니다. 그리고 중학교 때부터 함께 해왔던 나의 정말 소중하고 감사한 친구 봉주와 우익이, 부산사나이 한호에게 감사인사를 드립니다. 또, 2010년부터 지금까지도 함께 하고 있는 농구 모임 “후퍼스”의 100명 가까이 되는 모든 멤버들에게 감사하고 일일이 언급하지 못한 점 죄송합니다. Penn State에서 추억을 공유하였고 지금도 소중한 주영이형, 헌재형, 원석이, 대효, 선규, 가교, 성원이와 “유일한후배”인 좋은 날이 계속 올 현경이에게도 감사함을 전달합니다. 또, 너무 좋은 “타이밍”에 짠하고 나타나준 서우에게 나타나줘서 너무 감사하다는 말과 “앞으로 더욱 잘하겠다는 말”, 그리고 그 타이밍이 “평생을 좌우할 좋은 타이밍”이였다는 말을 하고 싶습니다.

다음으로 친척, 친지분들께 감사함을 전합니다. 하늘에 계신 할아버지, 할머니, 넷째 고모, 그리고 지금도 너무 보고싶고 감사하고 농구를 처음 알려주셨던 성엽이형에게 감사합니다. 어렸을 때부터 저를 너무 많이 보살펴주시고 항상 죄송한 마음이 너무 큰 외할아버지와 외할머니 에게도 너무 감사하다는 말씀을 드리고 싶습니다. 첫째 고모와 고모부, 둘째 고모와 고모부, 셋째 고모와 고모부, 넷째 고모부, 다섯째 고모와 고모부, 막내 고모와 고모부, 큰삼촌과 큰숙모, 작은삼촌과 작은숙모, 그리고 이모와 이모부께 너무 감사합니다. 그리고 나의 사촌인 현서누나, 두선이누나, 선이누나, 성희누나, 수연이누나, 종현이, 병현이, 수정이, 명준이형, 동현이, 나경이, 홍범이, 재경이, 성하에게도 너무 감사합니다. 제가 받았던 도움과 사랑을 갚아 나갈수 있도록 하겠습니다.

마지막으로 아버지와 어머니 그리고 예서에게 너무 감사하다는 말을 전하고 싶습니다. 아버지와 어머니께 어떻게 감사를 드려야할지 모르겠습니다. 부족한 아들을 항상 응원해주시고, 무조건적인 사랑을 주셨고, 제 몸 돌보지 않고 저를 위해서만 살아주신 아버지와 어머니 너무 감사하고 죄송합니다. 아버지와 어머니 사랑 덕분에 유학과 박사학위

과정을 무사히 마칠 수 있었습니다. 오래사시며 제가 더 나은 사람이 되는 모습을 계속 지켜봐주세요. 이제부터는 제가 부모님께 보답해가겠습니다. 그리고 마음으로는 너무 친하지만 많은 시간을 떨어져서 지내서 아직 쑥쓰러운 동생에서에게도 너무 감사하다는 말을 전하고 싶습니다. 앞으로는 더욱 좋은 오빠가 되도록 하겠습니다.

이렇게 고마운 분들 덕분에 무사히 학위를 마치고 관악산을 내려갑니다. 다시 한번 너무 감사드립니다. 앞으로 어느 곳에 있던, 어떤 일을 하던 항상 최선을 다하고 처음 관악산을 올라오던 때의 마음 가짐으로 살아가겠습니다.

2018. 5. 8

관악을 내려가며

윤창민 드림